Technische Universität München
TUM School of Engineering and Design

High-Frequency Flame-Acoustic Interaction Mechanisms in Reheat Flames

Jonathan James McClure

Vollständiger Abdruck der von der TUM School of Engineering and Design der Technischen Universität München zur Erlangung eines

Doktors der Ingenieurwissenschaften (Dr.-Ing.)

genehmigten Dissertation.

Vorsitz:
Prof. Dr.-Ing. Nikolaus A. Adams
Prüfende der Dissertation:
Prof. Dr.-Ing. Thomas Sattelmayer
Prof. Dr. Alessandro Orchini

Die Dissertation wurde am 27.09.2023 bei der Technischen Universität München eingereicht und durch die TUM School of Engineering and Design am 29.01.2024 angenommen.

Acknowledgements

The research summarised in this thesis was carried out at the Chair for Thermodynamics of the Technical University of Munich. The project was funded by the Deutsche Forschungsgemeinschaft (DFG, German Research Foundation, Project no. 414909282), whose support is gratefully acknowledged.

I would first like to thank Prof. Dr.-Ing. Thomas Sattelmayer and Dr.-Ing Mirko Bothien for their scientific supervision throughout the project. Their invaluable comments and insights over the last few years greatly helped progress my research. In particular I appreciate the freedom given to me to set my own goals throughout the project and pursue the most promising avenues of research. Next, I would like to recognise the scientific support of Dr.-Ing. Christoph Hirsch, whose guidance helped keep me on track both with my research and also with the writing of this thesis. I would also like to thank Prof. Dr. Alessandro Orchini for being my second examiner and Prof. Dr.-Ing. Nikolaus Adams for taking the role of chair during my defence.

I would next like to thank my colleagues from the Chair of Thermodynamics for numerous scientific discussions and also for the excellent atmosphere at the institute. Most significantly I would like to thank my office and lab partner Florian Franke for the valuable discussions as well as the long hours spent keeping the lab running over the last few years. I would also like to mention Moritz Merk and Simon Tartsch for numerous nice exchanges throughout my time at the institute. Thanks also to the SI group, especially Gerrit Heilmann, Thomas Hofmeister and Pedro Romero for helping me acclimatise at the beginning of my project and for introducing me to the field of thermoacoustics.

For their continuous help with the manufacturing and maintenance of parts for my test rig, I would like to extend my thanks to the workshop staff. In particular, Jens Hümmer, Thomas Schleussner and Gerhard Giel deserve a mention for their support with several occasions of last-minute repairs in the middle of essential test campaigns. I also wish

to extend my thanks to the secretarial staff Helga Bassett and Sigrid Schulz-Reichwald for their helping me navigate the worlds of TUM administration and German paperwork.

Finally, I would like to thank my family and friends for their continuous support over the years. Most importantly I would like to thank my parents for their constant support over the years, without which this thesis would not have been possible.

Munich, September 2023 Jonathan McClure

Abstract

Gas turbines featuring sequentially staged combustion systems offer excellent performance in terms of fuel flexibility, part load performance and combined-cycle efficiency. These reheat combustion systems are therefore a key technology for meeting fluctuating power demand in energy infrastructures with increasing proportions of volatile renewable energy sources. To allow the high operational flexibility required to operate in this role, it is essential that the impact of thermoacoustic instabilities is minimised at all engine load conditions. In this case, high-frequency thermoacoustic instabilities in the second "reheat" combustion stage are investigated. Reheat flames are stabilised by both autoignition and propagation and, as a result, additional thermoacoustic driving mechanisms are present compared with more conventional swirl-stabilised combustors.

The presence of both autoignition and propagation stabilisation in the reheat combustor presents a unique challenge for the prediction of thermoacoustic instabilities, as distinct driving mechanisms related to each combustion regime can be present simultaneously. This is particularly true for high-frequency instabilities due to the acoustically non-compact nature of the flame, meaning that different acoustic mode shapes may permit different flame-acoustic interactions depending on the overlap of pressure nodes and antinodes with autoignition- and propagation-stabilised flame zones. Prior investigations of both swirl and reheat flames have revealed a number of potential driving mechanisms; modulation of the heat release in the reactive shear layers, modulation of the pressure- and temperature-sensitive autoignition flame zone as well as periodic displacement and deformation of the flame by the acoustic velocity field. As these mechanisms can exist simultaneously in reheat flames, it is expected that the overall driving is a superposition of the contributions from each mechanism. The main goal of this work is therefore to determine the relative contributions of each mechanism and to identify which are likely to dominate flame-acoustic interactions in reheat combustion systems.

Experimental investigations are carried out using a lab-scale reheat test rig at atmospheric pressure. The test rig exhibits thermoacoustically unstable behaviour in the high-frequency regime at two modal frequencies. Preliminary investigation of these modes suggests that they are each associated with different flame-acoustic interaction mechanisms. The dynamic flame response of each mode is investigated to determine the underlying physical mechanisms which drive the thermoacoustic oscillations. It is found that driving for each mode originates from one of the distinct flame regimes of the reheat combustor. The weaker mode is associated with interactions between the propagation-stabilised shear layers and the acoustic velocity field via vortex shedding. High-amplitude limit-cycle oscillations are observed for the other mode and these are instead due to modulation of the autoignition flame by the acoustic pulsations. This is observed from optical flame measurements as a local axial flame motion caused by the coherent oscillations of the autoignition delay time, which is highly sensitive to pressure and temperature disturbances. This is further investigated through the development of a reduced order model for the autoignition delay modulation which is compared with the experimental results. The insights gained from this investigation provide confirmation of the relevant driving mechanisms of high-frequency thermoacoustic instabilities in reheat flames and contributes to the ongoing development of models to allow prediction and mitigation of thermoacoustic instabilities in reheat combustion systems, which are crucial for reliable combustor designs in the future.

Kurzfassung

Gasenturbinen mit sequenziell gestuften Verbrennungssystemen bieten hervorragende Leistung in Bezug auf Brennstoffflexibilität, Teillastleistung und Wirkungsgrad im Kombi-Kreisprozess. Diese Wiederverbrennungssysteme sind daher eine Schlüsseltechnologie, um den schwankenden Strombedarf in Energieinfrastrukturen mit zunehmenden Anteilen volatiler erneuerbarer Energiequellen zu decken. Um die hohe betriebliche Flexibilität zu ermöglichen, die für diese Aufgabe erforderlich ist, ist es wesentlich, dass der Einfluss von thermoakustischen Instabilitäten unter allen Lastbedingungen des Motors minimiert wird. In diesem Fall werden Hochfrequenz-Thermoakustikinstabilitäten in der zweiten "Wiederverbrennungs"-Verbrennungsstufe untersucht. Die Wiederverbrennungsflammen werden sowohl durch Autozündung als auch durch Propagation stabilisiert, wodurch im Vergleich zu konventionelleren, durch Wirbel stabilisierten Brennkammern zusätzliche thermoakustische Antriebsmechanismen vorhanden sind.

Die gleichzeitige Existenz von Autozündungs- und Propagationsstabilisierung in der Wiederverbrennungsbrennkammer stellt eine einzigartige Herausforderung für die Vorhersage thermoakustischer Instabilitäten dar, da unterschiedliche Antriebsmechanismen im Zusammenhang mit jedem Verbrennungsregime gleichzeitig auftreten können. Dies gilt insbesondere für Hochfrequenzinstabilitäten aufgrund der akustisch nicht kompakten Natur der Flamme, was bedeutet, dass unterschiedliche akustische Modenformen unterschiedliche Wechselwirkungen zwischen Flamme und Akustik ermöglichen können, abhängig von der Überlappung von Druckknoten und -antiknoten mit Autozündungs- und Propagationsstabilisierten Flammzonen. Vorherige Untersuchungen von Wirbel- und Wiederverbrennungsflammen haben eine Reihe potenzieller Antriebsmechanismen aufgezeigt: Modulation der Wärmeabgabe in den reaktiven Scherenschichten, Modulation der druck- und temperatursensitiven Autozündungsflammzone sowie periodische Verschiebung und Verformung der Flamme durch das akustische Geschwindigkeitsfeld. Da diese Mechanismen in Wiederverbren-

nungsflammen gleichzeitig existieren können, wird erwartet, dass der Gesamtantrieb eine Überlagerung der Beiträge jedes Mechanismus ist. Das Hauptziel dieser Arbeit ist daher die Bestimmung der relativen Beiträge jedes Mechanismus und die Identifizierung derjenigen, die wahrscheinlich die Wechselwirkungen zwischen Flamme und Akustik in Wiederverbrennungssystemen dominieren.

Experimentelle Untersuchungen werden an einer Laborskalen-Wiederverbrennungsprüfanlage unter atmosphärischem Druck durchgeführt. Die Prüfanlage zeigt thermoakustisch instabiles Verhalten im Hochfrequenzbereich bei zwei modalen Frequenzen. Voruntersuchungen dieser Moden deuten darauf hin, dass sie jeweils mit verschiedenen Mechanismen der Wechselwirkung zwischen Flamme und Akustik verbunden sind. Die dynamische Flammenantwort jeder Mode wird untersucht, um die zugrunde liegenden physikalischen Mechanismen, die die thermoakustischen Schwingungen antreiben, zu bestimmen. Es wird festgestellt, dass der Antrieb für jede Mode von einem der unterschiedlichen Flammenregime der Wiederverbrennungsbrennkammer stammt. Die schwächere Mode ist mit Wechselwirkungen zwischen den propagationsstabilisierten Schichten und dem akustischen Geschwindigkeitsfeld durch Wirbelabwurf verbunden. Für die andere Mode werden hochamplitudige Limitzyklusschwingungen beobachtet, die stattdessen auf Modulation der Autozündungsflamme durch die akustischen Pulsationen zurückzuführen sind. Dies wird aus optischen Flammenmessungen als lokale axiale Flammenbewegung durch die kohärenten Oszillationen der Autozündungsverzögerungszeit beobachtet, die sehr empfindlich auf Druck- und Temperaturstörungen reagiert. Dies wird weiter durch die Entwicklung eines reduzierten Modells für die Modulation der Autozündungsverzögerung untersucht, das mit den experimentellen Ergebnissen verglichen wird. Die Erkenntnisse aus dieser Untersuchung bestätigen die relevanten Antriebsmechanismen von Hochfrequenz-Thermoakustikinstabilitäten in Wiederverbrennungsflammen und tragen zur laufenden Entwicklung von Modellen bei, um die Vorhersage und Minderung von Thermoakustikinstabilitäten in Wiederverbrennungssystemen zu ermöglichen, die für

zuverlässige Brennkammerentwürfe in der Zukunft entscheidend sind.

Contents

List of Figures **xiii**

Nomenclature **xix**

1 Introduction **1**
1.1 Background and Motivation 1
1.2 Reheat Combustion Systems 4
1.2.1 Operational Flexibility 5
1.2.2 Fuel Flexibility 7
1.2.3 Emissions Reduction 7
1.3 High-Frequency Thermoacoustic Instabilities 8
1.3.1 Flame-Acoustic Feedback 10
1.3.2 Thermoacoustic Stability and the Rayleigh Criterion 11
1.3.3 Thermoacoustic Instability Evolution and Limit-Cycle Oscillations 12
1.3.4 Frequency Regimes of Thermoacoustic Instabilities 13
1.3.5 Thermoacoustic Instabilities in Reheat Flames . . . 14
1.4 Research Objectives and Thesis Outline 14

2 Flame-Acoustic Coupling in Reheat Combustors **17**
2.1 Driving due to Flame Displacement and Deformation . . . 18
2.2 Driving due to Acoustically-Induced Vortex Shedding . . 19
2.3 Driving due to Modulation of the Autoignition Flame by Acoustic Perturbations 21
2.3.1 Autoignition Flame Response Studies in the Low-Frequency Regime 21

2.3.2 Autoignition Flame-Acoustic Coupling in the High-Frequency Regime 23

3 Experimental Setup 26
3.1 Reheat Test Rig 26
3.1.1 Vitiator Stage 27
3.1.2 Reheat Stage 29
3.2 Diagnostics 30
3.2.1 Acoustic Measurements 30
3.2.2 Bandpass-Filtered Flame Chemiluminescence . . . 32
3.3 Reheat Flame Characteristics 33

4 Data Processing Techniques 36
4.1 Identification of Acoustic Pressure Oscillations 36
4.2 Identification of Coherent Heat Release Oscillations 38
4.3 Acoustic Field Estimation 40

5 Reheat Combustor Thermoacoustic Response 44
5.1 Impact of Operating Conditions on Transverse Thermoacoustic Response 44
5.2 Transverse Modes Acoustic Characteristics 48
5.2.1 T1y Mode Response 48
5.2.2 T1z Mode Response 50
5.3 Mode Shape Dependent Flame-Acoustic Interactions . . . 53
5.4 Summary 58

6 Reactive Shear Layer Modulation due to Acoustically-Induced Vortex Shedding 60
6.1 T1y Mode Dynamic Flame Response 60
6.2 Intermittent Flame Response 66
6.2.1 Phase Space Trajectory Reconstruction from Acoustic Time Series Data 66
6.2.2 Construction of Condition-Locked Ensemble-Averaged CL Images 71

6.2.3 Flame Dynamics Associated with Intermittency Conditions 72
6.3 Summary 78

7 Autoignition Delay Modulation by High-Frequency Acoustic Pulsations 81
7.1 Flame Dynamics Associated with High-Amplitude Limit-Cycle Oscillations 81
7.2 Modelling of Autoignition Delay Modulation 89
7.2.1 High-Frequency Autoignition Delay Modulation Mechanism 89
7.2.2 Flame Response Model Setup 91
7.2.3 Identification of Ignition Location 95
7.2.4 Autoignition Flame Response to Transverse Acoustic Oscillations 96
7.3 Summary 101

8 Summary and Conclusions 104

9 Previous Publications 110

List of Figures

1.1 Comparison of the GE/Ansaldo Energia GT24/26 and Ansaldo Energia GT36 combustor architectures. Adapted from Gant [66]. 5

1.2 Reheat gas turbine operation concept. Adapted from Guyot et al. [44]. 6

2.1 Illustration of the velocity induced by the acoustically-induced vortices along the shear layer. Adapted from Hofmeister [59]. 20

3.1 Sketch of the reheat test rig indicating the two combustion stages as well as key flow inlets and components. Adapted from Berger [110]. 27

3.2 Sectional view of the vitiator indicating the positions of the six swirl burners and dilution air tubes. Adapted from Berger [110]. 28

3.3 Illustration of the diagnostic setup for synchronous measurement of acoustic and heat release data. 31

3.4 Illustration of the reheat combustor setup with the camera positions and instrumentation ports indicated. 32

3.5 LOS-integrated, time-averaged CL images of the reheat flame from side-, top- and rear-view perspectives. Regions stabilised mainly by auto-ignition and propagation are indicated. 34

4.1 Procedure for correlating image and pressure data. The upper plot shows the pressure (blue) and phase (red) signals while the lower plot shows the intensifier gating signal II. Circles indicate the beginning of image exposures. 39
4.2 Approach for estimating reheat combustor temperature field from mean CL images. 41
4.3 Comparison of the numerically estimated pressure (solid lines) along the combustor with the pressures measured by the axially distributed pulsation probes (circles) for the two first transverse modes in the reheat combustor at 1600 Hz and 3000 Hz. For ease of comparison, values are normalised by the maximum pressure amplitudes. 42

5.1 Amplitude spectra from two test conditions with varying fuel reactivity. Dashed lines indicate bandpass filter limits for each peak. 45
5.2 RMS of the bandpass-filtered pressure signal at the T1z mode frequency over thermal power level for different fuel blends. 47
5.3 Upper: Sample of the pressure time series bandpass-filtered about the T1y mode frequency with envelope amplitude indicated by the black line. Lower: Spectrogram illustrating the bursts of high-amplitude periodic behaviour at the T1y mode frequency. 49
5.4 Acoustic pressure field estimation of the 1600 Hz T1y mode calculated via FEM. 50
5.5 Sample of the pressure time series bandpass-filtered about the T1z mode frequency with envelope amplitude indicated by the black line. 51
5.6 Acoustic pressure field estimation of the 3000 Hz T1z mode calculated via FEM. 52
5.7 Transverse component of the 1600 Hz T1y mode acoustic pressure (upper) and velocity (lower) fields with the flame boundary illustrated by the black contour. 54

5.8 Transverse component of the 3000 Hz T1z mode acoustic pressure (upper) and velocity (lower) fields with the flame boundary illustrated by the black contour. 55

5.9 Illustration of the difference in relative integration widths associated with the shear layers and the autoignition zone for LOS integrated CL from the top-view perspective. . . . 56

6.1 Phase-locked ensemble-averaged CL images of the flame at the T1y mode frequency for sample phase intervals (left) and the corresponding difference images (right). . . 62

6.2 CL oscillations in the upper shear layer region for phase intervals corresponding to maximum (upper) and minimum (lower) acoustic pressure. Insets indicate the acoustic pressure distribution in the combustion chamber (calculated via FEM) during each phase interval. 64

6.3 Normalised, spatially-integrated CL oscillation intensity over the T1y mode cycle in the upper shear layer region (blue circles) and the entire upper combustor half (red squares). The dashed lines are fitted in a least squares sense to the data points and the dotted line indicates the acoustic pressure. 65

6.4 Bandpass-filtered pressure signal with sample regions corresponding to each of the four defined intermittency conditions. Typical pulsation amplitude ranges for the stochastic and periodic conditions are indicated. 67

6.5 Selection of the phase space reconstruction parameters of time delay (left) and embedding dimension (right). 68

6.6 Reconstructed phase space trajectories for each intermittency condition. Arrows for growth and decay conditions indicate the trend of the trajectory over time. Inset amplitude spectra illustrate the relative strength of the T1y mode for each condition. 70

6.7 Example of the intermittency condition identification for the condition locking procedure. The dashed line indicates the smoothed envelope amplitude while the solid line represents its gradient. Markers show the indentified centres for different condition regions. 72

6.8 Condition-locked, ensemble-averaged CL images during each intermittency condition. Left: mean images for each condition. Right: difference in CL intensity between the top images and the overall mean image. The black contour represents the approximate flame boundary of the overall mean image for reference. 74

6.9 Phase- and condition-resolved ensemble-averaged difference images for a sample phase interval corresponding to each intermittency condition. 77

7.1 Phase-locked ensemble-averaged CL images of the flame from the rear view at the T1z mode frequency for sample phase intervals (left) and the corresponding difference images (right). In the left column, dotted vertical line indicates overall mean flame tip position and dashed contours are approximate flame tip boundaries. 83

7.2 Flame contours highlighting axial tip movement with overlaid acoustic pressure field. Solid contour is the displaced flame at phase interval $\phi = 0$ while the dashed contour is the mean flame shape. 84

7.3 Phase-locked ensemble-averaged CL images of the flame from the rear-view for sample phase intervals. The solid vertical line indicates the median location of heat release for the overall mean image while the dotted lines indicate the median heat release location for the corresponding ensemble-averaged image. Detail views A and B show the direction of the flame displacement during the first and third phase intervals. 85

7.4 Phase-locked ensemble-averaged CL difference images of the flame from the rear-view corresponding to the phase intervals shown in Fig. 7.3. 87
7.5 Flame-acoustic interaction mechanism for high-frequency autoignition delay modulation. 89
7.6 Schematic of the reduced order model showing the approaches used to represent each main component of the test rig. 92
7.7 Sketch of the plug flow reactor setup used to model the autoignition flame response in the second stage. 93
7.8 Axial temperature profile of the outermost mixture plug calculated by the PFR model with the imposed acoustic oscillations for a sample injection time, t_i. The area jump and ignition positions are indicated by x_j and x_{ig}, respectively. Both the instantaneous temperature in the mixture plug, T_{plug}, and the temperature due to the chemical reactions, T_r, are shown. 96
7.9 Comparison of ignition length variation over a full oscillation cycle between the flame response model and experimental measurements. The dashed line is fitted in a least squares sense to the experimental data points. The experimental error bars show the uncertainty of measuring ignition location due to limited pixel resolution. The shaded region around the model results shows the difference in ignition length variation calculated from the upper and lower bounds of experimental input uncertainties. 97
7.10 Pressure and temperature sensitivity of the autoignition delay time calculated by the flame response model with no acoustic perturbations. 99
7.11 Comparison of the ignition length variation and the net pressure oscillation experienced by a fluid particle over an oscillation cycle. 100

Nomenclature

Latin Letters

A	Area [m^2]
A	Envelope amplitude [J/kg-K]
c	Speed of sound [m/s]
dim	Embedding dimension [-]
f	Frequency [Hz]
f_s	Sampling rate [Hz]
H	Chamber height [m]
I	Chemiluminescence intensity [-]
l	Length [m]
L	Chamber length [m]
$\dot{m}$	Mass flow rate [kg/s]
N	Total number of samples [-]
p	Pressure [Pa]
P	Analytic pressure signal [Pa]
$\dot{Q}$	Heat release rate [W]
t	time [Pa]
T	Temperature [K]
P	Analytic pressure signal [Pa]
u	Flow velocity [m/s]
V	Volume [m^3]
W	Chamber width [m]
$\mathbf{x}$	Spatial coordinate vector [m]
$x_{C_3H_8}$	Propane mass ratio [-]

x,y,z	Cartesian coordinates [m]
Y_{PS}	Phase space trajectory [-]

Greek Letters

γ	Ratio of specific heats [-]
λ	Air-fuel equivalence ratio [-]
ρ	Density [kg/m^3]
τ	Time delay [s]
ϕ	Phase angle [rad]
ω	Angular frequency [rad/s]

Operators

$(\dot{\bar{.}})$	Mean value
$(\ldots)'$	Deterministic/oscillatory component
$(\dot{\tilde{.}})$	Stochastic component
$(\dot{\hat{.}})$	Hilbert transformed component

Subscripts

cc	Combustion chamber
$cond$	Intermittency condition
fl	Flame
i	Fluid particle injection index
ig	Ignition
in	Inlet
inj	Injector
j	Area jump location

k	Image index
max	Maximum
min	Minimum
MS	Mixing section
$plug$	Mixture plug
pre	Preheated air
PS	Phase space
r	Reactions
RC	Reheat combutsor
s	Sample
vit	Vitiator

Abbreviations

CL	Chemiluminescence
FEM	Finite element method
FFT	Fast Fourier transform
GT	Gas turbine
HF	High frequency
II	Image intensifier
LF	Low frequency
LOS	Line of sight
RI	Rayleigh integral
RMS	Root mean square
$T1y$	First transverse mode in y-direction
$T1z$	First transverse mode in z-direction

1 Introduction

1.1 Background and Motivation

Access to a consistently available supply of electricity has become an essential part of modern life. The demand for electricity continues to surge as populations grow, economies develop and industries expand. As a result, it is expected that global energy demand will increase by 30% by the year 2030 [1]. Historically, the increased energy demand was met through the use of fossil fuels; however, this has had a major ecological impact at both local [2] and global scales [3]. To counter the rise of global temperatures and meet the goal of keeping the global temperature rise within 1.5 °C, a transition to a decarbonised energy economy is required by 2050 [4]. Large scale deployment of renewable sources of power generation is essential to meet this goal in the long term while reducing the energy share of coal and oil fired power plants. In the short term, a shift from these latter power generation methods to natural gas fired power plants is also contributing to decarbonisation due to greatly reduced emissions [5, 6].

One of the key challenges of the future energy infrastructure is consistently meeting fluctuating power demand with an increasing proportion of energy generated by volatile renewable sources [7, 8]. To compensate for this volatility, it is essential that reliable methods of power generation are available which can rapidly compensate for supply shortages and changing demand without compromising climate change targets [9]. Gas turbines, with their inherent ability to quickly adjust output and respond to varying loads over a wide operational range, offer an ideal solution for balancing non-programmable renewable sources such as solar and wind power [10–13]. To maintain this role as decarbonisation pro-

gresses, fuel flexibility will also become an increasing important consideration for power generation gas turbines. As fuel sources for gas fired power plants become more diverse due to increased amounts of shale and synthetic gas, it is essential that the variation in fuel reactivity can be accounted for [14–20]. Furthermore, hydrogen is expected to become a significant additive to the fuel mixture to aid in the reduction of greenhouse gases [21–26], with the potential to eventually run with 100% hydrogen fuel [27–29]. The use of hydrogen not only aids in reducing greenhouse gases, but also offers a potential method for long term energy storage by using hydrogen produced by excess power generation from renewable sources [30]. However, hydrogen presents a number of technical challenges, in particular due to its extremely high reactivity which requires significant changes to conventional gas turbine combustion systems [31–34]. In addition to these core requirements of operational and fuel flexibility, it is also essential that advancements in emissions reduction, efficiency and reliability continue in order to meet increasingly strict regulations and to remain an economically viable method of power generation.

Lean-premixed combustion systems are used in the majority of modern power generation gas turbines which offer significant advantages compared with diffusion based combustion systems [35]. In these lean-premixed systems, the fuel and air are mixed upstream of the combustion chamber, which results in a homogeneous mixture prior to ignition. This produces a more uniform, low-temperature flame and avoids the occurrence of hotspots due to uneven mixing, reducing the formation of nitrogen oxides (NO_x) [36]. The high efficiency of these combustion systems over a wide operational range also reduces other key pollutant emissions such as carbon monoxide (CO), carbon dioxide (CO_2) and unburned hydrocarbons (UHC) [37]. In order to meet climate goals and meet future emissions regulations, further innovation on the lean-premixed combustion concept is required. A number of different concepts have been proposed which transition from the large swirl burners which have dominated gas turbine combustion systems since their inception [14, 38–42]. One of the most promising concepts, which is al-

ready in large scale deployment, is the reheat (or sequentially-staged) combustion system which utilises two axially-staged combustors with partial autoignition flame stabilisation in the second stage [43–45]. Key advantages of the reheat concept are excellent performance in terms of turn-down ratio, part-load efficiency and fuel flexibility, making it ideal for maintaining grid stability as renewable power generation increases [46,47].

As is often the case in advanced lean-premixed combustion systems, the improvement in emissions and performance characteristics is accompanied by increased susceptibility to thermoacoustic instabilities [48]. These manifest as high-amplitude pressure pulsations which arise due to a positive feedback loop between the acoustic field in the combustor and the unsteady heat release of the flame [49,50]. The consequences of this coupling between flame and acoustics include compromised combustion efficiency and increased pollutant emissions, limitations on the operational window of the gas turbine, as well as increased mechanical loads on the combustor and other components, potentially resulting in reduced component lifespan and in the worst case leading to catastrophic failure [48,51]. Prediction of such instabilities is challenging and historically a reactionary approach has been used to mitigate instabilities which arise late in design or even in production [52]. In recent years there has been considerable effort made in the development of predictive tools to mitigate or remove the potential for thermoacoustic instabilities from the earliest design stages [53–59]. These predictive approaches, and subsequent development of mitigation strategies, require a detailed understanding of the underlying mechanisms through which the flame and acoustic field interact [60,61]. This thesis focusses on enhancing this knowledge for reheat combustion systems, with a particular emphasis on the interactions between the acoustics and the partially autoignition stabilised flame in the second combustion stage.

1.2 Reheat Combustion Systems

Reheat combustion systems represent a key technology for meeting future power demand in a global energy infrastructure increasingly dominated by renewable sources of power generation. The feasibility of reheat combustors has already been demonstrated and is currently deployed for large scale power generation in the GE GT24, GE/Ansaldo Energia GT26 [46] and the Ansaldo Energia GT36 [45] gas turbines. The concept was originally developed by ABB in the 1990s with the GT24/26 gas turbines and was later acquired by Alstom where development of the GT36 was started. Currently, the GT24 is owned by GE, the GT26 is jointly owned by GE and Ansaldo Energia while the GT36 is owned by Ansaldo Energia.

These gas turbines feature two separate, sequential combustion stages. The first stage is broadly similar to a typical single-staged combustor and utilises an aerodynamically-stabilised premixed flame. The high temperature of the combustion products is taken advantage of in the second reheat stage, where fuel is added to the hot gas flow which results in a secondary flame partially stabilised by autoignition (the reheat flame also has a contribution from aerodynamic stabilisation which varies depending on the operating conditions [62]). This autoignition flame stabilisation behaves distinctly from the aerodynamic stabilisation in the first stage. Due to the high temperatures which the secondary fuel is injected into, radicals are produced once the air and fuel mix without an external spark or addition of heat [63]. After some time (in the order of milliseconds) the mixture ignites spontaneously. This delay before ignition is referred to as the autoignition delay time and it is sensitive to fuel reactivity as well as temperature of the flow [64,65]. As a result, the flame position is mainly independent of its own adiabatic flame temperature and can be adjusted by varying the upstream conditions in the first combustion stage.

This sequentially-arranged combustor setup is illustrated in Fig. 1.1 for both the GT24/26 and GT36 architectures. In the GT24/26 architecture,

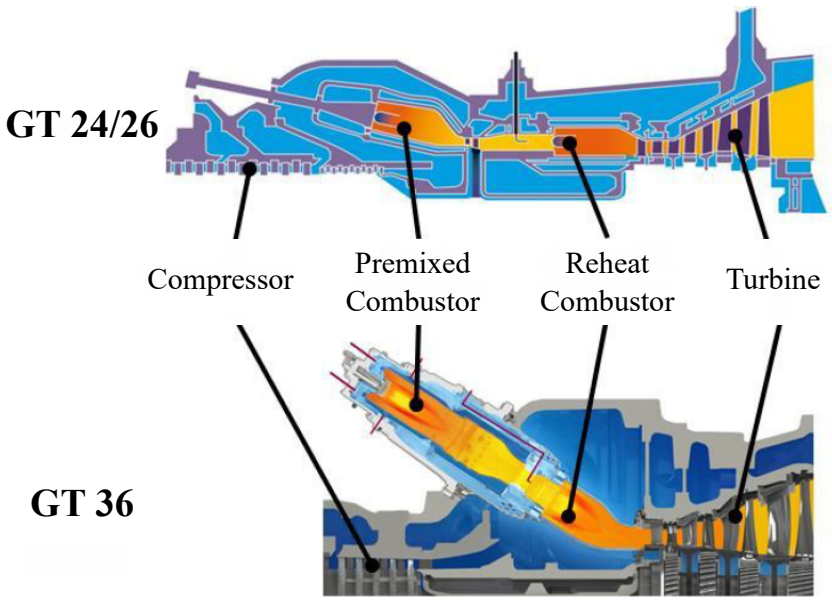

Figure 1.1: Comparison of the GE/Ansaldo Energia GT24/26 and Ansaldo Energia GT36 combustor architectures. Adapted from Gant [66].

the two combustion stages are separated by the high pressure turbine and therefore a significant pressure drop exists between the two stages. In the case of the GT36, the high-pressure turbine is positioned after the secondary combustor and the combustion products from the first stage are instead mixed with bypass air from the compressor such that both stages operate at roughly the same pressure. Splitting the combustion process into two discrete stages provides several advantages over the standard single-stage design. These benefits can be broadly categorised into three categories: operational flexibility, fuel flexibility and emissions reduction.

1.2.1 Operational Flexibility

Figure 1.2 illustrates the operation concept of a reheat gas turbine. It can be seen that across most of the operational range of the engine the

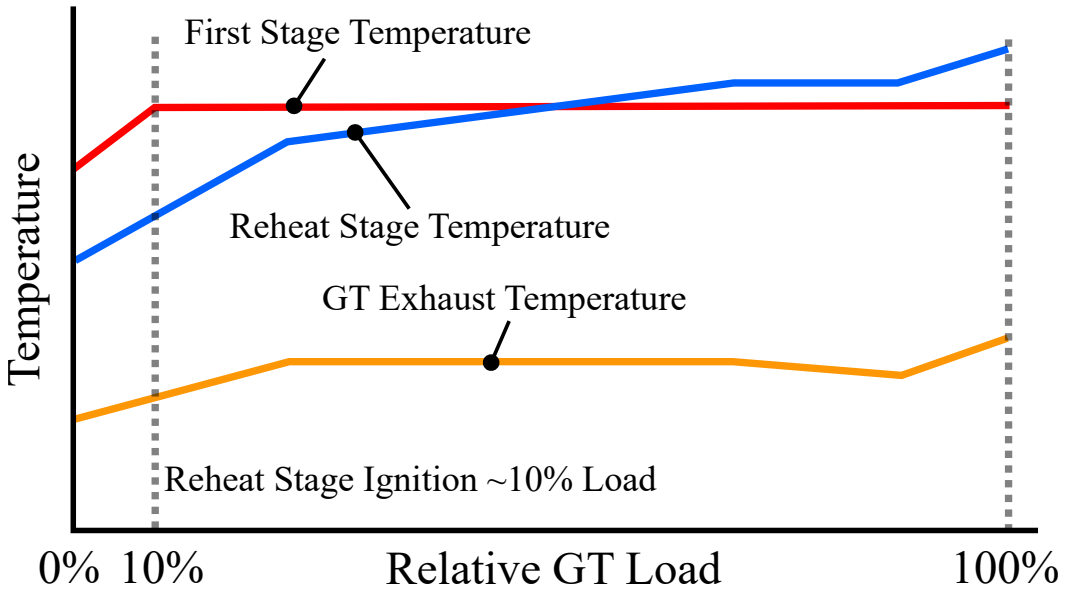

Figure 1.2: Reheat gas turbine operation concept. Adapted from Guyot et al. [44].

first stage combustor remain approximately constant at its deign conditions, while adjustments to the load are made by varying the fuel input to the reheat combustor. This unique approach to load control has useful consequences when considering operational flexibility. It negates one of the key limitations of conventional single-stage combustors which is difficulty operating away from design conditions, particularly at low loading [35]. This is becoming more of an issue as load flexibility is becoming increasingly important for power generation gas turbines [13]. In the case of the reheat concept, keeping the first stage at its design condition avoids the risk of efficiency and emissions compromises. As the autoignition stabilised flame in the reheat combustor is mostly independent of its own adiabatic flame temperature, this does not present issues for static flame stability [66]. This gives the reheat concept its excellent part load performance. Furthermore, by switching off the fuel supply to the reheat combustor, it is possible to maintain idle conditions at very low loading with only the first stage ignited. As the first stage is still operating at design conditions, the risk of lean blow-off is avoided and

the flame can remain anchored without sacrificing efficiency and emissions [44]. This allows rapid ramp-up of the power output and avoids the need for repeated startup/shutdown cycles which reduce the lifespan of the engine components [37]. It can also be seen from Fig. 1.2 that the exhaust temperature remains fairly consistent over the load range, which is advantageous in a combined-cycle gas turbine setup as it reduces the thermal stresses on the heat recovery steam generator.

1.2.2 Fuel Flexibility

The sequentially-staged setup also benefits the fuel flexibility of the engine. In a conventional single-stage combustor, burning fuels with increased reactivity, such as hydrogen and higher hydrocarbon fuels, causes the flame to move upstream [67]. This increases NO_X emissions and may lead to flashback which can damage the burner [14, 68, 69]. To counter this, the flame temperature would have to be reduced which lowers efficiency and limits the power output of the engine. In the sequentially-staged configuration, the temperature in the first stage would be similarly reduced, however this would be compensated by increasing the fuel input to the reheat combustor. A decrease in the autoignition delay time due to elevated fuel reactivity would be countered by the reduced flow temperature from the first stage, maintaining a consistent flame position. This would also result in an increase in the reheat flame temperature, which is the key parameter on which engine efficiency and power output depend. The potential for burning highly reactive fuels using reheat combustion extends to the use of hydrogen, which has been an area of increasing interest in recent years.

1.2.3 Emissions Reduction

Emissions levels are also improved with this setup due to the presence of two separate combustion stages and the characteristics of the autoignition stabilised flame. In particular, the main benefit concerns the produc-

tion of CO and NO_x. Minimising formation of these two pollutants is a challenge as each is formed by opposing conditions during the combustion process [70]. A large portion of NO_x emissions are produced due to high flame temperatures and this increases with residence time [71]. On the other hand, CO forms as intermediate step prior to oxidising to form CO_2. Low flame temperatures slow this reaction and long residence times are required to minimise CO in the exhaust. Due to these conflicting requirements, a balance must be achieved to keep both pollutants at levels which meet emissions regulations. The operation concept of the reheat combustor shown in Fig. 1.2 allows a high level of control of these pollutants without limiting engine performance. By reducing the reheat combustor inlet temperature at high load conditions, the flame moves downstream, reducing the residence time in the combustor and minimising NO_x production. The formation of NO_x is also reduced due to the fact that residence times for the autoignition flame are already low due to the high flow velocities at which combustion can occur as well as the homogeneous temperature distribution resulting from the mixing process in the reheat stage [72]. When engine loading is low, increasing the reheat combustor inlet temperature moves the flame upstream and increases residence time, allowing more time for CO to form CO_2.

1.3 High-Frequency Thermoacoustic Instabilities

Prediction and mitigation of thermoacoustic instabilities are two of the key challenges in the design of gas turbine combustions systems. This is becoming increasingly important as many of the modifications needed to reduce emissions production in gas turbines also leads to in increased susceptibility to thermoacoustic oscillations [48]. This is compounded by the increased flexibility requirements for modern gas turbines. In cases where a gas turbine can be expected to operate only at the design point, or within a narrow range of conditions, it is relatively simple to determine the dynamic stability characteristics in this limited band. Specific countermeasures can then be implemented if necessary to dampen any

thermoacoustic oscillations which arise [73–79]. However, as operational flexibility is increased to allow compensation for greater volatility in the power grid, prediction and mitigation of thermoacoustic instabilities becomes more challenging. Due to the sensitivity of these instabilities to changes in operating conditions and fuel type, the empirical approaches used in the past are no longer viable and the focus has instead moved towards the development of numerical tools to predict instabilities [77,80]. However, thermoacoustic modelling with the goal of predicting combustor stability requires a thorough understanding of the underlying mechanisms through which the flame and the acoustic field interact which often necessitates a combination of numerical and experimental studies.

This thesis focusses on the root causes of high-frequency instabilities in the reheat flame of sequentially-staged gas turbine combustion systems. The need for a deeper understanding of this phenomenon was highlighted in recent years with the occurrence of high-frequency screech-type instability in the reheat combustor of GE/Ansaldo Energia GT24/26 gas turbines, which limited the stable operating range of the engine [78,80]. In this case, dampers performed well for the mitigation of low-frequency modes but had to be modified during an engine upgrade to account for these high-frequency modes. This example illustrates the importance of accurate thermoacoustic prediction for both the low-and high-frequency regimes to avoid potential redesigns late in development which can be extremely costly compared with early design stage changes.

This section provides an introduction to thermoacoustic instabilities. First, the basic concept of thermoacoustic feedback between the acoustic field and the flame is introduced. Next, the key criteria by which thermoacoustic stability is assessed is described in terms of Rayleigh's criterion. Then, the evolution of a thermoacoustic instability from onset to saturation is described. The key phenomenological differences between thermoacoustics in the low- and high-frequency regimes is presented next and finally the considerations which are specific to reheat flames are discussed.

1.3.1 Flame-Acoustic Feedback

As described in Section 1.1, thermoacoustic instabilities arise when a positive feedback loop forms between the flame and the acoustic field in the combustor [50]. This coupling is described in the following example. The flame can be considered a volume source of acoustic energy due to the unsteady nature of the heat release. When the flame is disturbed by an acoustic perturbation, the heat release will fluctuate and this will in-turn emit an acoustic disturbance. The resulting acoustic waves travel through the combustor and are partially reflected by the chamber walls, inlets and outlets. These reflected waves travel back to the flame which generates another heat release disturbance and further acoustic waves are emitted. If the energy gained by the acoustic waves from the flame exceeds the amount dissipated through the combustion chamber, this forms the positive feedback loop which can lead to a thermoacoustic instability. The emitted acoustic waves can also indirectly lead to fluctuations of the flame heat release, for example by interacting with the air and fuel inlets, resulting in equivalence ratio fluctuations which are convected to the flame [81–83]. The resulting interactions between acoustic velocity fluctuations and the mean flow may also trigger vortex shedding [84–86]. These are simply examples of the mechanisms through which the acoustic field can couple with the flame heat release and identification of such interaction mechanisms is a key aspect of research into thermoacoustic instabilities.

The relevant coupling mechanisms can vary greatly depending on a number of parameters such as combustor geometry, flame stabilisation mechanism, thermoacoustic mode shape and frequency. In recent years, an increasing number of studies have focussed on improving the physical understanding of these interactions [87–92]. This then allows improvement to predictive techniques which is also an area of increasing interest [52, 54, 57, 58, 93, 94]. Understanding the nature of the most important flame-acoustic feedback mechanisms for different combustor concepts is therefore a key area of thermoacoustic research.

1.3.2 Thermoacoustic Stability and the Rayleigh Criterion

Understanding the feedback loop between the flame and the acoustics is essential for the prediction of thermoacoustic stability. Depending on the phase relationship between the acoustic pressure fluctuations $p'(\mathbf{x},t)$ and the unsteady heat release rate of the flame $Q'(\mathbf{x},t)$, the interactions can be constructive or destructive in nature. This is referred to as the Rayleigh criterion [95] which can be represented mathematically by the Rayleigh integral:

$$\mathrm{RI} = \int_V \oint p'(\mathbf{x},t)\dot{Q}'(\mathbf{x},t)\,dtdV > 0 \tag{1.1}$$

where, $\mathbf{x}$ is the spatial coordinate, t is time and V is volume. This indicates that the growth of a thermoacoustic instability is only possible if the Rayleigh integral is positive. This depends on whether or not the pressure and heat release oscillations are in-phase with each other, i.e. growth is possible when there is a phase difference smaller than $\pi/2$ between these two quantities. Therefore, in order for an instability to grow, heat release must be at a maximum during peak acoustic pressure and vice versa. If the Rayleigh criterion is met and acoustic energy is added to the system, then this is referred to as thermoacoustic driving.

As stated in Section 1.3.1, the rate of acoustic energy addition due to the amplification effects of the flame must exceed the rate of acoustic energy dissipation from the acoustic damping effects of the chamber and mean flow [50,85,96]. These are referred to as the flame driving rate and acoustic damping rate respectively. Linear thermoacoustic stability prediction is based on evaluation of these two conditions which are used to determine the growth rate for an acoustic eigenmode. If the growth rate is positive, pressure oscillations will increase over time and the mode is thermoacoustically unstable.

1.3.3 Thermoacoustic Instability Evolution and Limit-Cycle Oscillations

If a mode is thermoacoustically unstable, pressure oscillations will increase exponentially over time until a maximum oscillation amplitude, referred to as the limit-cycle, is reached. This process described step-by-step in the following.

1. Initially the acoustic field is dominated by stochastic noise due to turbulence and the unsteady heat release of the flame. The thermoacoustic growth rate at this point is negative and therefore acoustic damping is stronger than flame driving. Inspection of the pressure spectrum will reveal small peaks at the system eigenfrequencies; however, amplitudes are low and this corresponds to a stable condition. Some disturbance then causes a heat release fluctuation which amplifies acoustic waves beyond the acoustic damping. A typical example of this initial disturbance may be a result of a change of operating conditions due to changing load demand or a difference in the fuel composition which can impact thermoacoustic stability [97].

2. Following the initial disturbance, pressure oscillation amplitudes grow exponentially with time. At this point the excess flame driving compared with acoustic damping is greatly strengthening the acoustic perturbations over each cycle. This is referred to as the linear growth phase.

3. Eventually, the growth of the oscillation amplitudes slows and the gap between damping and driving is reduced, leading to saturation of the oscillations. The cause of this saturation are a range of nonlinear processes which vary depending on a number of factors [98–100].

4. Once the growth of oscillation amplitudes stops, flame driving and acoustic balance are equalised. Pressure pulsations continue at a

consistent amplitude, referred to as a limit-cycle [101]. This limit-cycle amplitude experiences small modulations due to turbulent combustion noise [102]. The mechanisms which result in the formation of this limit-cycle are typically attributed to the saturation of the flame driving potential with increasing pulsation amplitude [103, 104]. However, recent studies have instead suggested that, for the high-frequency regime, a non-linear increase of acoustic dissipation may instead be the cause of limit-cycle formation [105, 106].

1.3.4 Frequency Regimes of Thermoacoustic Instabilities

Thermoacoustic instabilities can generally be categorised as either low- or high-frequency. These two regimes are phenomenologically distinct and are separated by three key differences. The first and most significant of these is the assumption of an acoustically-compact flame in the low-frequency regime due to long acoustic wavelengths compared with the flame length [107]. In this case, flame-acoustic interactions are dominated by fluctuations of the spatially integrated flame heat release. In the high-frequency regime this assumption no longer applies as acoustic wavelengths are typically of similar magnitudes to the radial extent of the flame. The flame is now acoustically non-compact and local interactions between the flame and acoustics must be considered [108]. Secondly, thermoacoustic driving in the low-frequency regime is typically associated with the time-delayed flame response to convectively transported fluctuations of equivalence ratio, temperature and velocity [48]. These convective effects exhibit a low-pass filter behaviour and are strongly attenuated as oscillation frequency increases [109]. High-frequency thermoacoustic feedback is instead dominated by local, in-phase flame-acoustic interactions. Finally, low-frequency instabilities usually feature simpler mode shapes which can be considered one-dimensional in most cases. High-frequency instabilities are commonly associated with more complex, multidimensional mode shapes and are therefore influenced by local acoustic fluctuations.

1.3.5 Thermoacoustic Instabilities in Reheat Flames

The presence of both autoignition and propagation stabilisation in the reheat combustor presents a unique challenge for the prediction of thermoacoustic instabilities, as distinct driving mechanisms related to each combustion regime can be present simultaneously. This is particularly true for high-frequency instabilities due to the acoustically non-compact nature of the flame, meaning that different acoustic mode shapes may permit different flame-acoustic interactions depending on the overlap of pressure nodes and antinodes with autoignition- and propagation-stabilised flame zones. Prior investigations of both swirl and reheat flames have revealed a number of potential driving mechanisms: modulation of the heat release in the reactive shear layers [110], modulation of the pressure- and temperature-sensitive autoignition flame zone [111] as well as periodic displacement and deformation of the flame by the acoustic velocity field [90, 91]. While it is likely that the overall driving is a superposition of these mechanisms, previous numerical investigations have indicated that the modulation of the autoignition delay time is likely the dominant flame-acoustic coupling mechanism [60,112]. This hypothesis is also supported by a number of studies concerning reheat flame thermoacoustics in the low-frequency regime where the autoignition delay time was significantly influenced by the acoustics [113–117]. However, it should be noted that a modulation of the flame position due to this mechanism has not yet been observed in experiments. Confirming the presence of this mechanism experimentally is therefore a key objective of this thesis.

1.4 Research Objectives and Thesis Outline

The goal of this thesis is to identify the dominant flame-acoustic interaction mechanisms which drive high-frequency thermoacoustic instabilities in reheat gas turbine combustion systems. Reheat combustion is a key technology for the decarbonisation of the global energy infras-

tructure and it is therefore essential to avoid setbacks due to the unexpected occurrence of thermoacoustic instabilities. This is particularly relevant due to the increased use of alternative fuels as well as the need for greater operational flexibility, which can trigger such instabilities in previously stable combustors. In recent years there has been increased research effort in understanding the thermoacoustic characteristics of reheat combustors; however, the majority of these studies have focussed on the low-frequency regime. Recent industrial experience has shown that reheat combustors are indeed susceptible to high-frequency thermoacoustic instabilities so this is considered an important area for investigation.

The dual stabilisation mechanisms present in reheat flames make the prediction of thermoacoustic instabilities particular challenging. This is compounded by the acoustically non-compact nature of the flame in the high-frequency regime, where the dominant flame acoustic coupling mechanism is likely to be sensitive to the acoustic mode shape. This work therefore seeks to provide insight into the different driving mechanisms of high-frequency instabilities in reheat flames and determine which of these mechanisms are most likely to dominate thermoacoustic driving under real engine conditions.

This is achieved primarily through experimental means using a sequentially-staged combustor test rig which was previously constructed at the Chair of Thermodynamics of the Technical University of Munich. The test rig is used for the identification of the underlying flame-acoustic interactions which drive thermoacoustic oscillations. From the experimental data, the key driving mechanisms are identified and further investigated following these objectives:

- Characterise the acoustic response of the reheat test rig and identify conditions which lead to thermoacoustic instabilities.
- Investigate the flame dynamics of the unstable modes to determine the flame-acoustic interaction mechanisms which drive the thermoacoustic oscillations.

- Identify flame dynamic behaviour associated with modulation of the autoignition delay time by acoustic disturbances.
- Determine which driving mechanisms represent the greatest driving potential under real engine conditions.

The thesis is structured as follows. In Chapter 2, known flame-acoustic interaction mechanisms which are expected to be relevant for reheat combustors are described. This includes mechanisms for both the low- and high-frequency regimes as the low-frequency behaviours provides insights into the characteristics of partially autoignition stabilised flames when exposed to acoustic perturbations. In Chapter 3, the reheat test rig is described in terms of two combustion stages, the diagnostic techniques applied and the general characteristics of the reheat flame. Following this, the key techniques used for analysing the experimental data are presented in Chapter 4. The results and discussion begins with Chapter 5, where the thermoacoustic response of the reheat test rig is characterised. First, the sensitivity of the instabilities to operating conditions is discussed. Two unstable eigenmodes are then presented which are the focus of the study. Driving of each of these modes is dominated by a different flame-acoustic interaction mechanisms which originate from the two combustion regimes of the reheat flame (propagation and autoignition stabilisation). The study of these mechanisms is the focus of the next two chapters. Chapter 6 investigates the driving originating from the propagation stabilised parts of the flame. Next, Chapter 7 presents the investigation of the mechanism associated with the autoignition stabilised flame. In the first part of this chapter, the experimental observations are presented. To gain further insight into the underlying cause of the flame modulation observed in experiments, this is supplemented by a low-order modelling study which is described in the latter part of this chapter. Finally, a summary of the thesis is provided in Chapter 8.

2 Flame-Acoustic Coupling in Reheat Combustors

This chapter introduces several key mechanisms through which the flame and the acoustic field can interact and drive high-frequency thermoacoustic instabilities in reheat combustors. As the number of studies concerning high-frequency instabilities in reheat flames is limited, some of the mechanisms described here are based on research focussed on other combustor types or from the low-frequency regime. The first flame-acoustic coupling mechanism is the displacement of the flame by the acoustic velocity field and the flame deformation induced by this displacement, which is described in Section 2.1. Flame displacement and deformation has been observed as key sources of high-frequency driving in swirl flames but their significance for reheat flames is not yet well understood. Next, in Section 2.2, modulation of the flame heat release by acoustically-induced vortex shedding is presented as a thermoacoustic driving mechanism. This type of vortex shedding has also been previously observed for swirl-stabilised flames. In that case it was found that this phenomenon did not lead to any significant driving; however, due to the reactive nature of the shear layers in reheat flames, it is expected that this could be a potential source of driving. Finally, modulation of the autoignition flame by acoustic perturbations is considered in Section 2.3. This last mechanism is the least studied of those presented when considering the high-frequency regime; however, there have been several studies of the low-frequency response of autoignition flames to acoustic disturbances which form the basis of this section.

2.1 Driving due to Flame Displacement and Deformation

In experimental studies of swirl-stabilised flames, a displacement of the flame away from its stationary position was observed [96]. This flame motion was determined to be induced by the acoustic velocity field associated with the first transverse eigenmode in the combustion chamber. The motion was found to occur in-phase with the acoustic pressure, such that the maximum displacement of the flame towards the positive pressure antinode occurs at the pressure peak. This results in elevated heat release where acoustic pressure is high and the opposite is also true at the negative pressure antinode. As this satisfies the Rayleigh criterion, the flame displacement was identified as a thermoacoustic driving mechanism and a mathematical model for this mechanism was proposed [118].

Further numerical studies of this phenomenon revealed that the flame displacement leads to a second mechanism intrinsically linked to the first. As the flame is displaced towards to boundaries at the combustor walls, the heat release increases on the positive-pressure side due to local compression and decreases on the opposite side due to expansion. The induced deformation therefore represents a further oscillation of heat release which is in-phase with the effects of the displacement mechanism [119].

It is expected that these mechanisms will play a role in thermoacoustic driving of reheat flames as they are not associated with characteristics specific to the swirl-stabilised flames in which they were first observed. In any case where there is a strong acoustic velocity field, this should lead to displacement (and therefore deformation) of the flame. Numerical studies of Zellhuber et al. [60, 119] and Romero et al. [120] indicated that this should indeed be the case for reheat flames; however, this has not been confirmed experimentally. A more recent study suggests that these mechanisms, particularly the flame displacement, may contribute to damping rather than driving depending on the morphology of the flame and the acoustic mode shape [112]. This could explain why

no clear behaviour associated with the displacement and deformation mechanisms was observable in the preliminary experimental studies of Berger et al. [110]. The sensitivity of these mechanisms to key reheat combustion parameters was also investigated; however this indicated that both mechanisms are insensitive to changes in overall mass flow rate, fuel reactivity, mean flow temperature and adiabatic flame temperature [112].

2.2 Driving due to Acoustically-Induced Vortex Shedding

In addition to the initial observation of flame displacement by the acoustic velocity field, Schwing et al. [84] also observed rotating transverse patterns associated with periodic, acoustically-induced vortex shedding associated with high-frequency transverse instabilities. Later studies found that in the case of swirl-stabilised flames, strong flame quenching in the shear layers due to high stretch rates resulted in very low levels of heat release fluctuations [121], and the net effect of the vortex shedding contributed mainly to acoustic damping [59, 85]. However, in the case of reheat flames, it is assumed that quenching in the shear layers is negligible, allowing the possibility that modulation of the reactive shear layers by shed vortices could represent a source of thermoacoustic driving potential. This is supported by numerical investigations of reheat flames using large eddy simulation (LES) [119]. Furthermore, similar vortex shedding behaviour has also been associated with driving of high-frequency transverse modes in jet flames [86, 122–124].

The method by which this mechanism leads to thermoacoustic driving is described in the following. The transverse acoustic mode induces a transverse velocity field in the combustor. At the corners of the area jump at the inlet to the reheat combustion chamber, this transverse acoustic velocity interacts with the mean flow to produce vortices which are shed from this inlet and then convected downstream through the

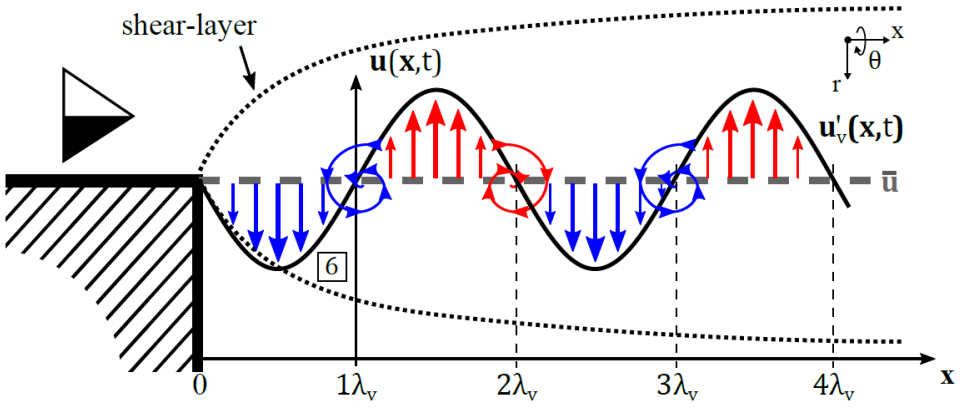

Figure 2.1: Illustration of the velocity induced by the acoustically-induced vortices along the shear layer. Adapted from Hofmeister [59].

shear layer. Due to the oscillatory nature of the acoustic velocity field, each subsequent vortex is of opposing sign. This results in a series of counter-rotating vortices as illustrated in Fig. 2.1. Between each pair of vortices, a velocity field is induced which alternates direction between each subsequent vortex pair. This velocity modulation results in a transport of reactants from the mean flow and recirculated combustion products through the shear layer, which in turn impacts the reaction progress. Where reactants are transported through the shear layer, heat release will increase and the opposite is true for where combustion products are transported as there are no further reactions taking place. As a result, a series of alternating patches of increased/decreased heat release forms.

Although this mechanism clearly produces a modulation of the heat release rate, it is unclear whether this would always lead to thermoacoustic driving. As seen in Fig. 2.1, multiple heat release patches of alternating sign are present simultaneously as they are convected downstream. Therefore, at any given instant in time, up to half of the modulated heat release patches are out of phase with the oscillating acoustic pressure. According to the Rayleigh criterion, these out of phase patches are con-

tributing to damping rather than driving. The net contribution of this mechanism therefore depends on the ratio of patches in and out of phase with the acoustic pressure. However, numerical studies of Zellhuber et al. [60] and Romero [112], as well as preliminary experimental studies of Berger et al. [110], indicate that there is indeed a net driving contribution associated with this mechanism. It is also indicated in Ref. [112] that this mechanism is sensitive to the mass flow rate. The increased mean flow velocity associated with elevated mass flow rate enhances the strength of the shed vortices, which results in greater convective transport through the shear layer. No sensitivity was observed in relation to the fuel reactivity, mean flow temperature or adiabatic flame temperature [112].

2.3 Driving due to Modulation of the Autoignition Flame by Acoustic Perturbations

The final mechanism to be presented in this chapter is the coupling between the autoignition flame and the acoustic pressure oscillations. This section is composed of two parts. The first considers the autoignition flame-acoustic interaction which have been identified for the low-frequency regime. Although these mechanisms are not directly relevant for the high frequency regime, they provide important insight into the response of autoignition flames to acoustic perturbations. In the second part, the proposed mechanism for the high-frequency regime is presented along with a discussion of numerical studies investigating the high-frequency response of the autoignition flame.

2.3.1 Autoignition Flame Response Studies in the Low-Frequency Regime

Studies on the autoignition flame response to acoustic perturbations typically focusses on the modulation of the autoignition delay time, which is the key parameter for determining the flame position in the combus-

tion chamber. A model based on this phenomenon was first proposed by Ni et al. [125] and this forms the basis of many later studies. In particular, this was expanded upon by Zellhuber et al. [60, 111, 126–128] in which the flame response to acoustic pulsations is numerically investigated (note that these studies also extend to the high-frequency regime). In those investigations, an analytical framework for modelling the response of autoignition flames was developed. From this, it was observed that the acoustic pressure fluctuations were altering the reaction rate of the fuel-air mixture between injection and ignition which directly affected the heat release of the flame. This has since been expanded on in later studies studies investigating reheat flames in industrial combustors. These studies confirmed the pressure sensitivity of reheat flames and also identified an even greater sensitivity to temperature fluctuations [113, 129, 130]. This agrees with studies investigating the stability of autoignition flames under varying operating conditions which previously determined that the parameter most significant for the autoignition delay time is the inlet temperature [34, 131, 132].

It is therefore clear that the autoignition flame is sensitive to both the acoustic pressure and also to temperature fluctuations, however several separate physical mechanisms exist by which the autoignition flame can couple to low-frequency acoustic disturbances.

- **Modulation of the reaction rate in the incoming fuel-air mixture.** In this mechanism, upstream travelling acoustic disturbances emitted from the flame cause a change in the reaction rate of the flow upstream of the flame front. Due to the pressure sensitivity of the autoignition delay time, the causes the flame position to oscillate and modulates the heat release rate [111, 117, 133].

- **Autoignition kernel formation upstream of the flame due to entropy waves.** In this case, the main cause of the flame modulation is the high temperature sensitivity [113, 129, 130]. Entropy waves generated from the first combustion stage are convected downstream and cause autoignition kernels to form in the mixing section [114].

This causes a rapid heat release fluctuation and flame position modulation in the autoignition flame when the kernels impinge on the flame front [116,134].[1]

- **Coupling between the first stage and reheat flames.** The unique nature of sequential combustion systems where two flames are present allows the potential for coupling between the two combustion stages [137]. Similarly to the previous mechanism, entropy waves originating in the first stage produce a response in the reheat flame. The resulting flame modulation produces upstream travelling acoustic waves which can interact with the first stage and produce further entropy disturbances.

- **Fuel jet flapping** Upstream travelling acoustic waves generated from the first stage flame induce velocity fluctuations of the fuel jet at the injection location. This causes fuel jet flapping which leads to equivalence ratio fluctuations which are convected to the reheat flame and result in heat release oscillations. This also modulates the residence time of the fuel-air mixture and periodically triggers autoignition kernel formation in the mixing section, further modulating the heat release rate [114,115,138].

2.3.2 Autoignition Flame-Acoustic Coupling in the High-Frequency Regime

Similarly to the response in the low-frequency regime, the sensitivity of the autoignition delay time to pressure and temperature disturbances is expected to play a key role for the flame-acoustic coupling mechanism at high-frequencies. A direct correlation between the flame heat release oscillations and acoustic pressure has already been identified in the numerical investigations of Zellhuber et al. [60,111] which also consider

[1] Entropy noise is a well-studied flame acoustic feedback mechanism where impingement of entropy waves on the combustion chamber outlet generates acoustic waves and forms a feedback loop [135,136]. The presence of a second flame in the reheat combustor allows a further mechanism for entropy waves to produce flame-acoustic feedback.

high-frequency transversal instabilities. However, the physical mechanism through which the flame and acoustics couple are significantly different from the low-frequency regime. This is mainly due to the fact that the mechanisms described in Section 2.3.1 are all based on convective effects which caused by modulation of the upstream flow properties in the mixing section and first stage flame. In the high-frequency regime, the oscillatory pressure field tends to be much more localised and as a result, the reheat combustion chamber can be considered to be acoustically-decoupled from the mixing section and first combustion stage. Therefore, the convective mechanisms are unlikely to be relevant for the high-frequency case.

Instead, it is proposed that the local reaction kinetics are instead modulated directly by the oscillating acoustic pressure field. This consideration of local reaction kinetics is also essential in the high-frequency regime due to the non-compact nature of the flame. As a result, it is not expected that there will be a uniform flame motion in response to the acoustic perturbations. Instead, the flame shape will deform as regions experiencing high or low acoustic pressure amplitudes will responds by moving up or downstream respectively. For example, for a first transverse mode which features an acoustic pressure antinode at each wall, one half of the flame would be displaced upstream and the other downstream simultaneously. It is also essential to consider the temperature sensitivity. As the first stage flame is acoustically-decoupled form the reheat stage, upstream entropy disturbances will be stochastic in nature and would not trigger a coherent response. However, the acoustic pressure oscillation will induce a fluctuation of the isentropic temperature. Typically these fluctuations are small but if limit-cycle oscillations reach large amplitudes then this can produce temperature oscillations which are significant for the highly temperature sensitive autoignition flame.

Although the oscillations of high-frequency modes are considered to be localised in the reheat combustion chamber, it must be considered that there is also a convective component to this local modulation of the reaction kinetics. As the high-frequency regime often concerns oscillations

in the kHz range, the fuel-air mixture likely experiences multiple oscillation cycles even in the short distance between the combustion chamber inlet and the flame front. Therefore, the history of pressure conditions along the flight path of a fluid particle must be considered and not just the instantaneous conditions at the time of ignition [125].

Numerical investigations of Zellhuber et al [60, 111, 119] and Romero [112] both indicate that autoignition delay modulation leads to a significant heat release modulation in phase with the acoustic pressure oscillations and therefore represents a significant source of driving. However, the effects of the ignition delay modulation on the flame position have not been observed in experiments. Romero [112] also found that driving associated with this mechanism is sensitive to mass flow rate, fuel reactivity, mean flow temperature and adiabatic flame temperature. The sensitivity to mass flow rate and adiabatic flame temperature are expected to be due to the relationship between these parameters and thermal power level. As the study by Romero [112] was conducted for an atmospheric pressure case, increased power density in the combustor aids in overcoming increased damping under these conditions, leading to the increased growth rate. The sensitivity to inlet temperature and fuel reactivity are expected as these are both key parameters for the autoignition delay time.

3 Experimental Setup

The experimental investigations presented in this thesis have been obtained from a lab-scale reheat combustor test rig under atmospheric conditions. First, the reheat test rig is described in detail in Section 3.1 in terms of the two combustion stages. Next the diagnostic techniques and the associated hardware are described in Section 3.2. Finally, the general characteristics of the stationary reheat flame are briefly presented in Section 3.3 to highlight the dual stabilisation mechanisms present and to illustrate how this must be accounted for when considering line-of-sight integrated optical measurements.

3.1 Reheat Test Rig

High-frequency flame-acoustic interaction mechanisms in reheat flames are investigated using the reheat test rig shown schematically in Fig. 3.1. A two-stage setup is implemented which imitates the constant pressure sequential combustion principle of the Ansaldo GT36 gas turbine [45], consisting of a vitiator, which represents the aerodynamically stabilised first combustion stage, followed by the reheat combustor. The test rig was originally developed in the work by F. Berger and P. Romero [110, 120, 139] and was designed to excite high-frequency transverse thermoacoustic modes in the vicinity of the reheat flame. In the following, the design and operation of each of the two stages are described.

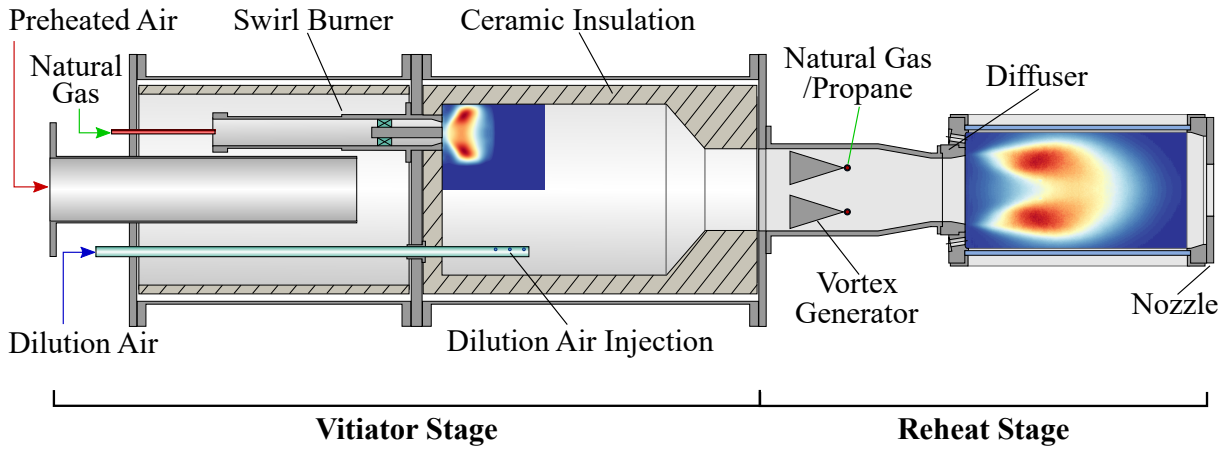

Figure 3.1: Sketch of the reheat test rig indicating the two combustion stages as well as key flow inlets and components. Adapted from Berger [110].

3.1.1 Vitiator Stage

The purpose of the vitiator is to provide controllable, high-temperature inlet conditions to the reheat stage under which an autoignition stabilised flame can form. This is implemented as a primary combustion stage followed by an air dilution stage in the post flame zone. A cross-sectional view of the vitiator is shown on the left of Fig. 3.1. Before entering the vitiator, air for the primary combustion stage is electrically preheated to $T_{pre} = 693\,\mathrm{K}$ to improve aerodynamic flame stabilisation which increases the possible air-fuel equivalence ratio in this stage, λ_{vit}. The preheated air enters a plenum and is evenly distributed between six lean premixed burners which utilise both swirl and bluff body stabilisation. The distribution of these burners in the vitiator can be seen in Fig. 3.2. A fuel lance is positioned at the inlet of each burner through which natural gas is injected into the preheated air flow. The fuel mixture is ignited by a torch igniter mounted in the side wall which is shut off after ignition is achieved. Each of the six burners provides a thermal power of $Q_{vit,burner} = 35 - 110\,\mathrm{KW}$ To provide greater control over the gas temperature entering the reheat stage, temperature staging is imple-

mented via six air dilution tubes which inject ambient air in the post flame zone. After the dilution air is added the air passes into the reheat combustor.

The parameters most important for the reheat inlet conditions are the mass flow rate of vitiated air and the flow temperature. This vitiator setup allows reheat combustor inlet mass flow rates in the range of $\dot{m}_{RC,in} = 0.35 - 0.55\,\mathrm{kg/s}$ and hot gas temperatures of $T_{RC,in} = 1200 - 1700\,\mathrm{K}$. These high mass flow rates are necessary to allow the high thermal power density required self-excited thermoacoustic behaviour at high frequencies in the reheat combustor. The thermoacoustic propensity of the vitiator is reduced by a high pressure drop of $\approx 20\%$ across the burners as well as the axially spaced injection positions of the dilution air. This ensures thermoacoustically stable operation of the vitiator stage allowing investigation of the acoustic behaviour of the reheat stage in isolation.

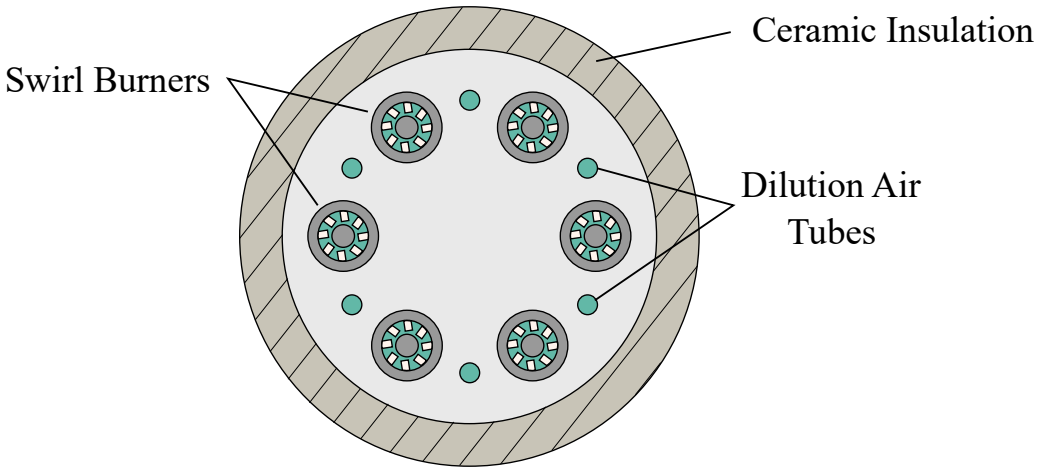

Figure 3.2: Sectional view of the vitiator indicating the positions of the six swirl burners and dilution air tubes. Adapted from Berger [110].

3.1.2 Reheat Stage

The hot vitiated gas from the vitiator first enters the rectangular mixing section of the reheat combustor through an orifice which influences acoustic coupling of the two combustion stages as well as the turbulence intensity in the mixing section. The mixing section is equipped with four delta-wing shaped vortex generators immediately upstream of the secondary fuel injection, which improve mixture quality and flow characteristics in the combustion chamber. At the entry to the reheat combustion chamber, the flow passes through a diffuser-shaped outlet. The geometry of the diffuser edge can be varied between a sharp-edged configuration and one with a rounded edge, which has implications for the strength of vortex shedding at the combustion chamber inlet. The area jump of $A_{CC}/A_{MS} = 2.1$ between the combustion chamber and mixing section, which takes place mainly in the vertical y-direction, promotes strong upper and lower recirculation regions, while the minor increase in the horizontal z-direction results in negligible flow recirculation in this direction. The combustion chamber is also of a rectangular cross-section, with a length, height and width of $L = 0.46\,\mathrm{m}$, $H = 0.25\,\mathrm{m}$ and $W = 0.13\,\mathrm{m}$ respectively. This quasi two-dimensional design promotes distinct zones of propagation and auto-ignition flame stabilisation, in addition to favouring purely transverse oscillations by suppressing rotating modes. Furthermore, the selection of non-integer multiples for the chamber dimensions avoids an overlap of higher harmonics between the orthogonal transverse acoustic modes. Damping of longitudinal modes is augmented by the addition of a nozzle at the outlet of the reheat combustion chamber which convectively dampens these modes while transverse modes remain unaffected due to their downstream attenuation resulting from the temperature increase.

The fuel for the second stage is a blend of natural gas an propane which can be varied between $x_{C_3H_8} = 0 - 50\,\%$ by mass. The addition of propane to the fuel blend alters the fuel reactivity, which in turn affects the autoignition propensity in the reheat flame [67]. To ensure sufficient mixing with the vitiated air cross flow, the fuel is surrounded by an annular jet

of shielding air to adjust the momentum ratio between the two streams. The reheat combustor can operate within an range of air-fuel equivalence ratios between $\lambda_{RC} = 1 - 1.8$ with a thermal power range between $Q_{RC} = 450 - 1000\,\mathrm{KW}$. The frame of the reheat combustion chamber is water cooled and additional impingement air cooling is included for the combustion chamber walls and the mixing section.

3.2 Diagnostics

The investigation of thermoacoustic instabilities in the reheat combustor requires spatially- and temporally-resolved diagnostic techniques. This is particularly challenging due to the high-temperature environment from which the measurements must be taken. The key properties to be measured are the acoustic pressure and the heat release of the flame, which are captured via water cooled dynamic pressure sensors and high-speed cameras respectively. Both the acoustic and heat release measurements are captured synchronously using a National Instruments PCI-4472 data acquisition card as illustrated in Fig. 3.3. This section provides details on the setup of these diagnostics.

3.2.1 Acoustic Measurements

Measurement of the pressure field in the reheat combustor is achieved using multiple dynamic pressure sensors at various positions in the reheat combustor as illustrated in Fig. 3.4. In most cases, four sensors are mounted in the faceplate of the reheat combustion chamber. These sensors are distributed to measure modes in either transverse direction in the rectangular cross section combustor. The measurement positions at the combustor faceplate is upstream of the flame zone and is located in the vicinity of the upper and lower recirculation zones. Due to limitations in the number of sensors available, as well as the number which can be sampled simultaneously, the acoustic field is reconstructed from

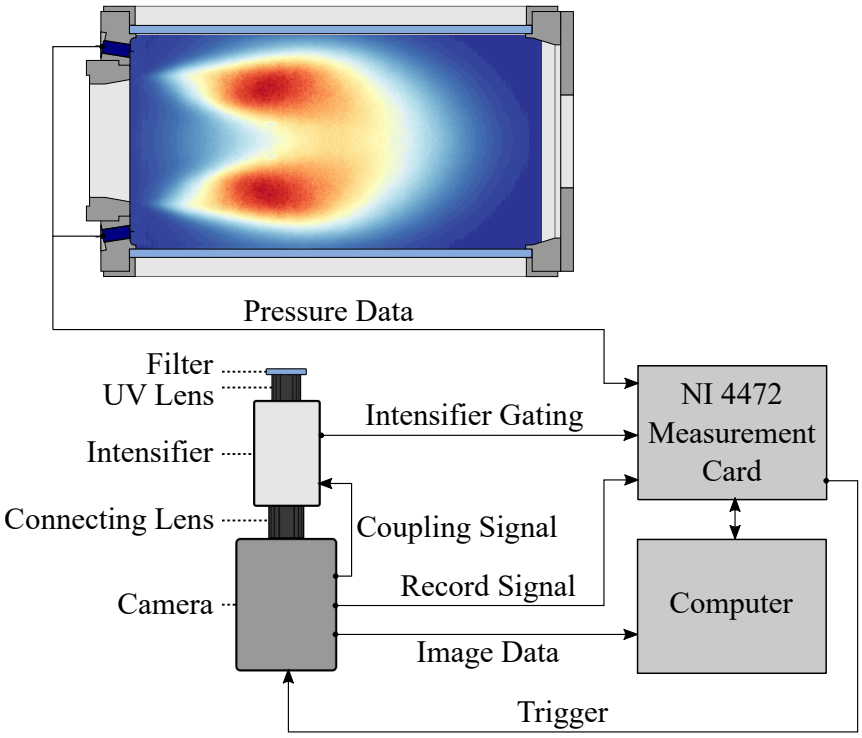

Figure 3.3: Illustration of the diagnostic setup for synchronous measurement of acoustic and heat release data.

these measurements via FEM using an approach which is described later in Section 4.3. Additional pressure probe positions are also included at various axial locations along the mixing section and combustion chamber to validate the FEM estimated field, particularly with regards to the upstream and downstream attenuation of the transverse modes due to the change in cross sectional area and the temperature rise.

PCB 106B piezoelectric pressure sensors are used for all acoustic measurements which have a sensitivity in the range of $35 - 45\,\mathrm{mV/kPa}$ and are sampled with a frequency of $f_s = 100\,\mathrm{kHz}$. For the measurements from the mixing section and the combustion chamber faceplate, these are mounted in water cooled PCB 064B06 adapters to avoid overheating, with the mounting ports on the faceplate also being water cooled. Due to much higher temperature along the combustion chamber wall, the PCB 106B sensors are instead mounted in modified adapters with additional

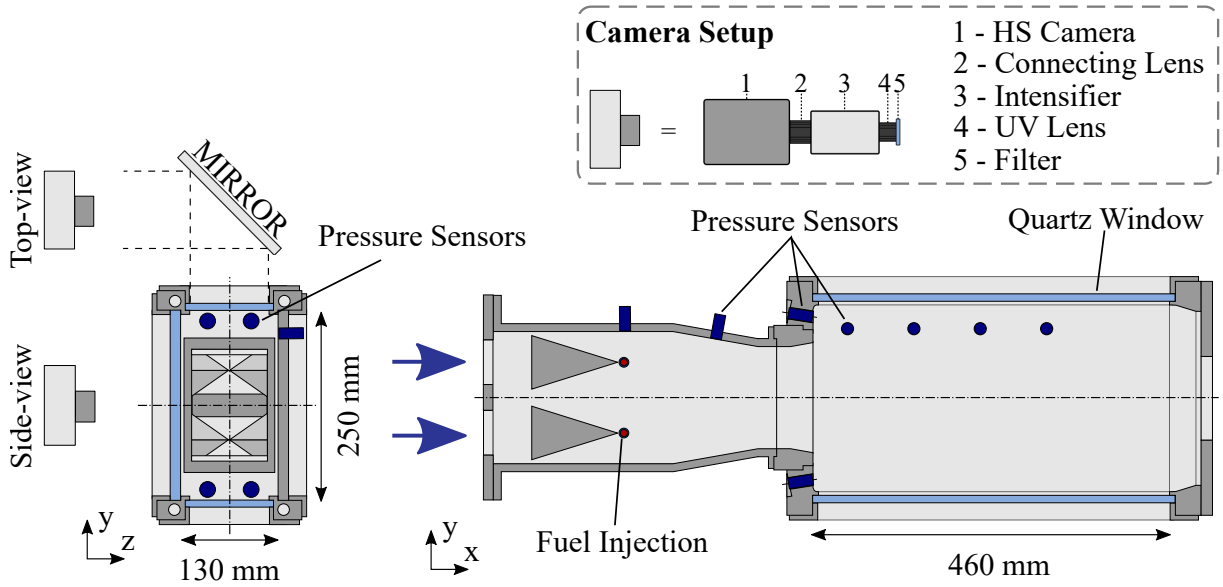

Figure 3.4: Illustration of the reheat combustor setup with the camera positions and instrumentation ports indicated.

water cooling channels and cooled mounting ports.

3.2.2 Bandpass-Filtered Flame Chemiluminescence

High-speed line-of-sight integrated chemiluminescence (CL) imaging is recorded synchronously with the dynamic pressure measurements for investigation of the flame dynamics. Images are recorded with a high sampling rate of 13.500 fps to allow sufficient temporal resolution of the flame dynamics associated with the transverse modes. The optical setup consists of a Photron FastCam SA-X2 high-speed camera coupled with a UVi 1850B image intensifier which is equipped with a 431 ± 5 nm interference filter mounted on a 45 mm UV lens. The selected interference filter allows detection of the carbyne (CH*) radical which typically appears where the local heat release is greatest in the combustion zone [140]. For the UV lens, a high aperture setting is applied to ensure sufficient depth-of-field such that the entire flame appears in sharp focus. The reduction

in light passing through the lens due to the high aperture setting is compensated for by increasing the intensifier gain. However, increased intensifier gain results in increased image noise. Therefore, CH* CL is preferred to OH* (hydroxyl radical) CL due to higher light emission at the corresponding wavelength in this case, allowing a reduction of the required intensifier gain.

Due to the technically premixed conditions in the reheat combustor, CL is not suitable as a quantitative measure of the local heat release rates. However, as the CH* CL intensity increases monotonically with heat release, the CL intensity still provides a qualitative measure of the spatial heat release distribution, which is sufficient for this investigation [141]. The reheat combustion chamber is equipped with quartz glass windows on all lateral sides, allowing observation of the flame dynamics from multiple perspectives. This is particularly important for the investigations described in this work due to the orthogonal nature of the two mode shapes being investigated. Images from the top-view were captured via a front surface mirror, coated to improve reflection at UV wavelengths. The spatial resolutions for each view are $2.6\,\mathrm{px/mm^2}$ and $1.5\,\mathrm{px/mm^2}$ for the side- and top-views respectively. Logical signals from the camera triggering and recording sequence, as well as the intensifier gating signal, are also sampled simultaneously with the pressure measurements. This allows the assignment of precise time stamps for each image relative to the acoustic measurements for the offline phase-resolved image processing technique described in Section 4.2.

3.3 Reheat Flame Characteristics

In this section the general characteristics of the reheat flame are briefly presented. Figure 3.5 shows time-averaged CL images from the side-, top- and rear-view perspectives. Due to the high inlet temperatures from the primary combustion stage, the reheat flame is partially stabilised by autoignition, while the area jump at the inlet to the reheat combustion

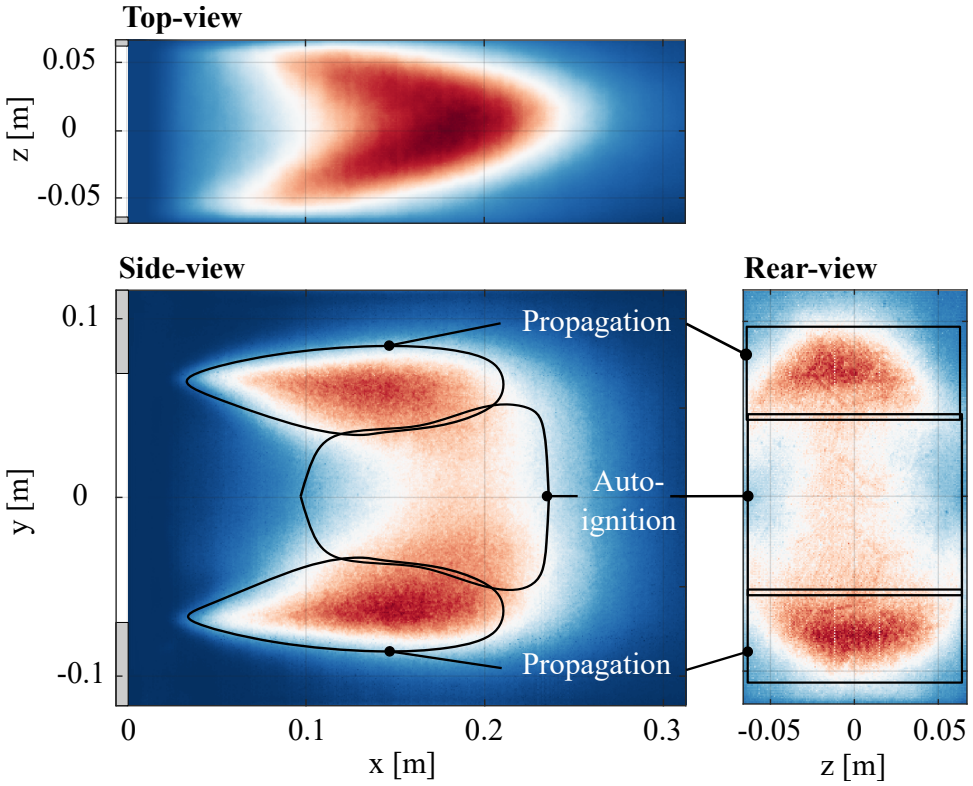

Figure 3.5: LOS-integrated, time-averaged CL images of the reheat flame from side-, top- and rear-view perspectives. Regions stabilised mainly by auto-ignition and propagation are indicated.

chamber promotes flow recirculation leading to additional propagation stabilisation. The quasi two-dimensional design of the reheat combustor allows distinction of these different combustion regimes without the need for tomographic reconstruction of the flame. The regions where each regime dominates are illustrated in Fig. 3.5. In the homogeneous core zone, the flame stabilisation is dominated by autoignition while the upper and lower portions of the flame are stabilised mainly by propagation. Note that the zones marked in Fig. 3.5 are for illustrative purposes and there is not a clear boundary between the stabilisation zones and it has been shown that autoignition behaviour is also present downstream parts of the propagation stabilised shear layer regions [114, 142].

From the side-view perspective, it is assumed that the heat release profile is approximately constant across the relatively narrow width of the combustion chamber. However, this does present a limitation when viewing the flame from the top, as CL intensity is now integrated through the propagation and auto-ignition stabilised flame zones. It is therefore not possible to distinguish which stabilisation zone any observed flame dynamics originate from. To mitigate this issue, rear-view images are investigated in tandem with the top-view images. This allows effects which vary across the chamber height to also be observed, although their axial extent cannot be determined from this orientation. The effect of varying integration widths must also be considered between the different views, where the long axial extent of the reactive shear layers can make them appear significantly brighter than the shorter auto-ignition stabilised core, despite comparable heat release quantities occurring in both regions.

4 Data Processing Techniques

This chapter introduces the techniques used to process the acoustic and optical data obtained from experiments for the analysis of thermoacoustic feedback mechanisms in the reheat test rig. First, the approach used to process the acoustic data obtained from the pressure sensors is presented. The output of this is used both for identification of unstable thermoacoustic modes in the combustor and also as inputs for the optical data processing techniques. Next, the method of identifying coherent heat release oscillations from the chemiluminescence imaging via the calculation of phase-resolved ensemble-averaged images is discussed. This allows investigation of flame dynamic phenomena which are coupled with the pressure oscillations and provides insight into the underlying mechanisms which drive thermoacoustic oscillations. Finally, the numerical estimation of the acoustic pressure field for the transverse modes is described which is based on both acoustic and optical measurements.

4.1 Identification of Acoustic Pressure Oscillations

To identify the components of the measured pressure signal associated with deterministic oscillations due to thermoacoustic instabilities, the time series data is decomposed into three components such that:

$$p(\mathbf{x},t) = \bar{p}(\mathbf{x}) + p'(\mathbf{x},t) + \tilde{p}(\mathbf{x},t) \tag{4.1}$$

where the measured pressure signal p consists of a time-averaged component $\bar{p}$ and two components which fluctuate with both position and

time. These fluctuating components represent a deterministically oscillating part p' and a stochastically fluctuating part $\tilde{p}$. The stochastic part can be attributed to turbulence and background noise. The deterministic component is of particular interest as this indicates the acoustic pressure.

The first step towards obtaining the acoustic pressure component, p', is to determine the modal frequencies of interest. The modes with the highest pressure pulsation amplitudes are identified from the Fourier transform of the pressure time signal. The acoustic response at the frequency of interest can then be isolated by applying a bandpass filter about this frequency. A symmetric passband about the central frequency is selected based on the spectral distribution to avoid other resonance frequencies close to the one of interest. As described in Section 3.1.2, this is not usually an issue as the test rig dimensions are selected such that there is no overlap between higher harmonics of the transverse acoustic modes. With the upper and lower passband thresholds selected, a rectangular filter is applied about the central frequency, setting the amplitude of all frequencies outside the passband to zero. An inverse Fourier transform is then applied to the filtered signal. Next, the mean component (found by taking a time average of the measured pressure signal), is subtracted from the real part of the resulting signal which gives the deterministic component of the pressure signal for a given frequency. Note that due to the large number of samples used for the averaging and the filtering processes, the stochastically fluctuating component is assumed to be negligible.

Additional information on the envelope amplitude and phase of the acoustic pressure oscillations can be obtained using the Hilbert transform [143]. This approach considers a time series signal as a projection of a complex analytical signal onto th real axis. In this case, the time series is the bandpass filtered acoustic pressure p' such that the analytic signal is expressed as:

$$P'(t) = p'(t) + i\hat{p}'(t) \tag{4.2}$$

where $\hat{p}'(t)$ is related to $p'(t)$ by the Hilbert transform, meaning a phase shift of 90° is applied to the original signal and then added to p' to form the complex signal P'. By converting Eq. (4.2) into trigonometric or exponential notation, it is possible to extract time-dependent envelope amplitude and phase information:

$$P'(t) = A(t)(\cos\varphi(t) + i\sin\varphi(t) = A(t)e^{i\varphi(t)} \tag{4.3}$$

where instantaneous envelope amplitude and relative phase are given by $A(t)$ and $\phi(t)$ respectively. The envelope amplitude is useful for identifying modal dynamics as it provides a time-resolved representation of the oscillation amplitude, making it easier to identify phenomena such as limit-cycle oscillations and intermittency. By comparing the difference in the instantaneous phase between the dynamic pressure sensors mounted at the reheat combustion chamber faceplate, it is possible to identify the orientation of the mode being analysed. In addition to this, these parameters are utilised as inputs for the image processing techniques described in Section 4.2.

4.2 Identification of Coherent Heat Release Oscillations

As was the case with the processing of the pressure signal in Section 4.1, the flame heat release fluctuations (represented by the intensity, I, of the CL images) are similarly decomposed into mean, deterministically oscillating and stochastically fluctuating components:

$$I(\mathbf{x},t) = \bar{I}(\mathbf{x}) + I'(\mathbf{x},t) + \tilde{I}(\mathbf{x},t) \tag{4.4}$$

The mean component can again be obtained simply by calculating the mean intensity over time.

$$\bar{I}(x,y) = \frac{1}{N}\sum_{k=1}^{N} I_k(x,y) \tag{4.5}$$

As the CL intensity is recorded as a 2D image, rather than a point measurement as was the case with pressure, this average is calculated for each pixel which can be constructed in to a mean image such as that seen in Fig. 3.5.

In order to identify modulation of the flame associated with the thermoacoustic oscillations, it is necessary to isolate the deterministic component of the CL intensity fluctuations I'. This is achieved by calculating phase-resolved ensemble-averaged images based on the associated pressure signal which is sampled synchronously to the image data

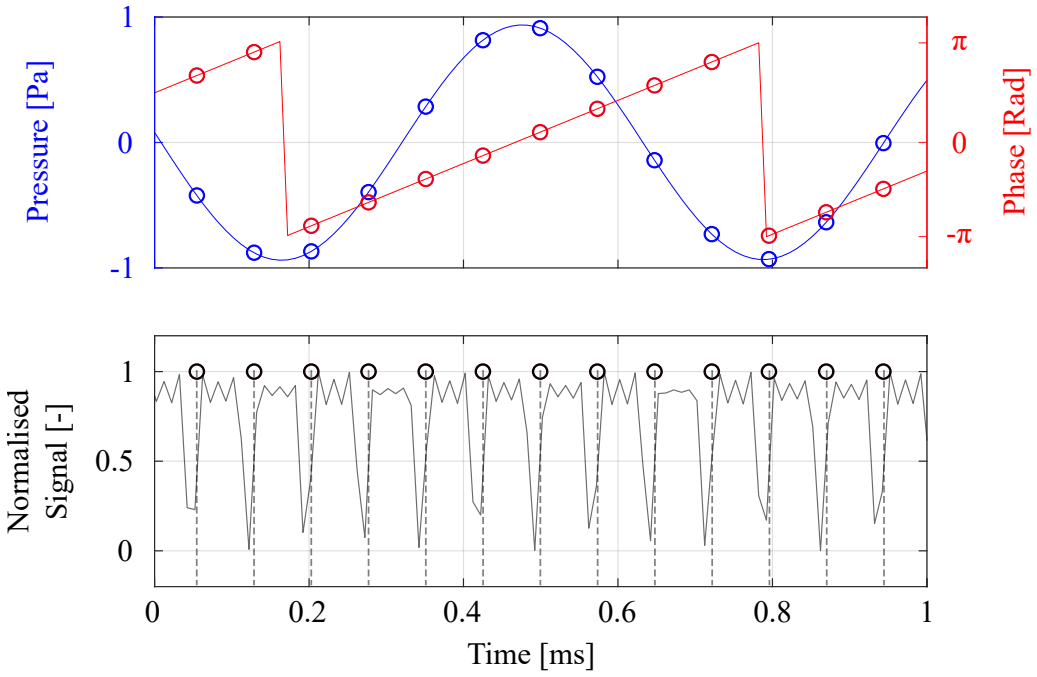

Figure 4.1: Procedure for correlating image and pressure data. The upper plot shows the pressure (blue) and phase (red) signals while the lower plot shows the intensifier gating signal II. Circles indicate the beginning of image exposures.

as described in Section 3.2.2. The first step in this process is to determine the points in time in the pressure signal at which each CL image was captured. This is illustrated in Fig. 4.1. The gating signal of the image intensifier, II, indicates the time at which an image was captured and the exposure time. During the processing, II is converted into a logical signal to more clearly identify times when images are being recorded. Due to the simultaneous measurement of pressure and image data, each image can now be associated with a corresponding pressure and envelope amplitude, as well as assigned a phase value relative to the acoustic oscillation based on the Hilbert transform of the pressure signal. Images are then sorted into 12 bins depending on their assigned phase. A mean image is then constructed for each bin to produce phase-resolved ensemble-averaged images which provide insight into the coherent flame dynamics associated with the acoustic oscillations at a particular frequency. The phase-locking procedure described here was originally developed by Güthe et al. [144] and has been used in a number of studies of thermoacoustic instabilities [86, 90, 92, 102].

4.3 Acoustic Field Estimation

As described in Section 3.2.1, the acoustic field is estimated numerically due to the limited number of dynamic pressure sensors which can feasibly be measured simultaneously. This is achieved by solving the Helmholtz equation via FEM. However, it is essential that the estimated pressure field accounts for the temperature rise due to the flame as this has major impact on the axial attenuation of transverse modes. In order to determine the axial pressure distribution, the evolution of the temperature in the axial direction must be known. However, combustion chamber temperatures are not measured experimentally, so an axial temperature distribution is instead estimated from the spatially-resolved CL data following the method introduced by Hertweck et al. [145]. Planar averages of the mean CL intensity in the transverse direction are first calculated, producing the axial intensity profile shown in the upper

plot of Fig. 4.2. The middle profile is then obtained as the cumulative sum of these planar averaged intensities along the axial direction. Due to the relationship between the CH* CL intensity and the heat release distribution [141], it may be assumed that the axial temperature rise follows the trend of this cumulative intensity profile. Therefore, this profile is scaled to the reheat combustion chamber inlet temperature and adiabatic flame temperature for the corresponding operating point as shown in the lower plot of Fig. 4.2. The calculated acoustic field of the reheat combustor is then scaled by the measured pressure values from the faceplate mounted pressure sensors. To validate the estimation of the axial pressure distribution, tests were run across a range of operation points with varying heat release distributions, which were varied mainly by altering the reheat combustor inlet temperature to change the autoignition delay time. Measurements were taken from the pressure sensors

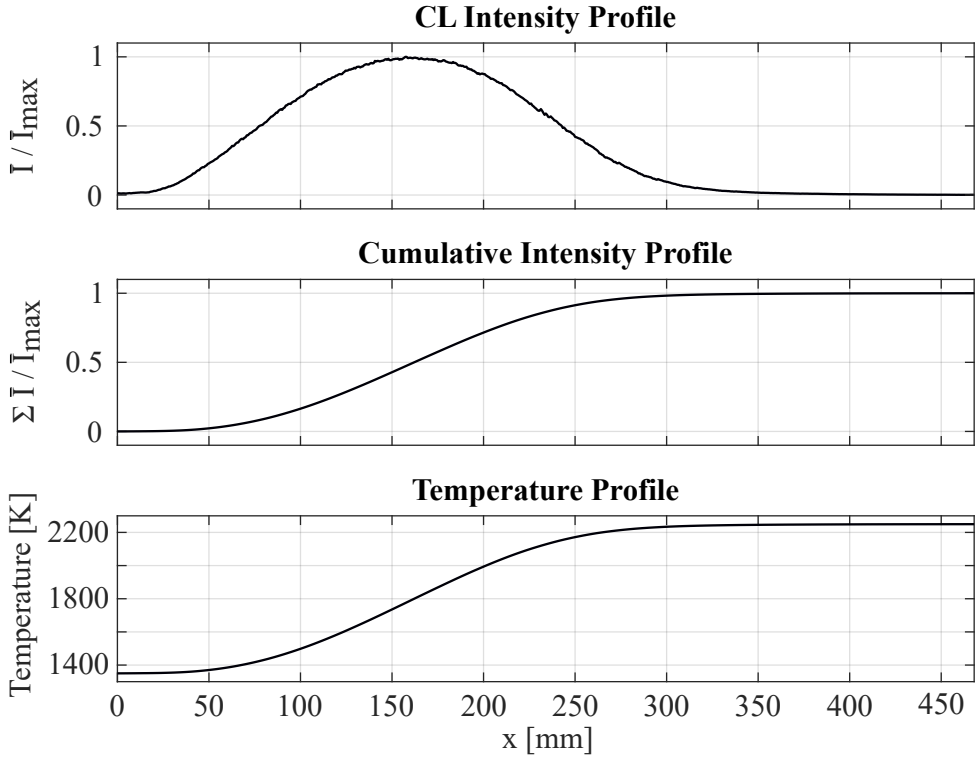

Figure 4.2: Approach for estimating reheat combustor temperature field from mean CL images.

mounted in the mixing section and along the reheat combustion chamber wall and compared with the calculated fields. This comparison is shown in Fig. 4.3, for the two first transverse modes in the reheat combustor at 1600 Hz and 3000 Hz. These two modes will be described in detail in the subsequent chapter. The $x = 0$ position in Fig. 4.3 corresponds to the first pressure measurement position in the mixing section which is located at the same axial location as the secondary fuel injection

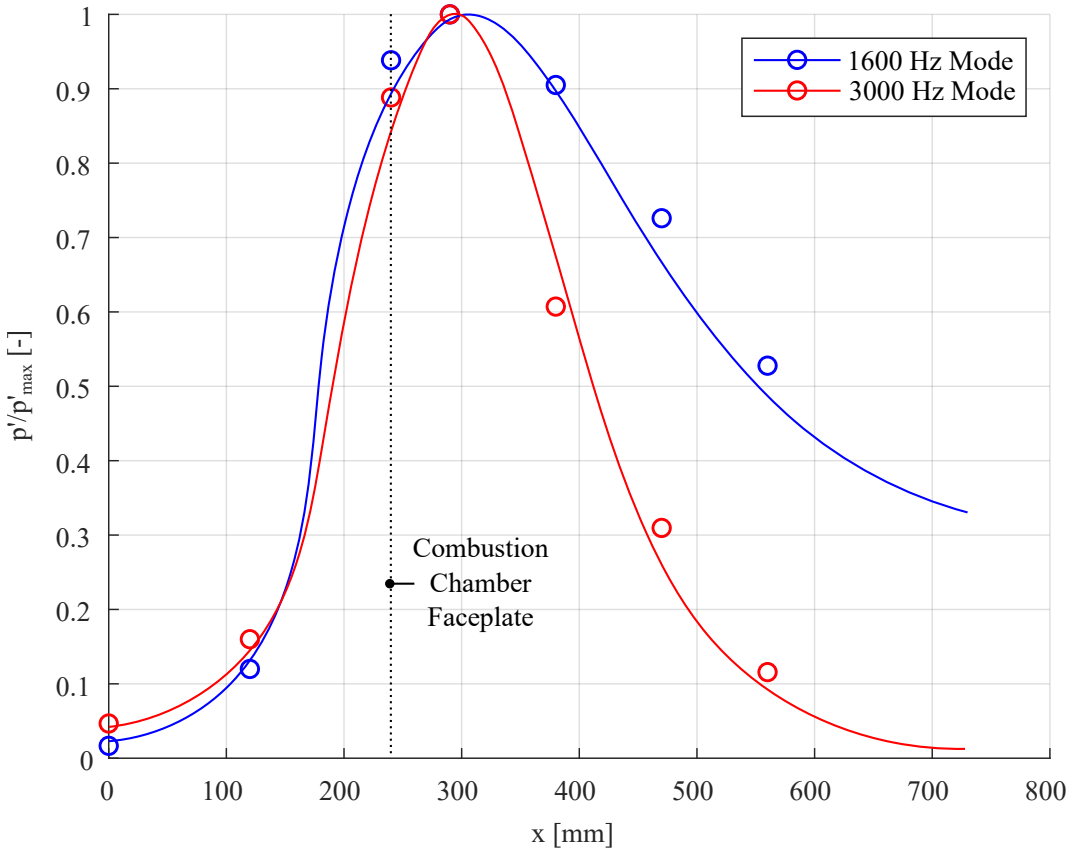

Figure 4.3: Comparison of the numerically estimated pressure (solid lines) along the combustor with the pressures measured by the axially distributed pulsation probes (circles) for the two first transverse modes in the reheat combustor at 1600 Hz and 3000 Hz. For ease of comparison, values are normalised by the maximum pressure amplitudes.

(see Fig. 3.4). The location of the sensor at the combustion chamber faceplate is shown by the dotted line. Good agreement was found between the experimental and numerical results indicating that the axial decay of the transverse modes is well captured in the estimated acoustic fields.

5 Reheat Combustor Thermoacoustic Response

In this chapter, two unstable thermoacoustic modes identified in the reheat combustor are introduced. In Section 5.1, the impact of the operating conditions of the test rig on the transverse thermoacoustic response is investigated. This mainly focusses on the influence of the thermal power level and the reactivity of the fuel blend with the goal of identifying operating conditions to be used to investigate the modes of interest. Next, the differences between the two modes is investigated in Section 5.2 by analysis of dynamic pressure time series measurements and numerically estimated acoustic mode shapes. Finally, in Section 5.3 the change in potential flame-acoustic interaction mechanisms depending on the acoustic mode shape is assessed to determine the likely sources of thermoacoustic driving for each mode.

5.1 Impact of Operating Conditions on Transverse Thermoacoustic Response

A preliminary study of the high-frequency thermoacoustic response of the reheat test rig used in this work was previously carried out by Berger et al. [110,139]. This identified operating parameters which significantly influence the thermoacoustic response of the reheat combustor. The results of this study were applied in the present work to select key operating conditions which display distinct thermoacoustic characteristics both in terms of the acoustic and non-compact flame dynamic response. The most important operating parameters for influencing the thermoacoustic

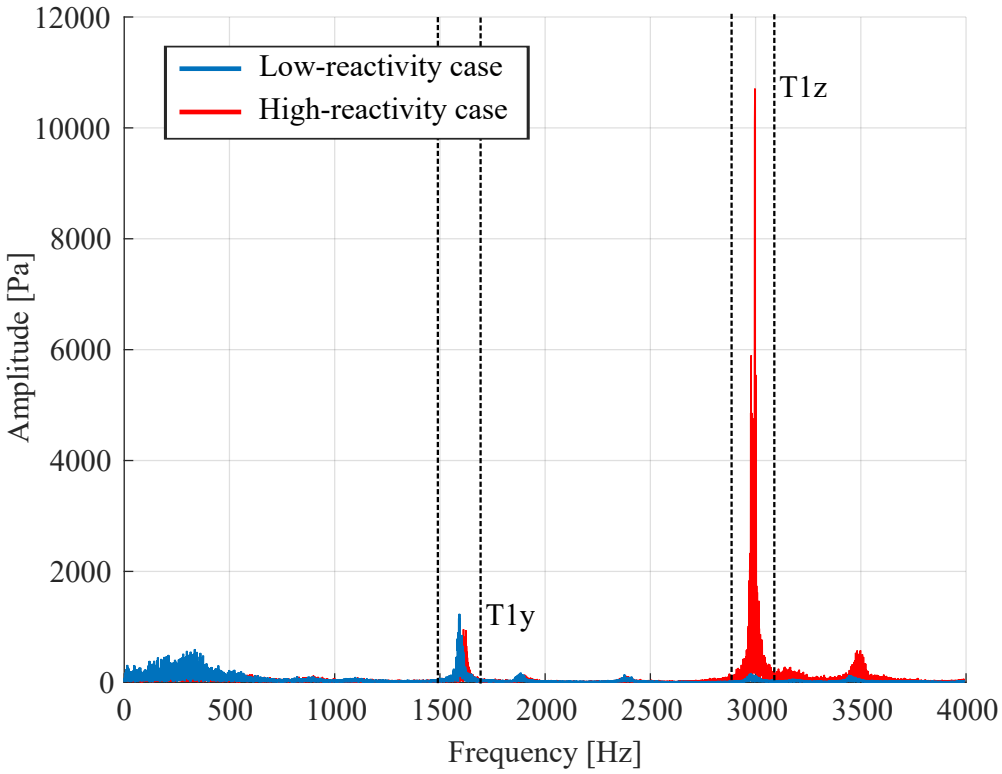

Figure 5.1: Amplitude spectra from two test conditions with varying fuel reactivity. Dashed lines indicate bandpass filter limits for each peak.

response were found to be thermal power level and fuel reactivity.

The amplitude spectra from two operating conditions are shown in Fig. 5.1. The main difference between these two operating points is the fuel reactivity, which is modified by varying the propane content of the fuel blend. For the low reactivity (LR) case the fuel propane content by mass is $x_{C_3H_8} = 5\%$ while the high reactivity (HR) case corresponds to a propane content of $x_{C_3H_8} = 25\%$. As the autoignition delay time is sensitive to fuel reactivity, the inlet air temperature is varied slightly such that $T_{RC,in} = 1350\,\mathrm{K}$ and $T_{RC,in} = 1330\,\mathrm{K}$ for the LR and HR cases respectively. This ensures that a consistent flame position is maintained. In both cases the test rig is operated with an inlet mass flow rate of vitiated air of $\dot{m}_{vit,air} = 520\,\mathrm{g/s}$ and a fuel mass flow rate of approximately

$\dot{m}_{fuel} = 16\,\mathrm{g/s}$, resulting in an air-fuel equivalence ratio of $\lambda = 1.25$. These settings produce a thermal power level in the reheat combustor of approximately $Q = 800\,\mathrm{kW}$.

Two distinct peaks can be observed from the amplitude spectra in Fig. 5.1, one at 1600 Hz and one at 3000 Hz. By comparing the pressure-phase relationship between the four pulsation probes mounted at the combustor faceplate, Berger [110] demonstrated that the 1600 Hz peak corresponds to the first transverse mode in the vertical y-direction while the 3000 Hz peak corresponds to the first transverse mode in the horizontal z-direction according to the coordinate system shown in Fig. 3.4. From this point, these will be referred to as the T1y and T1z modes respectively.

In both the high- and low-reactivity cases, the T1y peak is present at comparable amplitudes. This peak occurs across the entire operating range of the test rig and its pulsation amplitudes are largely independent of operating conditions, with only a small dependence on thermal power level. On the other hand, the high-amplitude T1z peak is only present in the high-reactivity case. This mode only exhibits significant amplitudes at high thermal power levels and with significant propane addition to the fuel blend. This is illustrated in Fig. 5.2 which shows the root-mean-squared value of the bandpass-filtered pressure signal at the T1z mode frequency with varying thermal power level and propane content. The thermal power in Fig. 5.2 is varied by altering the total mass flow rate through the reheat combustor while keeping the air-fuel equivalence ratio constant. With a propane content of 15% and above, pressure oscillation amplitudes increase dramatically at a thermal power level of $Q_{RC} \approx 680\,\mathrm{kW}$. At low levels of propane addition (5%) this sharp amplitude increase does not occur and there is only a slight rise in pulsation amplitude with increasing thermal power level. Increasing propane content beyond 15% only produces a slight increase in pulsation amplitude after the initial rapid amplitude rise and does not significantly change the power level at which the rise occurs. The main impact of propane addition to the fuel blend is a more reactive au-

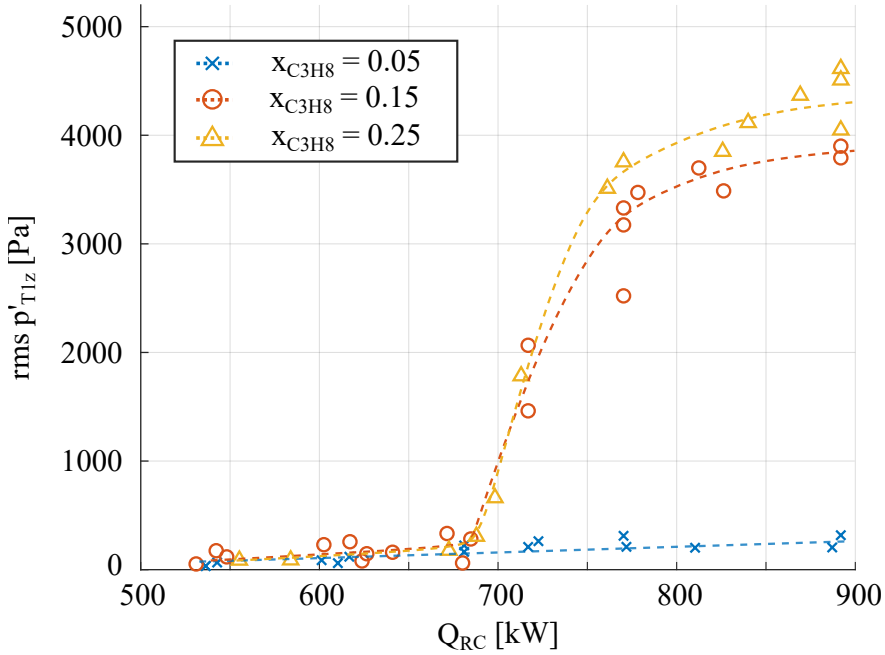

Figure 5.2: RMS of the bandpass-filtered pressure signal at the T1z mode frequency over thermal power level for different fuel blends.

toignition zone and shortening of the autoignition delay time [114, 146]. Therefore, the high amplitude pressure pulsations which occur with elevated fuel propane content can be attributed to heightened sensitivity of the autoignition flame to fluctuations of pressure and temperature. The different sensitivities of each mode to propane addition suggests that they are driven by different thermoacoustic driving mechanisms:

- As the T1y mode is largely independent of the fuel propane content, it is likely that the autoignition zone does not play a significant role in driving of the pressure pulsations. Driving must instead originate from the propagation-stabilised flame zones.

- The T1z mode is highly sensitive to propane content (and thus fuel reactivity), indicating that the autoignition flame zone contributes significantly to the thermoacoustic driving.

5.2 Transverse Modes Acoustic Characteristics

To gain a better understanding of the differences between the two modes, the acoustic characteristics of each will be discussed in this section. First, the marginally unstable T1y mode at 1600 Hz is described followed by the unstable 3000 Hz T1z mode.

5.2.1 T1y Mode Response

The upper part of Fig. 5.3 shows a sample of the pressure time series bandpass filtered about the frequency of the T1y mode. This sample was obtained from the low-reactivity case with a fuel propane content of $x_{C_3H_8} = 5\%$. The bandpass filter limits applied are $f_{T1y} \pm 100$ Hz as illustrated in Fig. 5.1.

It can be seen from the pressure time series in Fig. 5.3 that the amplitude of pressure oscillations at the T1y mode frequency fluctuate strongly over time. Irregularly occurring bursts of significantly higher envelope amplitudes occur surrounded by periods of low amplitudes. This can be seen more clearly in the spectrogram in the lower part of Fig. 5.3. The spectrogram shows the time-dependent frequency content in the filtered pressure signal and was calculated using a window size of 1000 samples (10 ms) with an overlap of 900 samples (9 ms). These irregular bursts of high-amplitude behaviour consist of periodic pressure oscillations at the T1y mode frequency while the surrounding low-amplitude periods are dominated by stochastic fluctuations. This behaviour is characteristic of intermittency and is qualitatively similar to that seen in studies of intermittent thermoacoustic oscillations in swirl and bluff-body stabilised flames [147–151]. However, in this case the intermittent thermoacoustic oscillations of the T1y mode persist across the entire operating range of the test rig, rather than as a precursor to instability within a narrow range of operating conditions as it typically the case.

Fig. 5.4 shows the acoustic pressure field of the T1y mode estimated

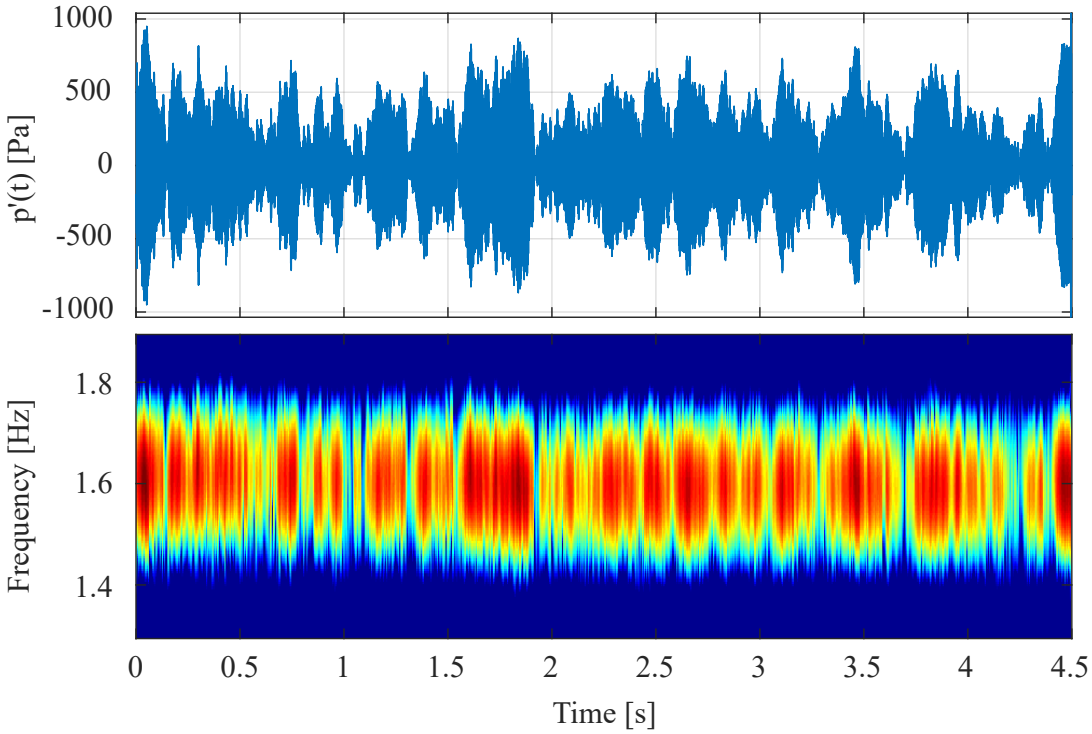

Figure 5.3: Upper: Sample of the pressure time series bandpass-filtered about the T1y mode frequency with envelope amplitude indicated by the black line. Lower: Spectrogram illustrating the bursts of high-amplitude periodic behaviour at the T1y mode frequency.

numerically using the estimation procedure described in Section 4.3. The estimated pressure field has been compared with measurements from axially-distributed pressure pulsation probes placed along the mixing section and the reheat combustion chamber for validation purposes.

The acoustic pressure field at 1600 Hz shows the typical form of a first transverse mode, with a pressure node along the horizontal centreline and antinodes at the upper and lower walls. This is an agreement with the mode assignment of the T1y mode based on the phase relationship between the four faceplate-mounted pressure sensors [110]. The strongest pressure oscillations occur in the region shortly after the area jump and from here the mode attenuates in both the upstream and

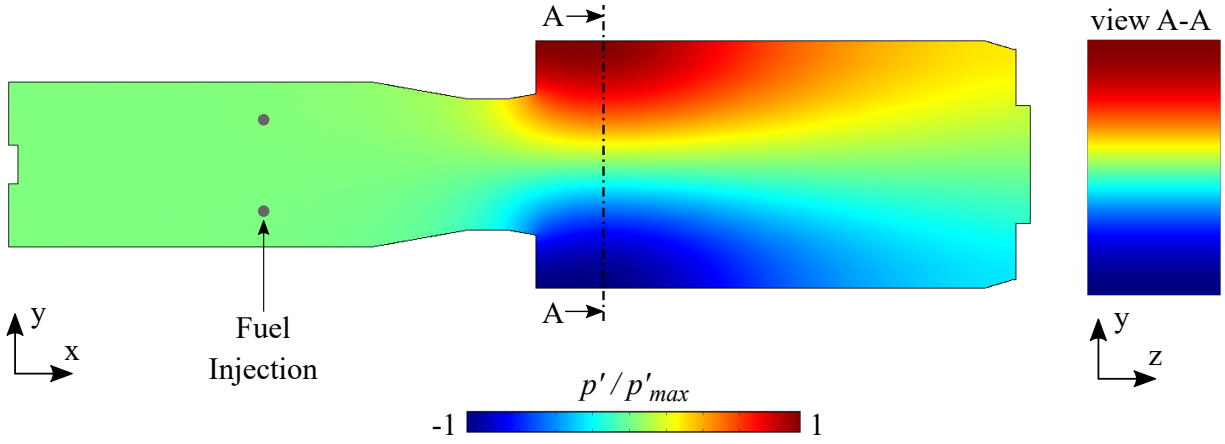

Figure 5.4: Acoustic pressure field estimation of the 1600 Hz T1y mode calculated via FEM.

downstream directions. The downstream attenuation is due to the sharp temperature rise through the reheat flame, which increases the sonic velocity, and therefore cut-on frequency, in the axial direction. In the upstream direction, the strong attenuation is due to the decrease in cross-section, which similarly increases the cut-on frequency. As a result of this upstream attenuation, the 1600 Hz T1y mode is effectively decoupled from the mixing section and the first stage flame. Most notably, this precludes the possibility for the T1y mode to induce equivalence ratio fluctuations in the incoming fuel-air mixture as the mode is completely attenuated far downstream of the fuel injection position. It can also be observed that the position of the pressure pulsation probes on the combustion chamber faceplate do not correspond to the location of the maximum oscillation amplitude.

5.2.2 T1z Mode Response

As described in Section 5.1, high power settings with a fuel propane content above 15% in the reheat combustor result in high pressure amplitudes at the T1z mode frequency. Fig. 5.5 shows a pressure time series sample bandpass filtered about this frequency with filter limits of

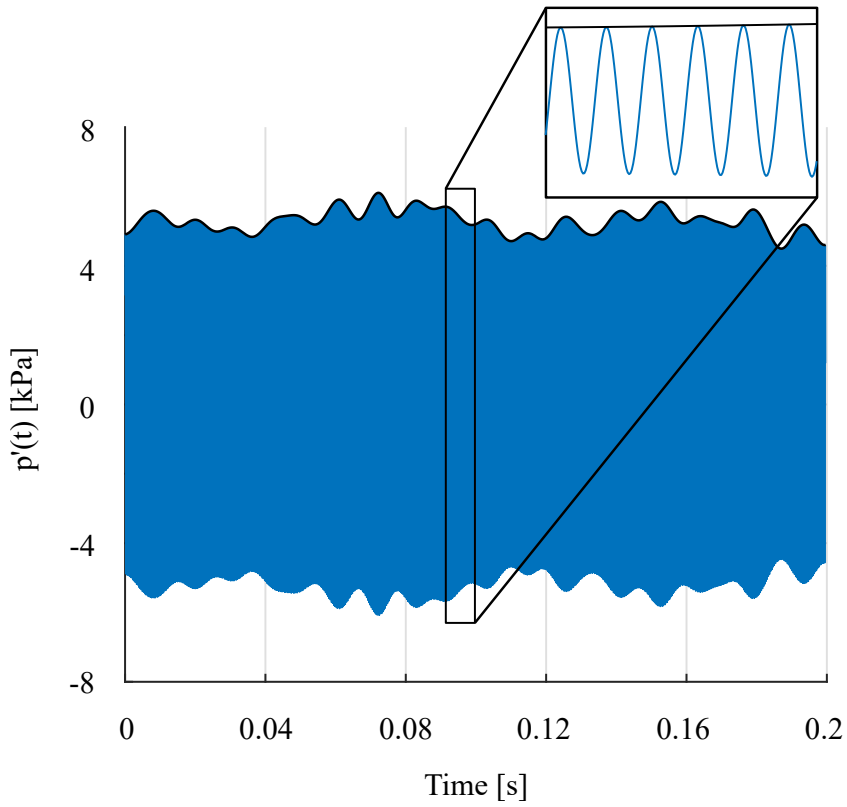

Figure 5.5: Sample of the pressure time series bandpass-filtered about the T1z mode frequency with envelope amplitude indicated by the black line.

$f_{T1z} \pm 100\,\text{Hz}$. This sample is taken from the high-reactivity test detailed in Section 5.1 with a thermal power level of $Q = 800\,\text{kW}$ and a fuel propane content of $x_{C_3H_8} = 25\%$. This corresponds to the strong T1z peak shown previously in the frequency spectrum in Fig. 5.1.

High-amplitude periodic oscillations are observed in the filtered pressure series and the envelope amplitude is indicated by the black line. The amplitude of the oscillations remains consistent over time with only small modulations which is typical of limit-cycle behaviour. At conditions below the occurrence of the sharp rise in pressure pulsation amplitudes shown in Fig. 5.2, these high-amplitude oscillations do not occur and this mode is thermoacoustically stable with a response dominated

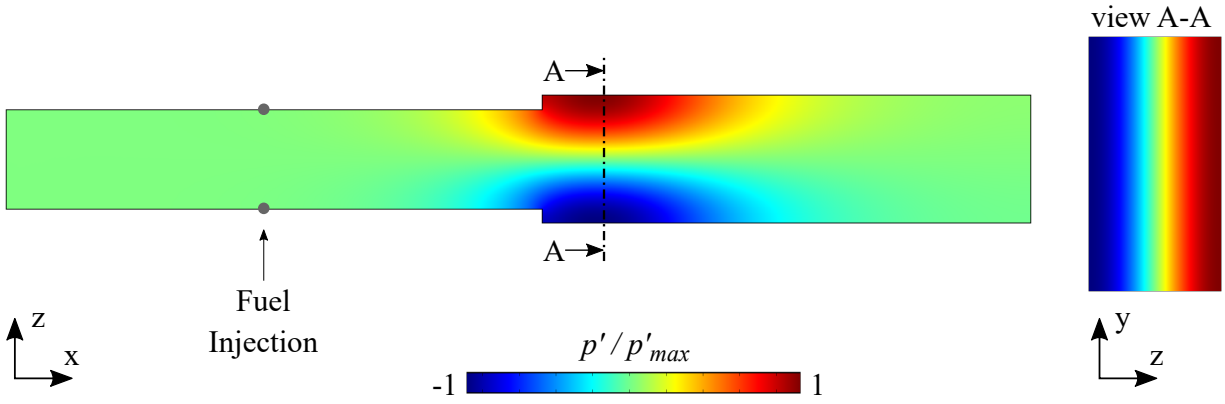

Figure 5.6: Acoustic pressure field estimation of the 3000 Hz T1z mode calculated via FEM.

by stochastic fluctuations.

The acoustic field of the T1z mode is shown in Fig. 5.6 calculated using the same approach as for the T1y mode in Section 5.2.1. As expected, this mode also exhibits the typical form of a first transverse mode in terms of the distribution of pressure nodes and antinodes. In this case however, the mode is oriented orthogonally to the T1y mode. This can be seen most clearly be comparing the sectional views A-A on the right between Fig. 5.4 and Fig. 5.6 which show the y-z plane. This is the reason for the different perspective of Fig. 5.6, which is from a top-down perspective showing the x-z plane. As with the T1y mode, the T1z mode is also attenuated in both the upstream and downstream directions. The downstream attenuation is stronger for the T1z case while in the upstream direction the pressure oscillation persist slightly further into the mixing section. However, the mode is still attenuated quickly enough that no pressure oscillations are observed at the fuel injection position and the mode is therefore also decoupled from the mixing section and the first combustion stage. This weaker attenuation in the upstream direction can be attributed to the smaller expansion in the z-direction at the area jump, which lessens the change in cut-on frequency of the mode.

5.3 Mode Shape Dependent Flame-Acoustic Interactions

To gain insight into the acoustic differences between the two unstable transverse modes, this section investigates the flame-acoustic interactions which dominate the thermoacoustic feedback for each case. Due to the dual-stabilisation mechanisms present in reheat flames, a change in the acoustic mode shape allows distinct interactions between the oscillating acoustic field and the different combustion regimes of the flame. This will be discussed qualitatively in terms of the Rayleigh Criterion, which indicates the potential for flame-acoustic interactions to contribute to thermoacoustic driving (see Section 1.3.2). If fluctuations of the unsteady heat release and acoustic pressure oscillations are phased such that constructive interference occurs, acoustic energy is added. For this to result in thermoacoustic instability, the acoustic energy addition must exceed its dissipation. In this section, this second requirement is considered, as the greatest potential for acoustic energy addition is achieved where the locations of strong unsteady heat release fluctuations overlap with regions of high pressure oscillations.

Figure 5.7 shows the mean contour of the reheat flame, obtained from CH* chemiluminescence imaging, superimposed on the acoustic pressure and velocity fields on the 1600 Hz T1y mode. By considering the different flame stabilisation regions, it is clear that the distribution of acoustic nodes and antinodes has a major influence on the possible flame-acoustic interaction mechanisms. Here, the upper and lower shear layer (see detail A in Fig. 5.7) are located in regions with high levels of acoustic oscillations. However, the autoignition core zone is only subjected to very small pressure oscillation amplitudes towards its upper and lower extents, while the centre experiences no pressure oscillations due to the pressure node here. This severely limits the extent to which the autoignition stabilised parts of the flame can contribute to driving of this mode. Since the propagation-stabilised shear layer regions experience a significant level of pressure oscillation amplitude, it is expected that heat release fluctuations from these regions contribute the majority

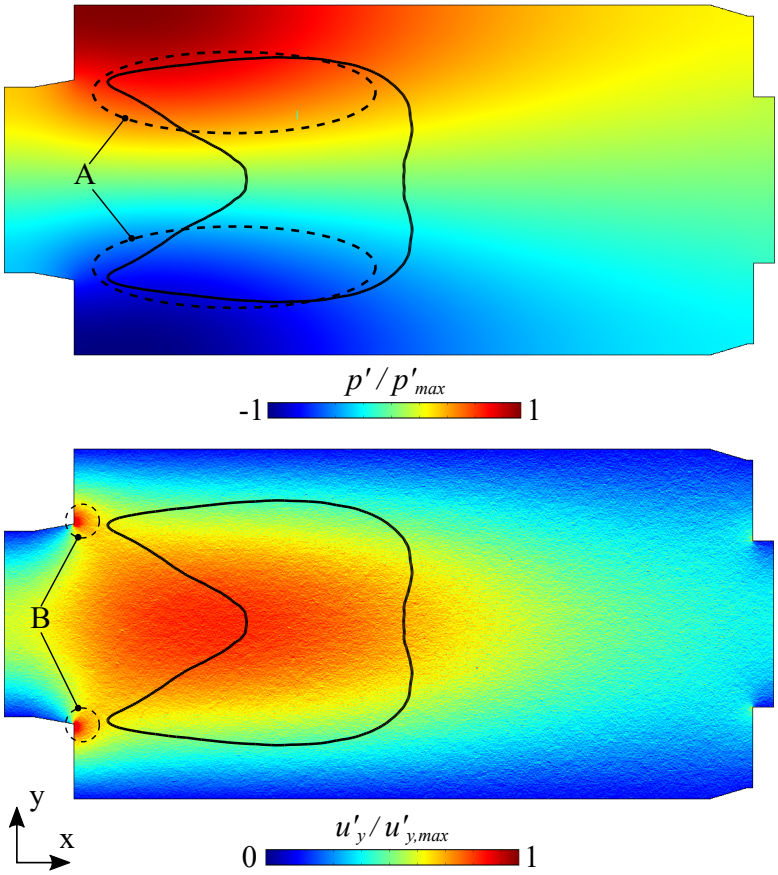

Figure 5.7: Transverse component of the 1600 Hz T1y mode acoustic pressure (upper) and velocity (lower) fields with the flame boundary illustrated by the black contour.

of the thermoacoustic driving of the T1y mode.

It is also important to consider the impact of the acoustic velocity field, which is shown in the lower part of Fig. 5.7. Since the position of nodes and antinodes changes between the acoustic pressure and velocity fields, the maximum transverse acoustic velocity occurs at the combustor centreline with minima at the walls. Regions of high acoustic velocity are observed at the edges of the area jump (see detail B in Fig. 5.7). This supports the hypothesis of Berger et al. [110] that modulation of the reactive shear layer regions in reheat flames is a result of acoustically-induced vortices shed from the edges of the area jump. This acoustic velocity dis-

tribution is also expected to give rise to a transverse flame displacement (and displacement-induced flame deformation) which has been found to drive high frequency thermoacoustic instabilities in swirl-stabilised flames [90, 91].

The difference in the orientation of the 3000 Hz T1z mode has considerable implications for the interactions between the different flame regimes and the acoustic field. Figure 5.8 shows the acoustic pressure and velocity fields of the T1z mode with the mean reheat flame contour from a top-down perspective. From this perspective, the limitations of the LOS-integrated nature of the CL images become more apparent as it is no longer possible to differentiate between the two combustion regimes. To address this issue, analysis of the flame dynamics of the T1z mode in later sections will also consider a rear-view perspective. Another consideration for the top-down perspective is the varying proportions of the integration width occupied by each flame regime. This is not an issue from the side-view as the width of the shear layers and the au-

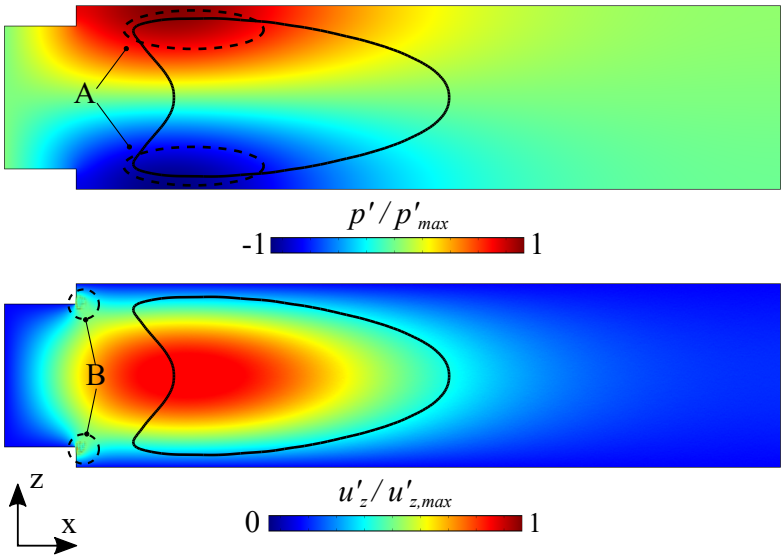

Figure 5.8: Transverse component of the 3000 Hz T1z mode acoustic pressure (upper) and velocity (lower) fields with the flame boundary illustrated by the black contour.

toignition core are approximately constant from the due to the quasi two-dimensional design of the reheat combustion chamber. However, as illustrated in Fig. 5.9, from the top-view the portion of the overall integration width occupied by the shear layers is narrow compared with that occupied by the autoignition core zone. As a result, the different flame regimes are disproportionately represented from this perspective. This explains why the upstream flame boundary is shifted downstream in Fig. 5.8 compared with Fig. 5.7, because the narrow z-extent of the upstream shear layer regions reduces the integral CL intensity at this position.

Despite the similar distribution of acoustic pressure nodes and antinodes between the T1y and T1z modes, the change of orientation relative to the flame has a pronounced effect on the pulsation amplitude levels and the potential flame-acoustic interactions associated with the limit-cycle oscillations. Both the propagation-stabilised shear layers

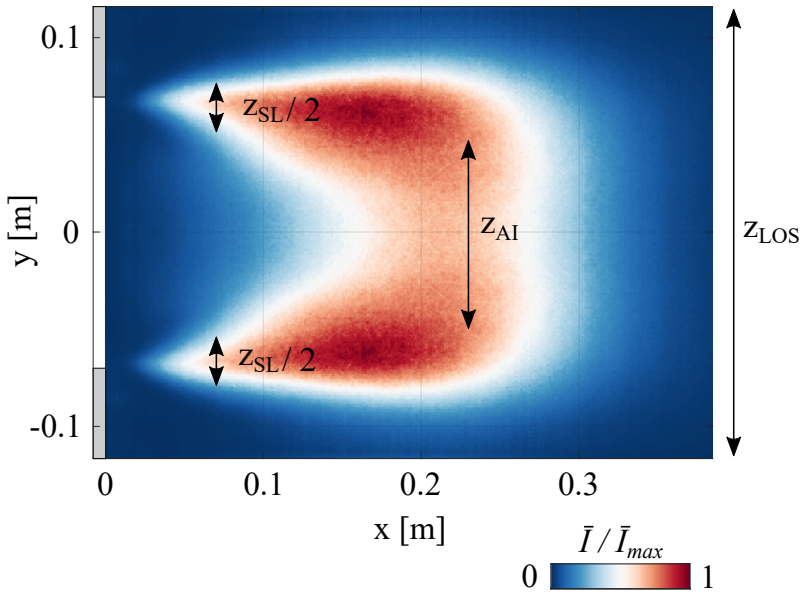

Figure 5.9: Illustration of the difference in relative integration widths associated with the shear layers and the autoignition zone for LOS integrated CL from the top-view perspective.

and the autoignition-stabilised core region are now in the vicinity of high-amplitude pressure oscillations, meaning each flame regime could potentially be modulated significantly by the acoustics. In this case, acoustically-induced vortex shedding from the edges of the area jump is unlikely to contribute significantly to driving of the T1z mode. The main reason for this is based on the geometry, specifically the very small area expansion in the z-direction compared with the y-direction at the combustion chamber inlet. Without the large step, the strong recirculation regions which give rise to the strong recirculation regions do not exist in the z-direction. Also, as the step is now closer to the acoustic velocity node at the walls, the low acoustic velocity in these regions (see detail B in Fig. 5.7) would not produce the strong acoustically-induced vortices which cause the shear layer modulation.

With the T1z mode, there is now an overlap of the high-amplitude pressure oscillations and the autoignition stabilised flame zone. This allows the potential for the autoignition flame to be modulated by the acoustic field. This modulation could lead to significant flame driving potential as autoignition flames have been shown to be very sensitive to fluctuations of pressure and temperature [114, 125]. As can be seen from detail A in Fig. 5.7, the upstream flame boundaries close to the walls are located in the regions where pressure oscillations are highest. This overlap suggests very high driving potential. The fact that significant pulsation amplitudes only occur in the high-reactivity case where the autoignition zone is strengthened indicates that the limit-cycle oscillations are associated with driving from the autoignition flame, rather than the propagation stabilised regions. The transverse velocity field shown in the lower part of Fig. 5.7 also suggests that there should be a driving contribution from the flame displacement and deformation mechanisms. However, these latter mechanisms are not sensitive to the reactivity of the fuel blend so it is expected that the majority of the driving is associated with modulation of the autoignition flame.

An additional difference which can be seen by comparing Fig. 5.7 and Fig. 5.8 is that the reheat flame occupies almost the entire z-extent of

the chamber but there are large regions without combustion in the upper and lower recirculation regions in the y-extent ($z_{fl}/z_{cc} \approx 0.95$, $y_{fl}/y_{cc} \approx 0.75$). The presence of these combustion-free regions limits the potential for flame-acoustic interactions since the highest amplitude pressure pulsations occur close to the walls. This is likely a contributing factor to the lower amplitudes experienced by the T1y mode compared with the T1z mode. This may be a fundamentally limiting factor for the driving potential due to reactive shear layer modulation as these non-reactive regions are essential for the recirculation regions which give rise to the propagation-stabilised shear layers. If the size of the area jump is reduced, this results in weaker shear layers closer to the acoustic velocity node at the walls which would consequentially weaken the vortex shedding and heat release modulation. Based on these observations, it is clear that multiple mechanisms are present which drive the high-frequency thermoacoustic instabilities and these vary in significance depending on the mode shape. Driving of the T1y mode is associated with the propagation-stabilised shear layer regions while the T1z mode driving is dominated by the response of the autoignition-stabilised core flame region.

5.4 Summary

In this chapter, the acoustic characteristics of two thermoacoustic modes in the reheat combustor are assessed with the goal of identifying the likely sources of thermoacoustic driving in each case. The outcomes of this investigation are summarised in the following:

- Two first transverse modes exist in the rectangular cross-section reheat combustion chamber, the 1600 Hz T1y mode and the 3000 Hz T1z mode. The T1y mode response is consistent across the operating envelope of the test rig while the T1z mode is highly sensitive to thermal power level and the reactivity of the fuel blend.

- The T1y mode exhibits intermittently unstable thermoacoustic behaviour, with irregular bursts of periodic pressure oscillations amidst periods dominated by stochastic fluctuations. This behaviour is independent of both thermal power level and fuel reactivity.
- At high thermal power settings and increased fuel reactivity, high-amplitude limit-cycle oscillations occur at the T1z mode frequency.
- From the numerically-estimated acoustic pressure field, which has been validated with experimental measurements, both modes are strongly attenuated in the upstream directions and are acoustically decoupled from both the mixing section and the first combustion stage. This precludes the possibility of equivalence ratio fluctuations or entropy waves as driving mechanisms.
- Based on the overlap of acoustic oscillation regions with the different combustion regimes of the reheat flame, thermoacoustic driving of the T1y mode must originate from the propagation-stabilised shear layer regions as the autoignition core is located in a region of very low acoustic oscillation amplitudes. The dominant driving mechanism is expected to be modulation of the reactive shear layers by acoustically-induced vortex shedding with flame displacement and deformation by the acoustic velocity field as secondary mechanisms.
- For the T1z mode, both combustion regimes overlap with regions of high acoustic oscillation amplitudes. However, the sensitivity of this mode to fuel reactivity indicates that driving is associated with the autoignition-stabilised core flame. Due to the high pressure and temperature sensitivity of autoignition flames, the dominant driving mechanism of this mode is expected to be modulation of the autoignition delay time by the acoustic oscillations.

6 Reactive Shear Layer Modulation due to Acoustically-Induced Vortex Shedding

In this chapter, the driving mechanism associated with modulation of the reactive shear layers by acoustically-induced vortex shedding is investigated. As described in Section 5.3, this mechanism is expected to be most significant for the 1600 Hz T1y mode based on the overlap of high amplitude acoustic pressure oscillations and the propagation-stabilised flame regions. In Section 6.1, the dynamic flame response at the T1y mode frequency is presented and discussed based on phase-resolved CL imaging to give insight into the significance of this mechanism for the overall driving of this mode. Next in Section 6.2 the intermittent nature of this mode is investigated by examining the change in flame dynamics over the intermittency cycle with the goal of identifying the cause of the intermittent behaviour.

6.1 T1y Mode Dynamic Flame Response

To determine the flame-acoustic coupling mechanism behind the thermoacoustic driving of the T1y mode, the spatially-distributed heat release is investigated in terms of phase-resolved CL intensity fields. As described in Section 4.2, instantaneous CL image frames are correlated with the simultaneously sampled dynamic pressure signal which allows evaluation of the flame dynamics during specific portions of the acoustic oscillation cycle. Due to the orientation of the T1y mode, images captured from the side-view (xy-plane) are considered in this sec-

tion. Twelve phase intervals are defined with corresponding ensemble-averaged images, each of which is an average of approximately 2,900 frames.

Figure 6.1 shows a series of ensemble-averaged CH* CL images from different phase intervals of the pressure oscillation cycle. There is a phase shift of 90° of the pressure signal between each of the presented images. The left column shows the mean image for each phase interval while the right column shows the corresponding oscillation of the CL intensity field. This is visualised as the difference between each of the ensemble-averaged images in the upper row and the overall mean image

$$\Delta \bar{I}_\phi = \bar{I}_\phi - \bar{I} \tag{6.1}$$

where $\bar{I}_\phi$ is each phase-averaged image and $\bar{I}$ is the overall mean image. The values of the intensity fields are normalised by the maximum intensity of the overall mean image to simplify comparison.

By examining the mean images in the left column of Fig. 6.1, a distinct modulation of the upper and lower shear layers can be observed. This observation is consistent with those seen in numerical investigations of high-frequency thermoacoustic sources in reheat combustors [119], where the shear layer modulation was a result of acoustically-induced vortex shedding. Similar vortex shedding was also observed in experimental studies concerning swirl-stabilised flames; however, in that case there was no significant modulation of the heat release due to flame quenching associated with high local strain rates [84, 121]. As a result, the vortex shedding phenomenon only contributed to acoustic damping in the case of the swirl flame [59, 85]. As this strong flame quenching is not present in reheat flames, it is expected that the vortex shedding does indeed produce a modulation of the heat release as indicated in Refs. [110,112,119]. This hypothesis is supported by experimental observation of similar flame-vortex interactions which contribute to thermoacoustic driving in jet flames [86, 123]. It should be noted that a similar response could also be a result of equivalence ratio fluctuations originat-

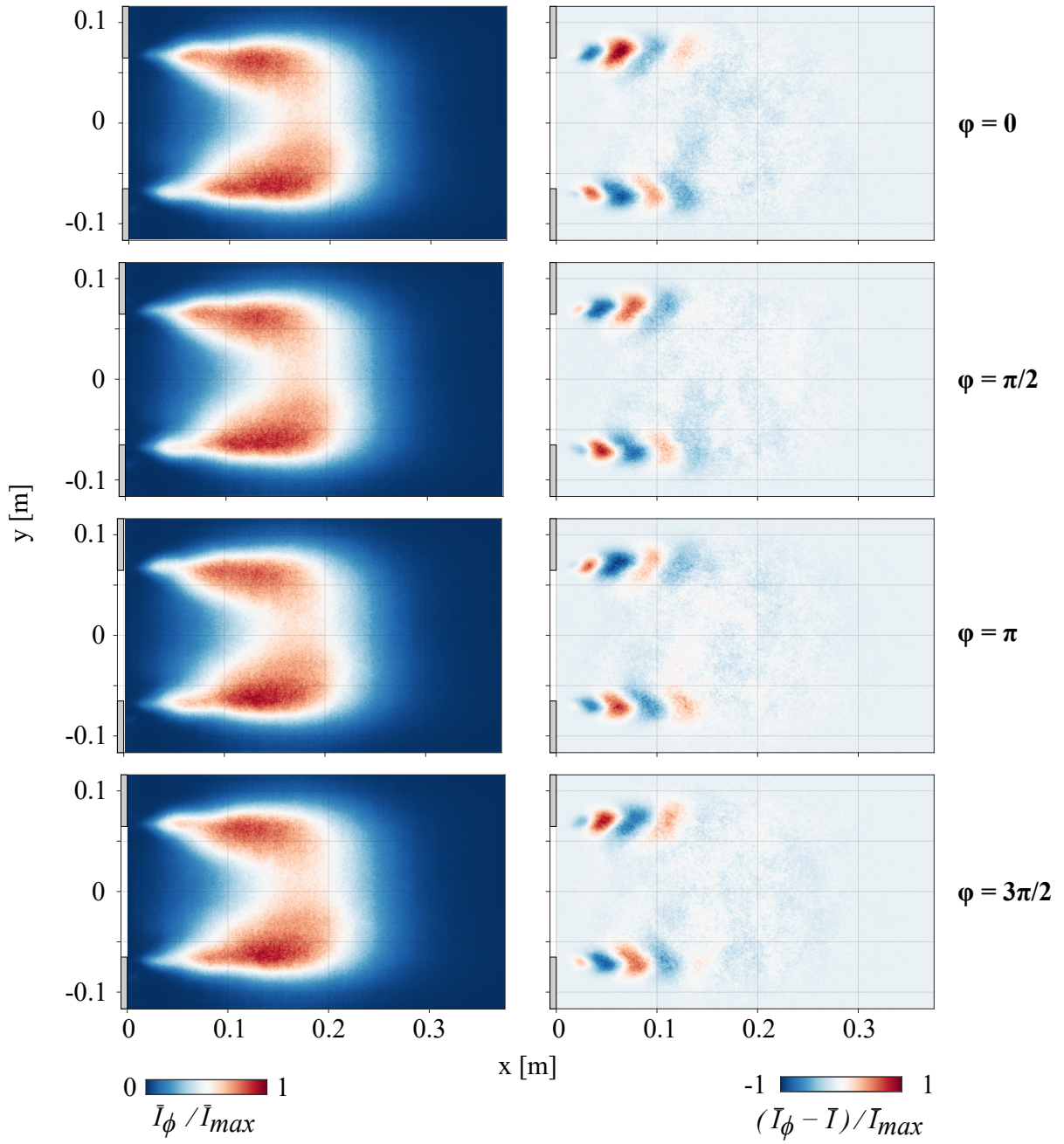

Figure 6.1: Phase-locked ensemble-averaged CL images of the flame at the T1y mode frequency for sample phase intervals (left) and the corresponding difference images (right).

ing from the mixing section caused by the oscillating acoustic pressure field. However, as shown previously in Section 5.3, the mixing section is acoustically decoupled from the transverse modes which precludes this possibility.

This modulation of the shear layers produces a sequence of alternating sign intensity patches which can be seen in the right column of Fig. 6.1. Tracking these intensity patches over time reveals they are convected downstream with the mean flow and are contained within the propagation-stabilised shear layer regions between the recirculation zones and the bulk flow. The tracking also indicated that the origin point of the patches is at the edge of the area jump at the combustion chamber inlet. It should be noted that the central autoignition-stabilised core flame region does not show any coherent flame modulation at this frequency. This can be explained by the pressure node at the combustor centreline which limits the potential for interactions between the acoustics and this flame regime (see Section 5.3). The alternating intensity zones are shed at the frequency of the T1y mode, with both a hot and cold patch being shed during each oscillation cycle. A further observation is that the alternating patches are antisymmetric about the combustor centreline. Counter-phase behaviour such as this is typical for the flame response to oscillations of the first transverse eigenmode which is likewise antisymmetric about the centreline.

To determine the degree to which the shear layer modulation contributes to thermoacoustic driving of the T1y mode, the phase relationship between the CL intensity oscillations and the acoustic pressure field is evaluated. Due to the antisymmetric nature of the T1y mode, only the intensity oscillations in the upper combustor half are considered. The CL oscillations for the two phase intervals corresponding to the maximum and minimum acoustic pressure level in this part of the combustion chamber are shown in Fig. 6.2. It can be seen that several regions of opposing sign exist simultaneously in this region, and it is therefore essential to know to what degree these opposing patches cancel each other out. The spatially-integrated values of oscillation intensity for both the

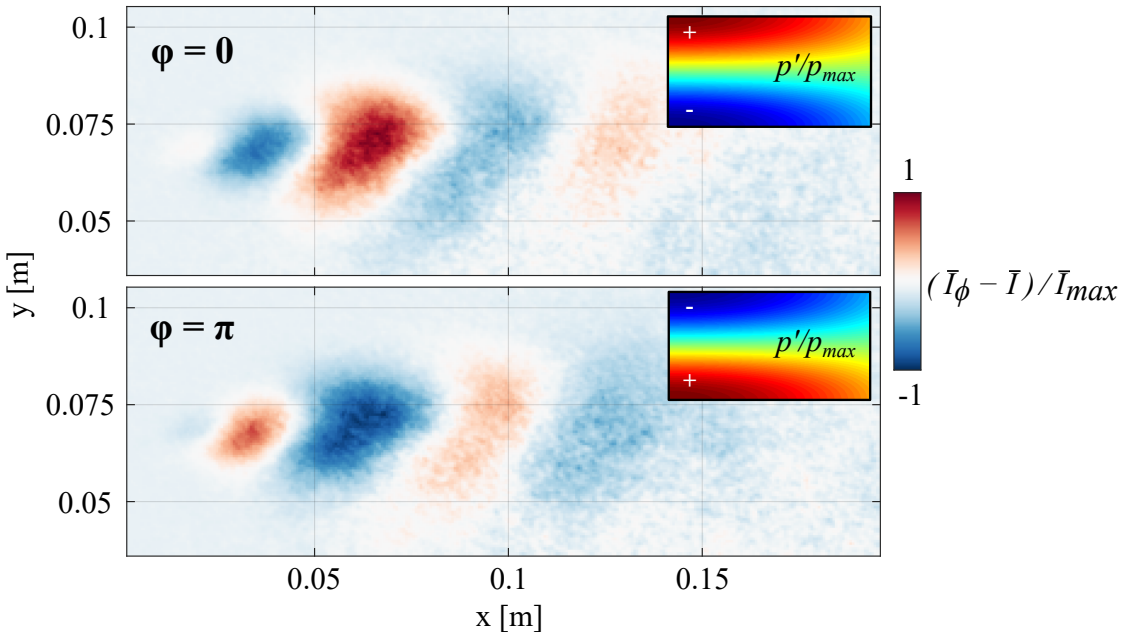

Figure 6.2: CL oscillations in the upper shear layer region for phase intervals corresponding to maximum (upper) and minimum (lower) acoustic pressure. Insets indicate the acoustic pressure distribution in the combustion chamber (calculated via FEM) during each phase interval.

entire upper combustor half and from only the upper shear layer region are calculated for each of the twelve phase intervals and then plotted over the T1y acoustic oscillation cycle in Fig. 6.3. Firstly, the contribution of the shear layer modulation to the overall heat release oscillation can be seen by comparing the oscillation intensity in the shear layer with that of the entire upper combustor half. This reveals that the majority of the heat release oscillation is contained within the shear layer regions, with only a very small contribution from the rest of the combustor. Secondly, the trend of the oscillation intensity, shown by the fitted curves, shows that the heat release oscillations occur in-phase with the acoustic pressure. The first point demonstrates that shear layer modulation contributes the majority of the total heat release oscillation, while the second point demonstrates the phase relationship between oscillatory heat re-

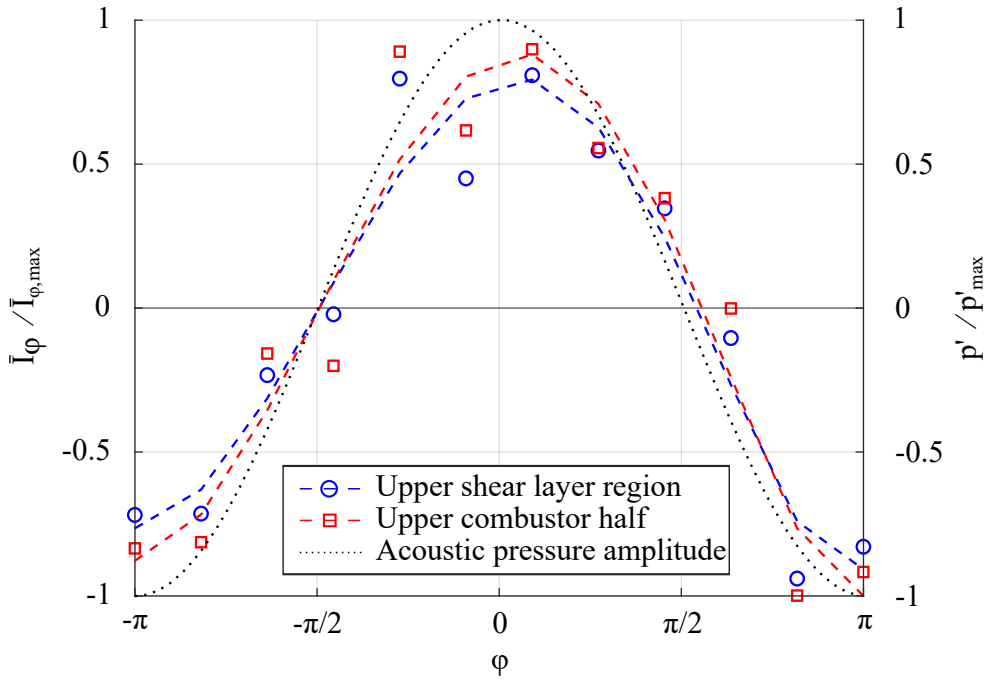

Figure 6.3: Normalised, spatially-integrated CL oscillation intensity over the T1y mode cycle in the upper shear layer region (blue circles) and the entire upper combustor half (red squares). The dashed lines are fitted in a least squares sense to the data points and the dotted line indicates the acoustic pressure.

lease and the acoustic mode satisfies the Rayleigh criterion. As a result, it is clear that the shear layer modulation due to acoustically-induced vortex shedding contributes positively and significantly to thermoacoustic driving of the T1y mode.

An additional point which should be noted is the absence of behaviour associated with transverse displacement and deformation of the flame by the acoustic velocity field. This was also true of previous experimental investigations on this test rig in Ref. [110]. It is possible that some influence of these mechanisms is present but is not visible due to the much stronger effects of the reactive shear layer modulation. The transverse flame displacement may become more prominent with increased oscillation amplitudes but as shown in Section 5.2.1, the T1y mode only

achieves moderate pulsation amplitudes regardless of operating conditions. It is therefore assumed that the the flame displacement and deformation mechanisms are secondary driving mechanisms with only a small contribution to the overall thermoacoustic driving of the T1y mode, while the majority of the driving originates from modulation of the reactive shear layers by acoustically induced vortex shedding.

6.2 Intermittent Flame Response

As shown in Section 5.2.1, the thermoacoustic response of the T1y mode is intermittent in nature, with irregular bursts of periodic pressure oscillations occurring amongst periods dominated by stochastic fluctuations. To better characterise the intermittent behaviour, four distinct intermittency conditions are defined based on the pressure data, with exemplary conditions and pulsation amplitudes shown in Fig. 6.4. The acoustic response of the T1y mode during each of the four conditions can be summarised as follows:

1. **Stochastic** - low-amplitude, stochastic pressure fluctuations
2. **Growth** - increasing envelope amplitude and tendency toward periodic oscillations over time
3. **Periodic** - high-amplitude periodic oscillations of the dynamic pressure
4. **Decay** - decreasing envelope amplitude and tendency towards stochastic fluctuations over time

6.2.1 Phase Space Trajectory Reconstruction from Acoustic Time Series Data

To gain deeper insight into the intermittent nature of the pressure pulsations, the phase space trajectory is reconstructed from the acoustic pres-

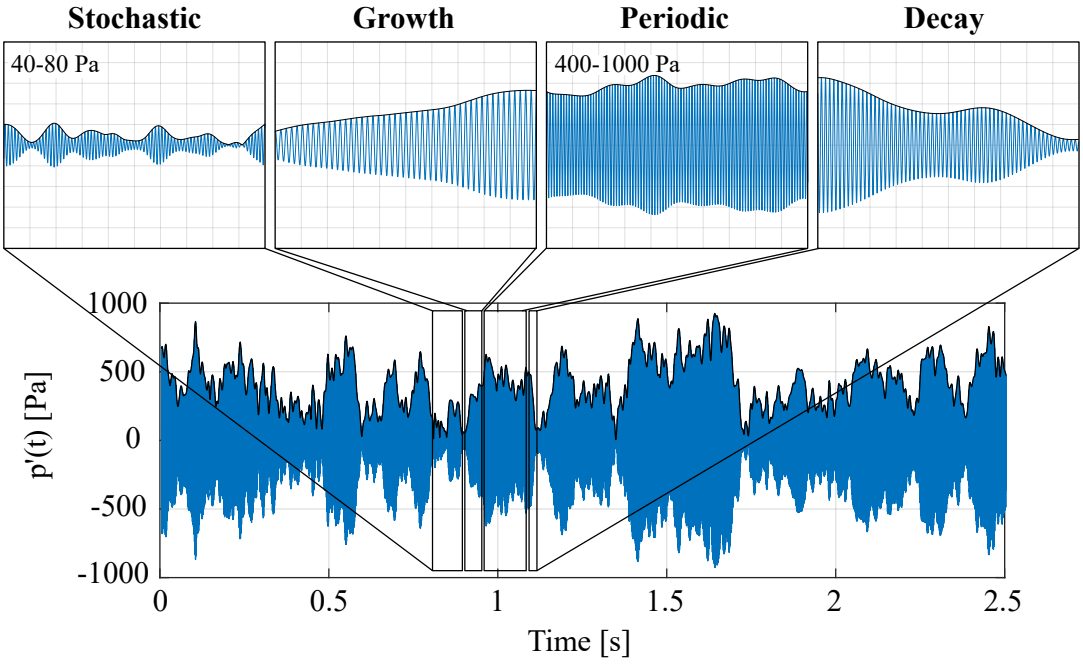

Figure 6.4: Bandpass-filtered pressure signal with sample regions corresponding to each of the four defined intermittency conditions. Typical pulsation amplitude ranges for the stochastic and periodic conditions are indicated.

sure measurements. The shape of this trajectory provides information on the dynamic system characteristics. This approach can be extended to provide quantitative details on the system response; however, in this work it is only used for qualitative assessment. A methodology analogous to that described by Kabiraj et al. [152] is applied which reconstructs the phase space trajectory from time series data, in this case from the pulsation probes at the combustion chamber faceplate. In this approach, the phase space trajectory consists of a series of n time-delayed vectors based on the dynamic pressure time series from the reference sensor, i.e.

$$Y_{PS} = [p'(t), p'(t+\tau_{PS}), p'(t+2\tau_{PS}), ..., p'(t+(dim-1)\tau_{PS})] \tag{6.2}$$

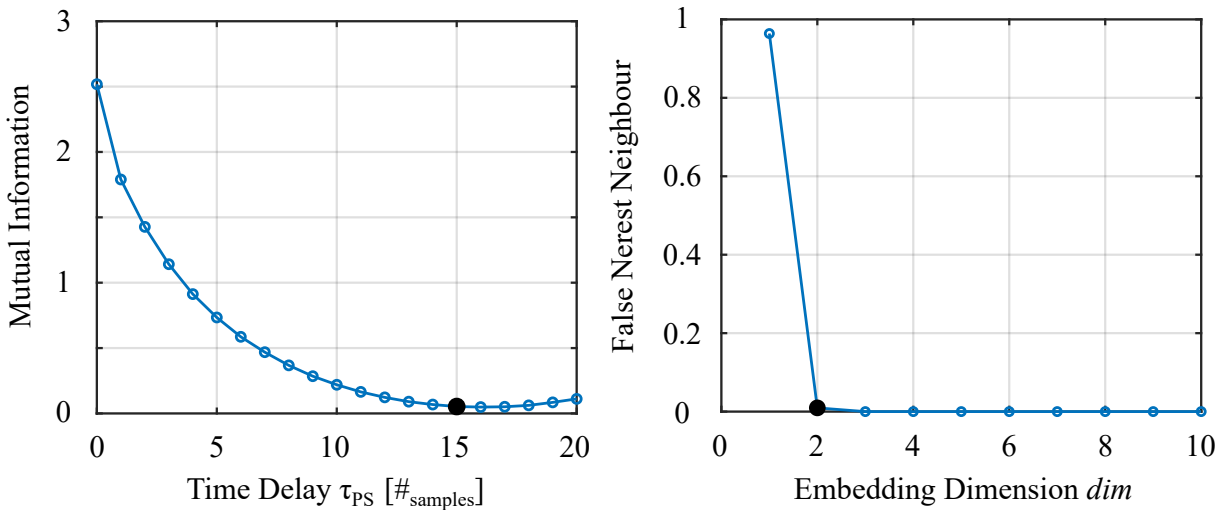

Figure 6.5: Selection of the phase space reconstruction parameters of time delay (left) and embedding dimension (right).

where τ_{PS} is the time delay between points along the trajectory and *dim* is the embedding dimension. The selection of the time delay, τ_{PS}, and embedding dimension, *dim*, must be optimised to ensure that the obtained trajectory is representative of the system dynamics and is not dominated by influences of false projections between phase space dimensions. As described by Kabiraj et al. [152], the selection of the time delay and embedding dimension is based on calculation of the average mutual information and the false nearest neighbour method, respectively. The time delay is selected as the first local minimum of the mutual information, which describes the degree of similarity between the measured signal, $p'(n)$, and the time-delayed vector, $p'(n + \tau_{PS})$. This is shown on the left of Fig. 6.5 with the corresponding minimum value highlighted, which equals approximately a quarter period of the T1y mode pressure oscillation cycle (0.15 ms). The right plot of Fig. 6.5 shows the false nearest neighbour test which indicates the percentage of points in the trajectory which erroneously appear close to other points. The embedding dimension is selected as the smallest dimension where this is almost zero. Due to a fairly low signal-to-noise ratio in the raw pressure signal, the bandpass-filtered signal around the frequency of the observed

intermittency is used for the phase space reconstruction. However, in order to mitigate the loss of the ability to distinguish between periodic and stochastic behaviour from the reconstructed trajectory, significantly wider bandpass filter limits are applied for the phase space reconstruction than described previously for the application of the Hilbert transform. These alternative limits are selected to be as wide as possible while also avoiding the frequency range below 500 Hz to improve the signal-to-noise ratio. The application of bandpass filtering does exclude system dynamics associated with frequencies outside the filter limits, most significantly the low-frequency range containing mostly broadband noise due to the high power densities. However, it is assumed that there is no significant interaction between the low-frequency and transverse modes so the filtering method applied allows an acceptable assessment of high-frequency dynamics.

Characteristic behaviours of each condition can be seen in the phase space trajectories shown in Fig. 6.6. As shown from the embedding dimension in Fig. 6.5, the reconstructed phase space is two dimensional due to the applied bandpass filter. Beginning with the stochastic condition, the trajectory is widely distributed and does not show any clear pattern (note that the roughly circular nature of the trajectory is due to the use of the bandpass-filtered pressure rather than the raw signal). Pressure amplitudes of the T1y mode in this condition are also low, seen in both the axis of the trajectory and in the inset amplitude spectrum. This type of grouping of trajectories close to the origin in an indistinct pattern is indicative that this state is linearly stable [151]. The trajectory during the growth condition shows a transition from low-amplitude, incoherent fluctuations towards increasingly high-amplitude periodic oscillations, indicated by the arrow showing the general trend of the trajectory. An increase in the acoustic energy at the T1y mode frequency can be seen from the amplitude spectrum. During the periodic condition, a narrow ring-shaped pattern emerges, as the trajectory follows the same general path but does not return to the exact same point at the beginning of each cycle. This is because the pulsation amplitudes do not rise and then settle at a constant amplitude, rather the amplitude tends to peak

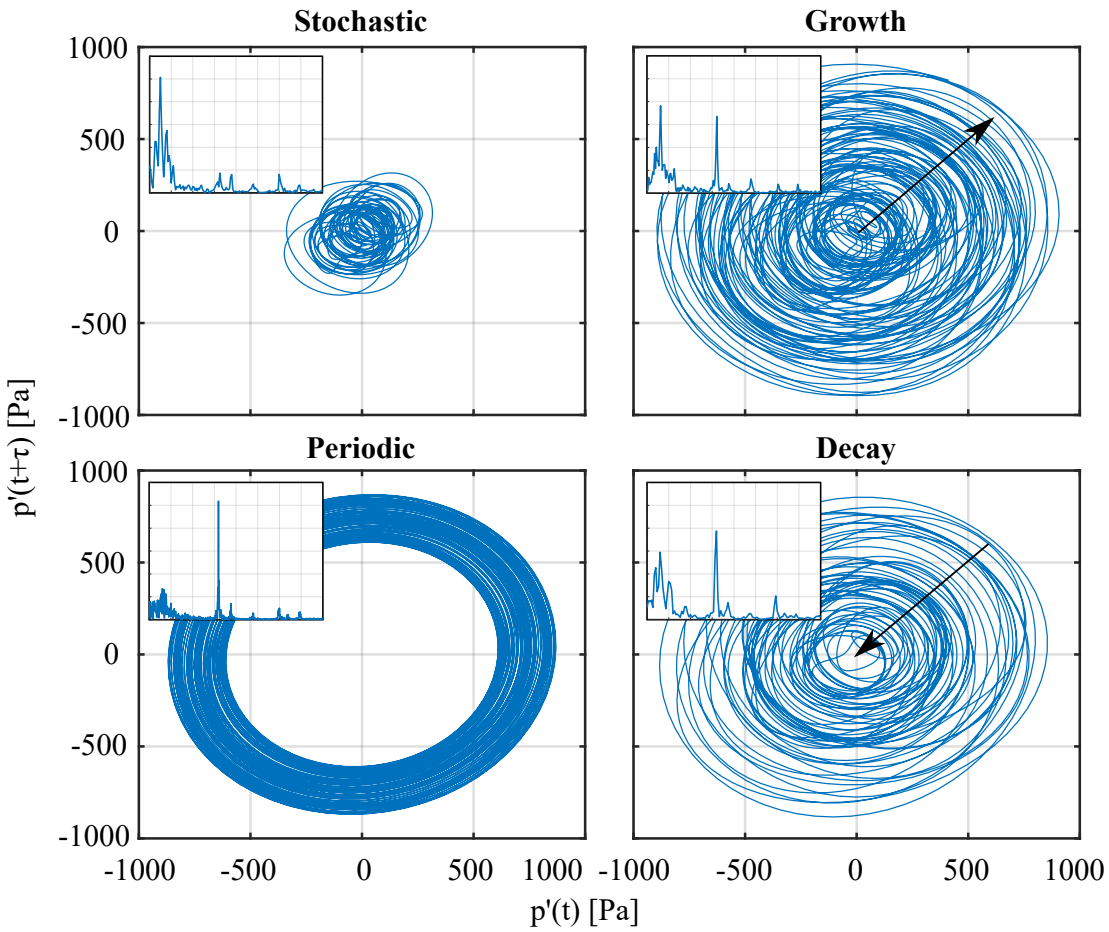

Figure 6.6: Reconstructed phase space trajectories for each intermittency condition. Arrows for growth and decay conditions indicate the trend of the trajectory over time. Inset amplitude spectra illustrate the relative strength of the T1y mode for each condition.

and then fluctuate somewhat before entering the decay condition. It is of note that the ring-shaped pattern formed by the trajectory indicates a thermoacoustically unstable state during the periodic condition [102]. Consequently, this condition also corresponds to the highest coherent T1y acoustic energy, where the peak at the T1y frequency dominates the other modes present in the amplitude spectrum. Finally, in the decay condition, similar behaviour to that seen during the growth condition is observed but with the trend in the opposite direction, indicated by

the arrow, with a move from high-amplitude periodic behaviour to low-amplitude stochastic fluctuations and reduced peak amplitude of the T1y mode. As seen in the time series in Fig. 5.3, after the decay condition the pressure signal returns to a state of stochastic fluctuations and the cycle repeats. It should be noted that the lengths of individual instances of each condition are irregular and can vary significantly between cycles.

6.2.2 Construction of Condition-Locked Ensemble-Averaged CL Images

For the evaluation of the flame dynamics during different states of the intermittent thermoacoustic behaviour, condition-locked ensemble-averaged images are calculated based on the four intermittency conditions defined in Section 6.2. The approach used for the identification of these conditions from the filtered pressure signal is illustrated in Fig. 6.7. In this approach, the key parameter used for the condition identification is the pressure oscillation amplitude. In particular, the gradient of the envelope amplitude over time is of interest. First, the envelope is smoothed by a locally-weighted linear regression to remove most of the small scale peaks which are not significant for condition identification. The effect of this smoothing can be seen by comparing the dashed line in with the amplitude of the blue bandpass-filtered pressure signal in Fig. 6.7. Condition definitions are based on peak, trough and zero gradient positions, with minimum thresholds applied to ensure only significant characteristics of the gradient are considered for condition identification. The markers in Fig. 6.7 show examples of the identification of each condition from the envelope amplitude. In some cases, manual refinement of the identified positions is required, such as for the failure to identify the significant decrease of growth at $t \sim 1.51\,\mathrm{s}$; however, this rarely leads to significant differences in the overall result. The regions surrounding identified positions are allocated to a single intermittency condition. The size of these regions are defined by either a minimum threshold or by the characteristics of the surrounding envelope amplitude. As the position of each CL image with respect to the pressure time series is known

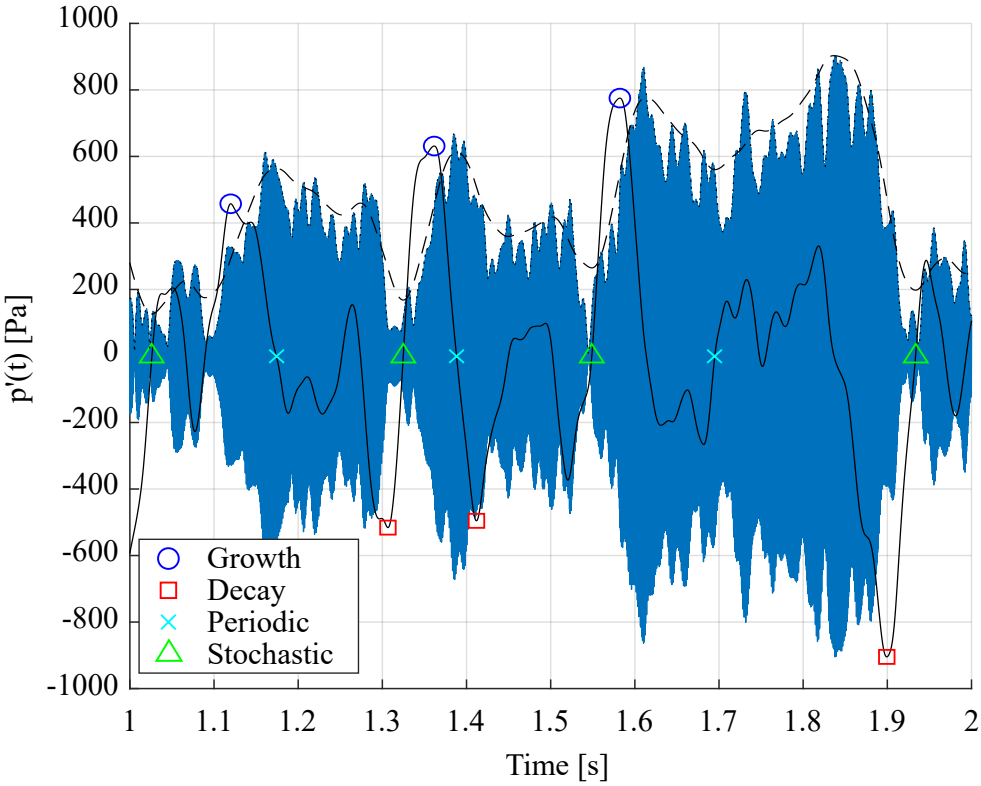

Figure 6.7: Example of the intermittency condition identification for the condition locking procedure. The dashed line indicates the smoothed envelope amplitude while the solid line represents its gradient. Markers show the indentified centres for different condition regions.

due to the synchronous measurement of pressure and image data, each frame can be categorised within one of if the intermittency conditions. This allows the calculation of corresponding ensemble-averaged images in a similar manner to the phase-locking process described in Section 4.2.

6.2.3 Flame Dynamics Associated with Intermittency Conditions

The ensemble-averaged CL images for each of the four intermittency conditions are shown in the left column of Fig. 6.8. The right column

shows the difference between each of the condition-locked mean images and the overall mean image calculated as

$$\Delta \bar{I}_{cond} = \bar{I}_{cond} - \bar{I} \tag{6.3}$$

where $\bar{I}_{cond}$ represents each of the condition-averaged images. The black contour indicates the approximate flame boundary estimated from the overall mean image to highlight how the heat release distribution varies between the conditions. The contour position is based on the mean CL intensity level within which the majority of the heat release occurs. From inspection of the flame response over the intermittency cycle, the following trends are observed:

- During periods dominated by stochastic pressure fluctuations, a greater proportion of the heat release is concentrated in the autoignition-stabilised core region.
- During the growth phase as the coherent pulsation amplitudes increase, there is a shift of the heat release distribution towards the propagation-stabilised shear layer regions.
- During the peak periodic pressure oscillation amplitudes, the heat release concentrated in the shear layer regions is also at its maximum.
- The decreasing pulsation amplitudes during the decay phase coincide with greatly reduced heat release in the shear layers, and a shift of the maximum local heat release back towards the autoignition-stabilised core region.

The difference images in the right column of Fig. 6.8 indicate that the shift in the CL intensity between conditions is of the order of 5% of the maximum overall intensity from the mean image. This therefore represents a significant redistribution of the flame heat release between the different intermittency conditions. It is likely that this shift of maximum

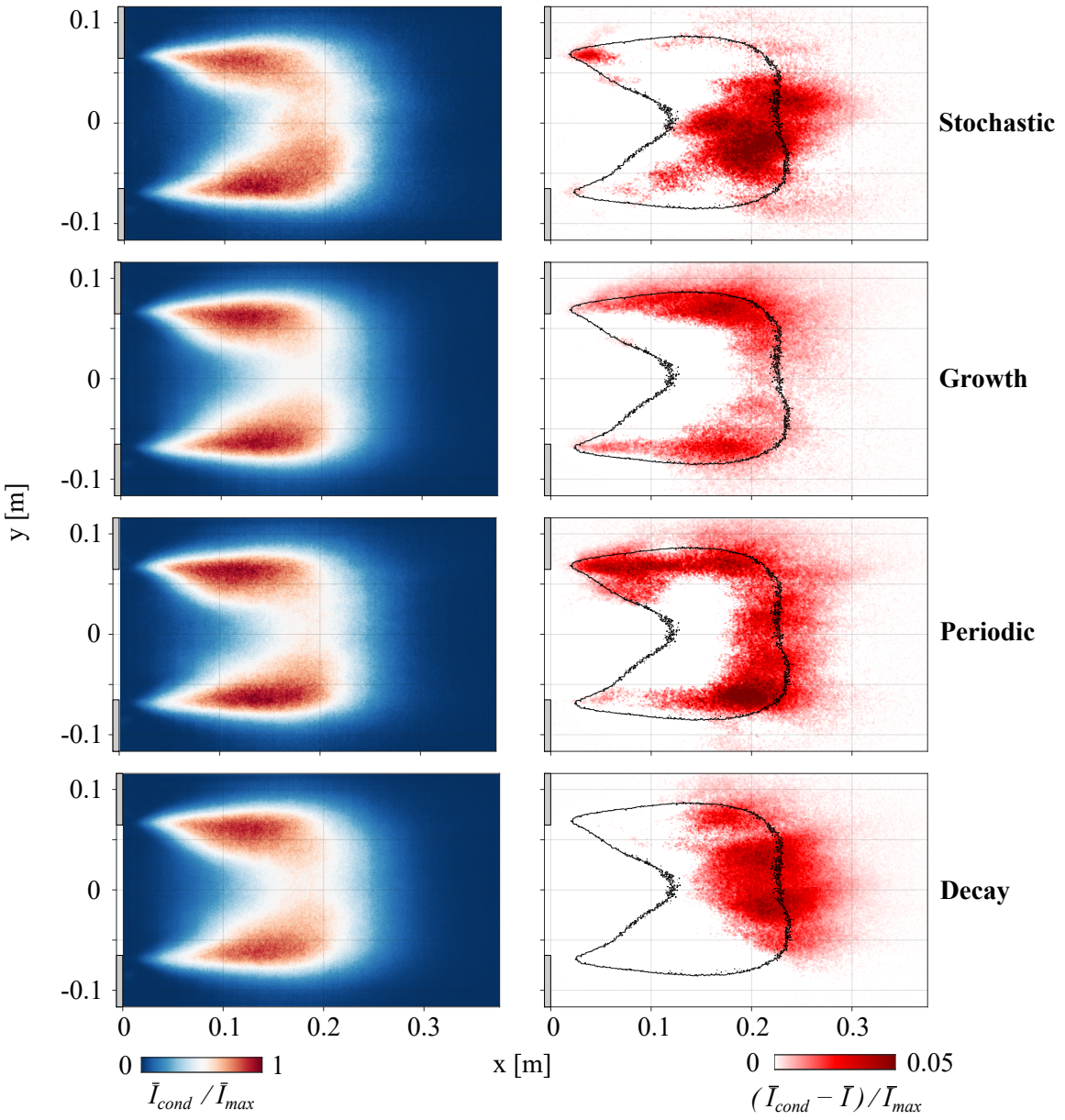

Figure 6.8: Condition-locked, ensemble-averaged CL images during each intermittency condition. Left: mean images for each condition. Right: difference in CL intensity between the top images and the overall mean image. The black contour represents the approximate flame boundary of the overall mean image for reference.

heat release is mainly a result of the stochastic nature of autoignition kernel formation. Although the majority of the heat release is concentrated close to the combustor centreline, it is shown in Refs. [110,114,142] that there is also autoignition activity in the shear layer regions. Therefore, the periods of elevated heat release close to the shear layers could be caused by increased kernel formation in the upper/lower parts of the flame, followed by greater core heat release as more kernels begins to form closer to the combutsor centreline. This connection to the stochastic nature of autoignition kernel formation explains the persistency of the intermittency across the operating range, rather than only existing at a transition point between stable and unstable operation.

By comparing the heat release redistribution shown in Fig. 6.8 with the acoustic pressure field associated with the T1y mode (see Fig. 5.4), the link between the observed flame response and the different intermittency conditions can be described. As the driving of high-frequency thermoacoustic oscillations is associated with local interactions of the flame and the acoustic field, flame-acoustic interactions in regions where pulsation amplitudes are high represent significantly greater driving potential than in regions where pulsation amplitudes are low. As described in Section 5.2.1, the T1y mode shape has a pressure node along the horizontal centreline of the reheat combutstor and antinodes at the upper and lower walls. Therefore, the strongest thermoacoustic driving potential exists during the growth and periodic intermittency conditions where the heat release is increased in regions of high pressure oscillation amplitudes near the antinodes. On the other hand, the shift of the heat release towards the pressure node during the decay and stochastic conditions decreases the driving potential. It is therefore inferred that the observed intermittent behaviour is the result of shifting heat release distribution between areas of varying thermoacoustic driving potential. This produces the periods of pulsation amplitude growth, during which the increase in thermoacoustic driving overcomes acoustic dissipation, and then decay once driving decreases and acoustic dissipation once again dominates.

Next, the impact of the intermittent behaviour on the modulation of the shear layers by acoustically-induced vortex shedding is investigated by comparison of the oscillating CL intensity field during each intermittency condition. Both the phase- and condition-locking procedures are applied in this case to calculate the ensemble-averaged images. The oscillating CL intensity for a single phase interval is shown in Fig. 6.9 for the four intermittency conditions. To better show how the itermittency alters the oscillatory heat release pattern seen previously in the right column of Fig. 6.1, the difference images are calculated relative to each condition-resolved mean image (see left column of Fig. 6.8), such that:

$$\Delta \bar{I}_{\phi,cond} = \bar{I}_{\phi,cond} - \bar{I}_{cond} \tag{6.4}$$

where $\bar{I}_{\phi,cond}$ is the phase- and condition-resolved mean image. From examination of the four conditions illustrated in Fig. 6.9, the following observations can be made:

1. During stochastic conditions, the oscillating pattern appears to have completely broken down. There is no coherent flame behaviour at the frequency of the T1y mode and the intensity field is dominated by random fluctuations.
2. With growing pressure pulsation amplitudes, the oscillatory pattern begins to show in the upstream parts of the shear layers.
3. Periodic pressure oscillation conditions produce a clear oscillatory heat release pattern.
4. During decay of pulsation amplitudes, the pattern begins to weaken. The intensity pattern is only seen in the upstream part of the shear layers while the downstream region is increasingly dominated by random fluctuations.

The differences in the oscillatory pattern between each intermittency condition is a result of the difference in strength of acoustic oscilla-

tions of the transverse acoustic field. The low amplitude stochastic pressure fluctuations are not associated with the periodically oscillating transverse acoustic field required for the formation of the acoustically-induced vortices which modulate the heat release in the shear layers. As a result, the pattern seen previously in Fig. 6.1 is not present during the stochastic condition. As the periodic pressure oscillation develop and their amplitude grows, thermoacoustic driving increases and the pattern of alternating hot and cold patches begins to form. As pulsation amplitudes increase, the pattern becomes more pronounced and persists further downstream throughout the growth condition. The pattern is clearest and heat release oscillations are strongest during the periodic condition where pressure oscillation amplitudes are at their maximum. Finally, once the heat release distribution shifts back towards the core flame region, driving potential is reduced and the pressure oscillation

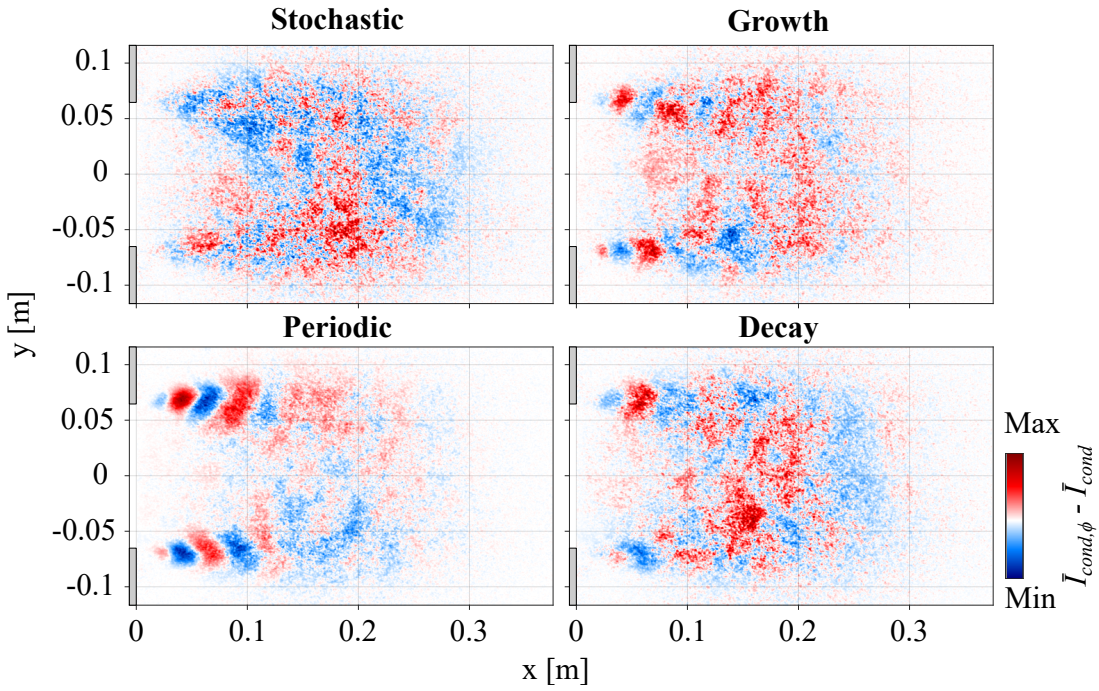

Figure 6.9: Phase- and condition-resolved ensemble-averaged difference images for a sample phase interval corresponding to each intermittency condition.

amplitudes decrease during the decay condition. The is reflected in the weakening of the heat release pattern under this condition before returning to the stochastic condition.

The strengthening of the heat release pattern during conditions associated with increased thermoacoustic driving (growth/periodic conditions), and the subsequent weakening when the driving potential is reduced (decay/stochastic conditions), reinforces the hypothesis that modulation of the reactive shear layers is the main driving mechanism of the T1y mode. As was the case with the phase-resolved imaging in Section 6.1, no behaviour associated with flame displacement and deformation by the acoustic velocity field or modulation of the autoignition core flame are observed in Fig. 6.9. It is therefore assumed that the contribution of these additional mechanisms is small and the driving of this mode is dominated by the reactive shear layer modulation mechanism.

6.3 Summary

In this chapter, the reactive shear layer modulation by acoustically-induced vortex shedding is investigated by examining the dynamic flame response at the T1y mode frequency. This is carried out in two steps. Firstly, the coherent response of the unsteady heat release over the acoustic oscillation cycle, indicated by phase-resolved CL imaging, reveals the following:

- An alternating, antisymmetric pattern of hot and cold patches are observed which originate at the edges of the area jump at the combustor chamber inlet and are convetively transported through the shear layers. These patches are shed at the T1y mode frequency and cause a visible wrinkling of the upper and lower flame regions. This heat release modulation is consistent with similar behaviour seen in swirl and jet flames and is the result of vortices induced by the acoustic velocity field.

- Despite the convective nature of this phenomenon and the fact that several patches of opposing sign exist simultaneously, the net heat release oscillation in the upper and lower halves of the combustion chamber oscillate in-phase with the T1y acoustic pressure field.
- Comparing the contribution from the heat release patches with the total heat release fluctuations in the combustion chamber reveals that the reactive shear layer modulation mechanism makes up the vast majority of the overall heat release oscillation. This indicates that this mechanism is the dominant source of driving of this mode.
- No observable effects are present which indicate any significant contribution of the flame displacement and deformation mechanisms or of modulation of the autoignition portion of the flame.

The second step was to determine the reason for the intermittent nature of the T1y mode thermoacoustic instability. Distinct conditions corresponding to different phases of the intermittency cycle are defined and the flame response under each condition is investigated, leading to the following findings:

- The condition-dependent flame dynamics reveal a shift in the heat release distribution between the autoignition-stabilised core flame region and the propagation-stabilised reactive shear layers. Intermittent bursts of coherent pressure pulsations coincide with increased heat release in the shear layers while the stochastically dominated fluctuations occur when heat release is more concentrated in the core.
- This redistribution of heat release is expected to be due to the stochastic nature of autoignition kernel formation, which explains the random bursts of unstable behaviour amidst stable conditions.
- Simultaneous condition- and phase-averaging of the CL images reveals that the strength of the pattern of alternating heat release patches is closely associated with the acoustic pulsation amplitude.

The pattern is not visible when amplitudes are low and is clearest when pulsation amplitudes are high. This further reinforces the connection between the shear layer modulation mechanism and the T1y mode thermoacoustic instability.

7 Autoignition Delay Modulation by High-Frequency Acoustic Pulsations

This chapter focusses on flame driving associated with modulation of the autoignition delay time by transverse acoustic pulsations. The investigation of the autoignition delay modulation mechanism will focus on the response of the 3000 Hz T1z mode due to the overlap of the autoignition core region with regions of high-amplitude acoustic oscillations (see Section 5.3. The 1600 Hz T1y mode is not considered here as there are no significant pressure oscillations in the vicinity of the autoignition-stabilised portion of the flame. In Section 7.1, the dynamic flame response at the T1z mode frequency is presented and discussed which provides information on the sources of driving for this mode. Phase-resolved CL from multiple perspectives is considered for this mode due to the LOS integrated nature of the images. Once the potential driving mechanisms are identified, Section 7.2 investigates the contribution of the autoignition delay modulation mechanism in isolation by developing a reduced order model coupled to reaction kinetics calculations which is then compared with the experimental results of Section 7.1.

7.1 Flame Dynamics Associated with High-Amplitude Limit-Cycle Oscillations

The following section concerns the flame response associated with high-amplitude limit-cycle oscillations in the reheat combustor at the T1z mode frequency. As described in Chapter 3, flame dynamics can be investigated by means of CH* CL imaging from all lateral sides of the re-

heat combustion chamber. However, due to the orientation of the unstable transverse eigenmode in the z-direction, the line-of-sight integration of the CL imaging means that no significant effects relevant for driving of the limit-cycle oscillations are observed from the side-view. As such, results from this view are omitted from the following discussions which will instead focus on the observations from the top (xz-plane) and rear (yz-plane) view perspectives. Using the same process used in Section 6.1, phase locking of the instantaneous image frames with the simultaneously sampled dynamic pressure allows evaluation of the flame dynamics during specific portions of the transverse pressure oscillation cycle. Twelve phase intervals are defined with corresponding ensemble-averaged images, each of which is an average of approximately 2,900 frames for the top-view and 1,350 frames for the rear-view.

The left column of Fig. 7.1 shows four CH* CL ensemble-average images from the top-view camera position. It can be seen that there is an antisymmetric axial motion of the flame close to the chamber walls, illustrated by comparison of the flame tip contours for each phase interval with the overall mean flame tip position, while the flame close to the combustor centreline remains unperturbed in the axial direction. This flame tip motion is associated with a local increase in heat release (indicated by greater CL intensity) upstream of the mean flame position close to the positive pressure antinode and decreased heat release on the opposite side where the pressure antinode is negative. This can be more clearly seen in Fig. 7.2 which shows the CL intensity contours representing the approximate flame boundary overlaid on the numerically estimated acoustic pressure field for the first phase interval depicted in Fig. 7.1, as well as for the overall mean image. The estimated acoustic field is obtained using the method described in Section 4.3. The observed flame shape modulation occurs in phase with the oscillating acoustic pressure. This increase in upstream heat release during peak pressure amplitudes strengthens flame-acoustic feedback due to attenuation of acoustic pressure oscillations in the downstream direction. Consequentially, the in-phase oscillatory flame tip motion represents a significant source of thermoacoustic driving. It is therefore es-

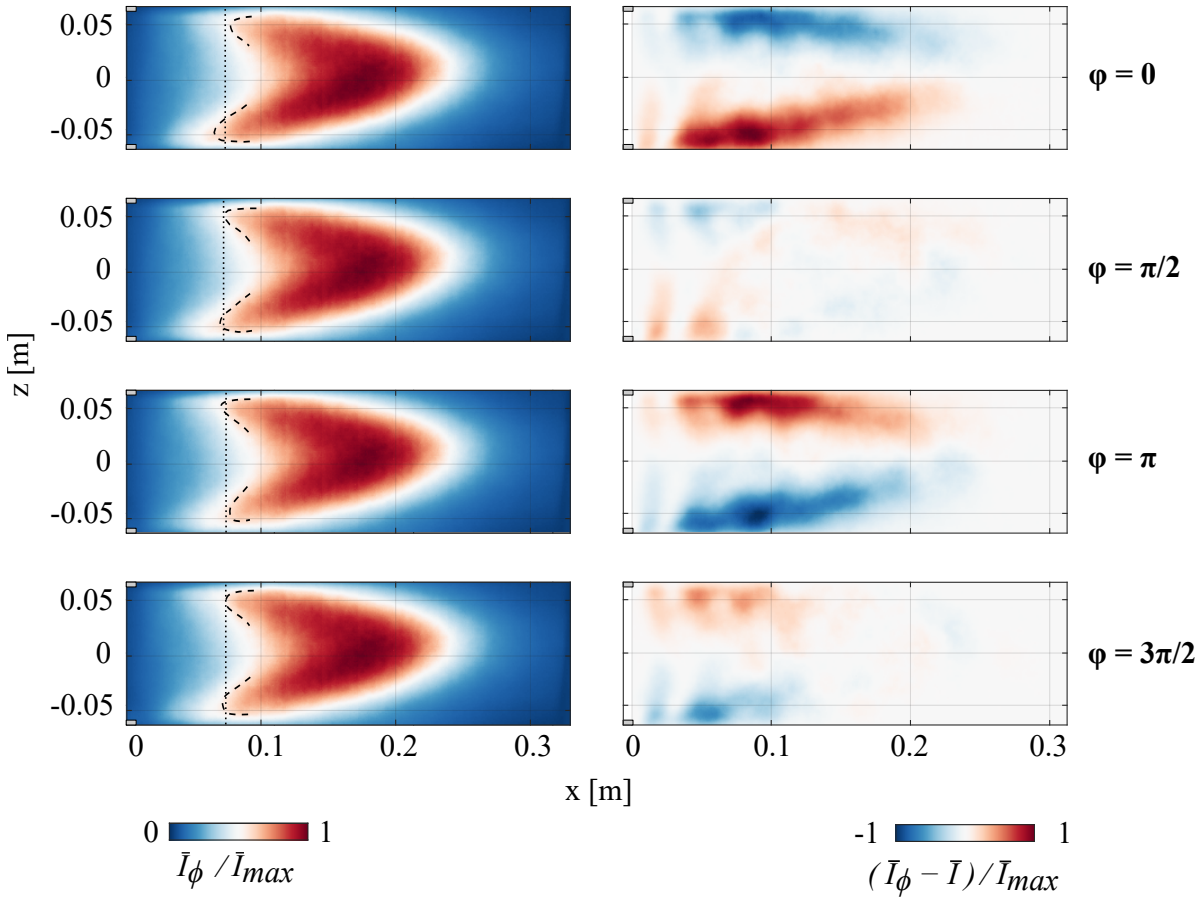

Figure 7.1: Phase-locked ensemble-averaged CL images of the flame from the rear view at the T1z mode frequency for sample phase intervals (left) and the corresponding difference images (right). In the left column, dotted vertical line indicates overall mean flame tip position and dashed contours are approximate flame tip boundaries.

sential to determine the cause of this axial flame motion. One possibility is that the oscillating acoustic field is causing an in-phase modulation of the auto-ignition delay time which would result in decreased auto-ignition delay times while the pressure oscillation is of positive sign and vice versa. This could produce the observed flame modulation, as a decrease/increase in auto-ignition delay time would produce a cor-

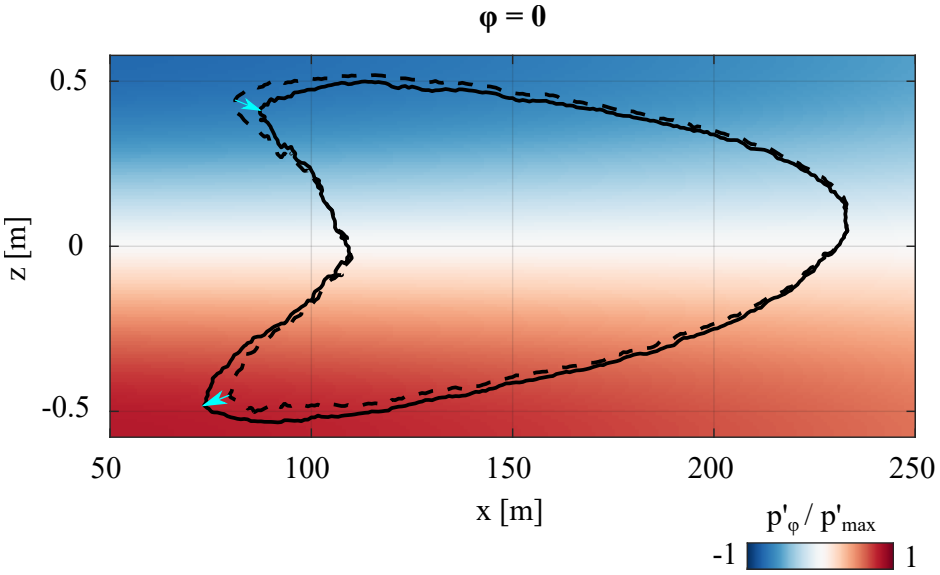

Figure 7.2: Flame contours highlighting axial tip movement with overlaid acoustic pressure field. Solid contour is the displaced flame at phase interval $\phi = 0$ while the dashed contour is the mean flame shape.

responding upstream/downstream movement of the ignition position. This is also supported by the observation that the flame movement is strongest where pressure oscillations are highest while no significant axial flame movement is present close to the pressure node at the combustor centreline. A further possibility is that transverse flame displacement is produced as a result of the acoustic velocity field, as described and observed for swirl-stabilised flames in Refs. [90, 91]. In this case, flame displacement would induce a deformation towards the chamber side walls, resulting in regions of compression and expansion which would have implications for reactivity and could also produce a similar flame movement. In this case it is expected that a transverse flame motion would occur, displacing the flame towards the region of maximum pressure. Close inspection of Figs. 7.1 and 7.2 reveals a very small modulation of the transverse position of the flame, although it is difficult to observe clearly from this perspective.

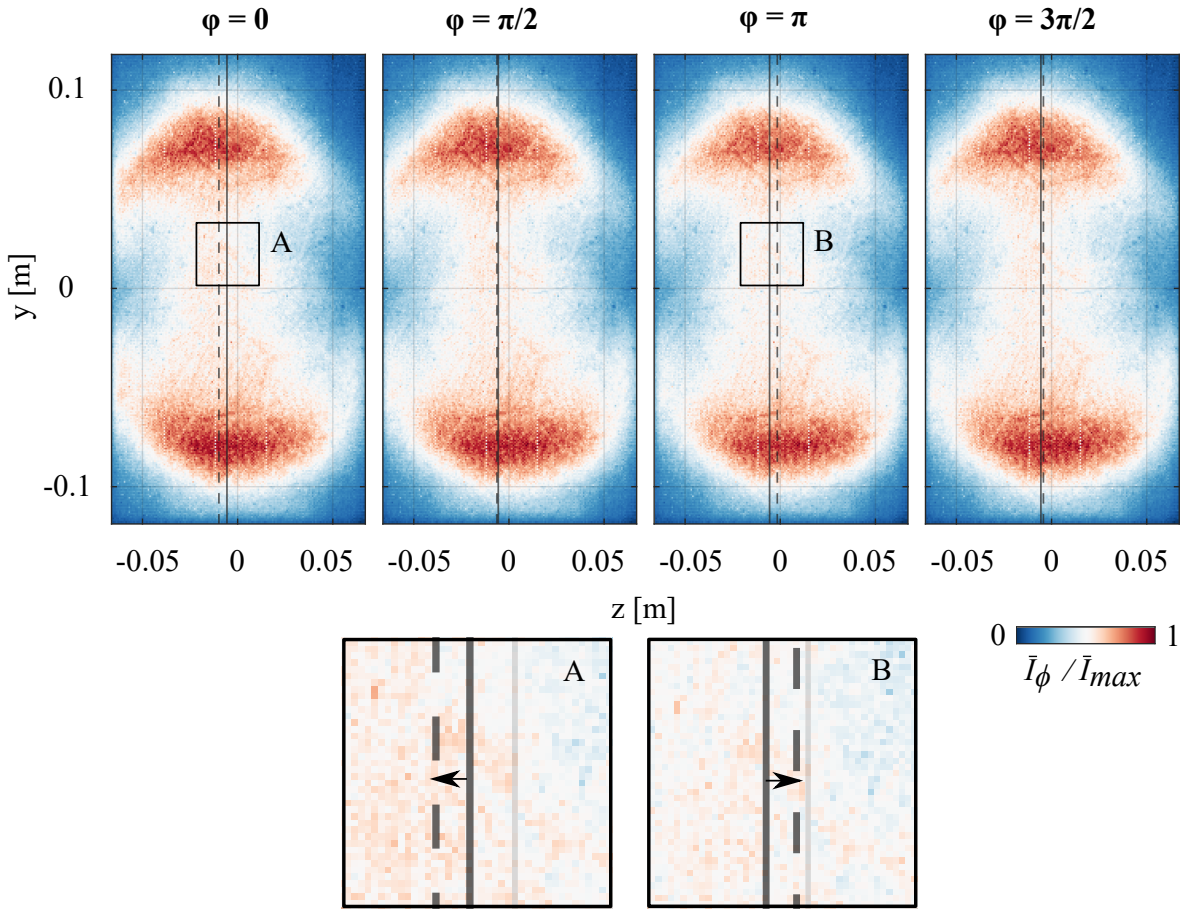

Figure 7.3: Phase-locked ensemble-averaged CL images of the flame from the rear-view for sample phase intervals. The solid vertical line indicates the median location of heat release for the overall mean image while the dotted lines indicate the median heat release location for the corresponding ensemble-averaged image. Detail views A and B show the direction of the flame displacement during the first and third phase intervals.

To further investigate if a transverse flame displacement is present, CH* CL intensity distribution images from the rear-view are shown in Fig. 7.3. These correspond to the same phase intervals as in Fig. 7.1. The solid vertical line in each image is positioned at the median position of maximum intensity across the height of the combustion chamber

for every frame, while the dashed lines indicate the maximum intensity position for each ensemble-averaged image. The shift of this maximum intensity position indicates that there is indeed an in-phase transverse flame displacement towards the region of maximum acoustic pressure. The magnitude of the displacement is small compared with the axial motion observed from the top-view. The observation of both the axial motion and transverse displacement indicates that it is likely that the overall flame shape modulation is a result of the superposition of both auto-ignition delay time and flame displacement/deformation effects. Furthermore, as both effects represent an oscillation of heat release about its mean value in phase with the acoustic mode, each may contribute to the thermoacoustic driving potential.

In order to provide further information with regards to the oscillating heat release field, the spatially distributed CL intensity oscillation, as seen from the top-view, is shown in the right column of Fig. 7.1, which depicts the difference between each of the ensemble-averaged images presented in the left column of Fig. 7.1 and the overall mean image, i.e. $\Delta\bar{I}_\phi = \bar{I}_\phi - \bar{I}$ (similarly to the approach used previously in Section 6.1). The value of the CL intensity is normalised by the maximum intensity value of the overall mean image to allow for easier comparison of the flame response during each phase interval. A clear oscillatory pattern in phase with the acoustic pressure can be seen. As would be expected, the greatest intensity oscillation occurs in the area of the previously observed axial flame tip motion. It is also observed that the oscillations are not limited to these regions and that there is significant oscillation intensity along the length of the flame.

Similarly to the flame shape modulation, the intensity oscillations are most pronounced close to the pressure anti-nodes at the chamber walls, with no significant oscillation near the pressure node at the centreline. The intensity oscillation away from the walls does increase slightly in the downstream direction; however, this is due to the narrowing of the flame (as seen from the top-view mean flame image shown in Fig. 3.5.

The distribution of this oscillatory heat release pattern across the com-

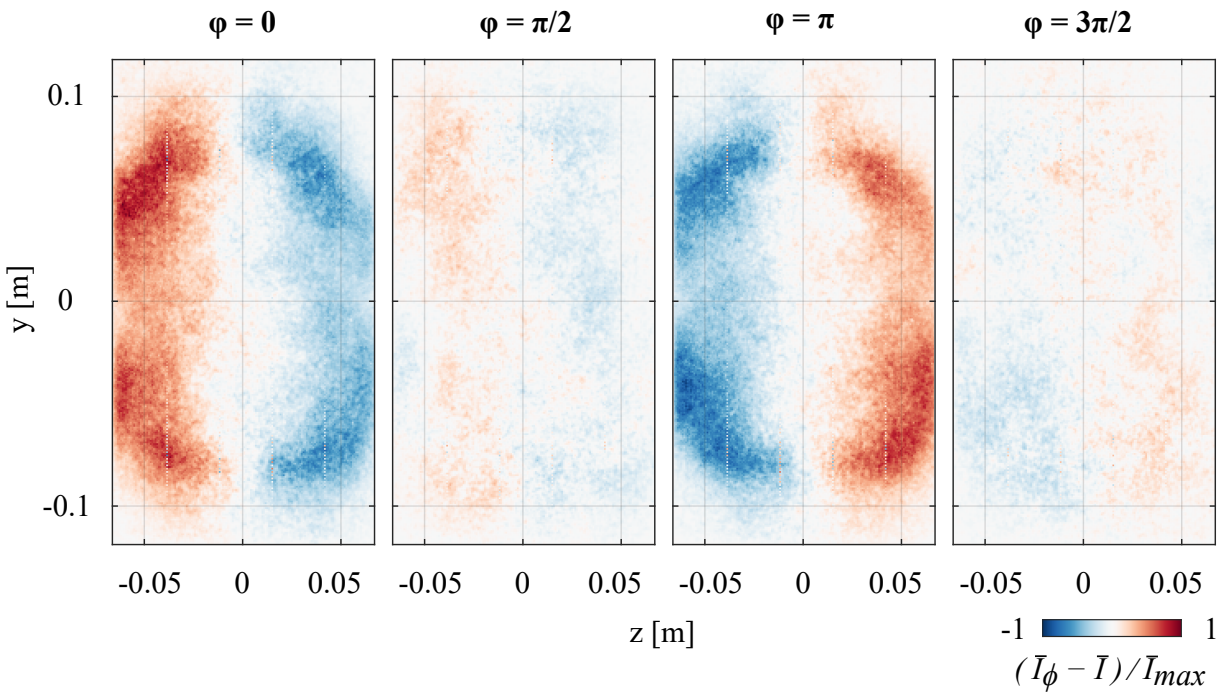

Figure 7.4: Phase-locked ensemble-averaged CL difference images of the flame from the rear-view corresponding to the phase intervals shown in Fig. 7.3.

bustor y-direction, and therefore for each of the distinct flame stabilisation zones, can be seen from the rear-view ensemble-average difference images shown in Fig. 7.4. The same alternating heat release pattern is observed; however, from this view it can be determined that the intensity oscillations take place across both the propagation stabilised shear layers and the auto-ignition stabilised core region. The highest intensity oscillation occurs in areas which contain vortical flow structures originating from the vortex generators in the mixing section. Greater mixture homogeneity in these regions due to the increased mixing may be the reason for the maximum of local oscillation intensity here. This maximum also coincides with the positions of the propagation stabilised shear layers, although it should be noted that the downstream portions of the propagation stabilised areas have been shown to also contain auto-ignition [114]. The higher oscillation intensity observed in these

regions could, therefore, be a superposition of modulation of the heat release of both the reactive shear layers and auto-ignition; however, the low pressure-sensitivity of the propagation stabilised flame region implies that the auto-ignition modulation likely dominates the oscillatory flame response. Despite the maximum oscillation intensity being located close to the shear layer regions, the heat release oscillations in the purely auto-ignition stabilised core flame are still of significant amplitude. Due to this distribution of high-amplitude heat release oscillations across almost the entire height of the combustion chamber, as well as their significant axial extent, the in-phase flame-acoustic interactions therefore represent high driving potential of thermoacoustic instabilities.

It is expected that the observed heat release oscillation pattern is a result of the superposition of multiple effects. Firstly, the auto-ignition contribution can be explained as a modulation of reactivity in the regions of high pressure oscillations which would result in an increase or decrease in auto-ignition activity during periods of positive or negative pressure oscillation amplitude respectively. Secondly, the aforementioned expansion and contraction of flame regions near the wall induced by flame displacement and associated deformation could also produce a similar oscillating heat release pattern to that observed. Flame-acoustic interactions due to modulation of the reactive shear layers by acoustically-induced vortex shedding does not appear to be present in the case of the T1z mode. This is due to the small extent of the area expansion in the z-direction which does not produce any significant recirculation region. The low transverse acoustic velocity close to the velocity nodes at the walls (see Fig. 5.8) also precludes the formation of strong vortex shedding behaviour. Furthermore, as described in Section 5.3, equivalence ratio modulation from the mixing section is also not present due to the strong attenuation of the T1z mode in the upstream direction. As the T1z mode experiences extremely high limit-cycle amplitudes of roughly 10 kPa it is essential to determine the mechanism which dominates the driving.

7.2 Modelling of Autoignition Delay Modulation

In this section, a flame-acoustic coupling mechanism based on local modulation of the autoignition delay time by thermoacoustic oscillations is proposed. A reduced order model coupled to reaction kinetics calculations for the autoignition flame response to transverse acoustic perturbations is developed based on a simplified representation of the test rig geometry introduced in Chapter 3.

7.2.1 High-Frequency Autoignition Delay Modulation Mechanism

First, the underlying mechanism which couples the autoignition portion of the flame with the oscillating acoustic field is introduced. In recent years, a number of studies have investigated the autoignition flame response; however, these have focussed on the low-frequency regime where the flame modulation was mainly due to convectively transported flow disturbances [113–117,125,129,130,137,138,153]. In the high-frequency regime, convective effects such as these are strongly attenuated [109] and thermoacoustic feedback is instead dominated by local interactions between the acoustic field and the unsteady heat release of the flame [108].

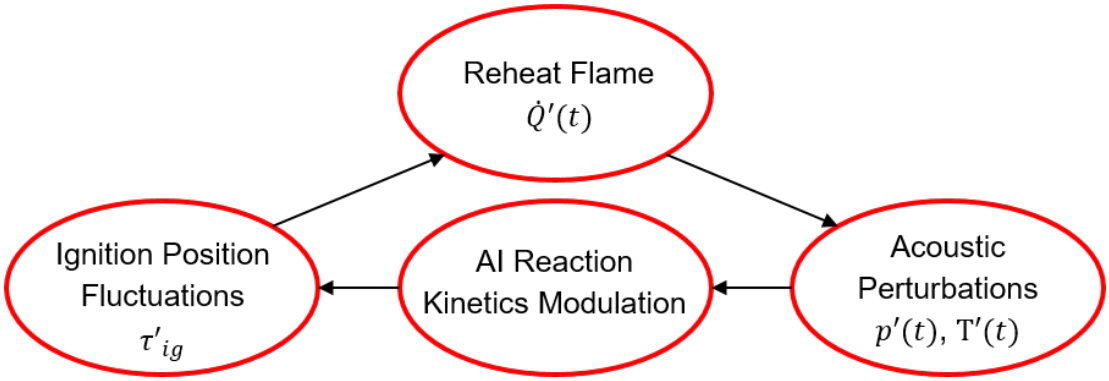

Figure 7.5: Flame-acoustic interaction mechanism for high-frequency autoignition delay modulation.

In this case, the potential for high-frequency transverse thermoacoustic oscillations to locally influence the autoignition delay time in reheat flames is investigated on the basis of the following feedback mechanism, which is illustrated in Fig. 7.5:

- Localised acoustic perturbations in terms of pressure (and induced isentropic temperature) oscillations arise in the combustion chamber in regions where autoignition is present.
- Due to the high sensitivity of autoignition flames to pressure and temperature disturbances, these acoustic perturbations directly modulate the local reaction kinetics.
- This produces a fluctuation in the autoignition delay time, and therefore a shift in the ignition position such that there is an axial movement of the flame.
- The motion of the flame in turn results in a fluctuation of the heat release rate, which produces further acoustic perturbations.
- If the oscillations of pressure and heat release rate occur in-phase with each other, this results in a positive feedback loop and allows the instability to grow in strength.

This mechanism differs from existing low-frequency models in that the local reaction kinetics are being modulated directly by the oscillating acoustic field, rather than being modulated by a perturbation of upstream flow conditions induced by the acoustic field. In existing low-frequency models, the acoustic perturbations travel upstream and cause a disturbance in the incoming flow parameters, for example by causing fluctuations in temperature or equivalence ratio, which then produce a fluctuation in the autoignition delay time as they are convected to the flame front (see Section 2.3.1 for examples of these mechanisms). For the mechanism presented in Fig. 7.5, the autoignition delay modulation is not due to convected flow properties, but is instead a result of a direct interaction between the transverse acoustic oscillations and the

chemical kinetics which determine the autoignition delay time. The local modulation of the autoignition delay time causes the flame position to oscillate in the axial direction. As this motion represents a fluctuation of the relative velocity between flame and fluid, the instantaneous amount of fuel being burned varies over the acoustic period, resulting in the heat release rate oscillation. A similar phenomenon was observed from numerical investigations by Gant et al. [153]; however, this was instead induced by entropy waves from the first stage flame. In the following section, a reduced order model is developed to investigate if the proposed high-frequency autoignition delay modulation mechanism does indeed produce a coherent flame response.

7.2.2 Flame Response Model Setup

The reduced order model developed to investigate the autoignition delay modulation mechanism consists of a simplified representation of the test rig described in Chapter 3. The model has been developed using the Python interface of Cantera [154] with the GRI-Mech 3.0 natural gas reaction mechanism [155]. To improve the comparability with experimental results, both the vitiator and reheat stage are modelled as illustrated in Fig. 7.6. This allows the conditions from different experimental operating points to be investigated numerically without requiring separate calculation of the reheat combustor inlet conditions. The input parameters for the model also mirror the control parameters of the test rig to further simplify comparison of various operating points.

The first stage is modelled as two perfectly stirred reactors (PSR): one representing the combustion of electrically preheated air and natural gas (Vitiator Combustion PSR) and one representing the addition of dilution air (Vitiator Dilution Air PSR). After the dilution air PSR, the vitiated air temperature is decreased slightly to account for heat losses between the two stages.

The second stage is modelled as two reactor steps. The addition of the

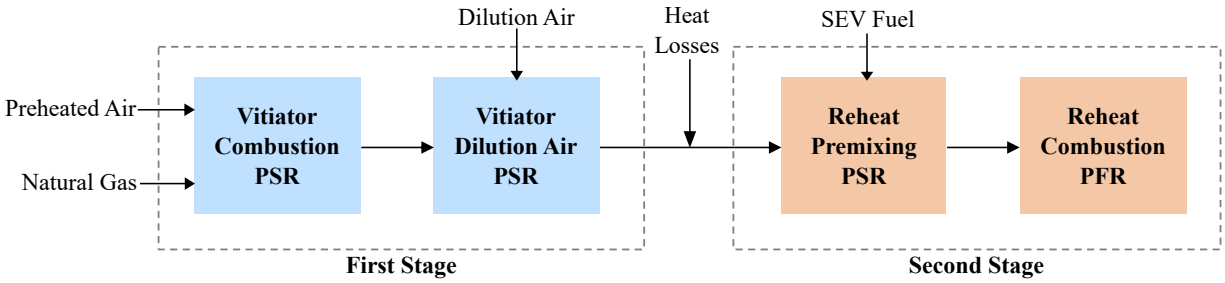

Figure 7.6: Schematic of the reduced order model showing the approaches used to represent each main component of the test rig.

secondary fuel in the reheat combustor mixing section is modelled by another PSR but without any reactions taking place (Reheat Premixing PSR). This approach to modelling the fuel-air mixing is necessary for the inlet conditions of the subsequent step but assumes that the mixing occurs instantaneously and results in perfect premixing at the injection location. This assumption neglects the impact of dispersion due to inhomogeneous mixing. In future work, this may be accounted for by including a dispersive factor which assumes a normal distribution of the autoignition delay time [156]. The reheat combustion process (Reheat Combustion PFR) is modelled as a series of plug flow reactors (PFR) in a straight duct as illustrated in Fig. 7.7. Each mixture plug can be described as an independently evolving Lagrangian fluid particle which enters the domain at the fuel injection position ($x = 0$) and is advected downstream by the mean flow. Chemical reactions progress as the plug is advected due to the high inlet temperature from the vitiator. The time between injection and ignition is the autoignition delay time, τ_{ig}. By considering the evolution of the fluid particle velocity, $u(t)$, the time from injection, t, can be used to find the position of the mixture plug, x_{plug}, in the domain:

$$x_{plug}(t) = \int_0^t u(t)\, dt \tag{7.1}$$

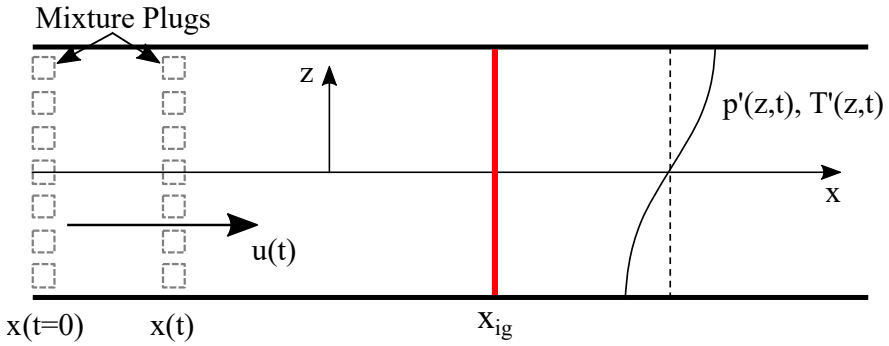

Figure 7.7: Sketch of the plug flow reactor setup used to model the autoignition flame response in the second stage.

As the flame response to transverse thermoacoustic modes is of interest, the domain is discretised in the transverse direction following the approach used by Zellhuber et al. [111], such that seven streamlines at equidistant transverse locations are represented by separate mixture plugs. An oscillatory pressure fluctuation, p', is imposed on the mixture plugs with an amplitude which depends on their transverse location, z, to account for the acoustic pressure distribution of the high-frequency mode and on time, t, such that:

$$p_{plug}(z,t) = p_0 + p'(z,t) \tag{7.2}$$

$$p'(z,t) = A(z)e^{i\omega t} \tag{7.3}$$

where p_{plug} is the pressure of the fluid particle, p_0 is ambient pressure, A is the oscillation amplitude at a given transverse location and ω is angular frequency. As only the evolution of the plug from injection until ignition is of interest, during which time the pressure drop due to gas expansion is very small [117], p_0 is kept constant and the pressure is only varied by the imposed oscillations. The pressure condition at injection is varied depending on the injection time of the mixture plug, t_i:

$$p'_{inj}(z, t_i) = A(z)e^{i\omega t_i} \tag{7.4}$$

For clarity, t represents the time used to track the Lagrangian fluid particle through the domain, while t_i represents the times at which successive fluid particles are injected into the domain.

Isentropic temperature fluctuations are then superimposed on top of the pressure oscillations. The amplitude of these temperature fluctuations for a given time is calculated via the linearised isentropic relation:

$$T'(z, t) = T_r(t)\frac{p'_{max}}{p_0}\frac{(\gamma - 1)}{\gamma}e^{i\omega t} \tag{7.5}$$

where T_r is the temperature evolution of the plug due to the chemical reactions. Unlike with pressure, the temperature rise due to chemical reactions prior to ignition is not negligible and must be considered. The temperature of a mixture plug for a specified time is therefore given by:

$$T_{plug}(t) = T_r(t) + T'(z, t) \tag{7.6}$$

To account for the area jump between the mixing section and the reheat combustion chamber, the approach used by Zellhuber et al. [111] is again considered. The impact of jet expansion is neglected due to the small step height in the z-direction (see Fig. 3.4) and the influence of the area jump is therefore assumed to be purely acoustic in nature. The smaller cross section in the mixing section compared with that in the combustion chamber results in a difference in cut-on frequency, which means that transverse modes in the combustion chamber are strongly attenuated in the mixing section as shown previously in Fig. 5.6. As a result, transverse pressure oscillations (and therefore isentropic temperature fluctuations) at the frequencies of interest will be small in the region upstream of the area expansion. This is implemented in the model as:

$$p'(x,z,t) = \begin{cases} 0 & x < x_j \\ Ae^{i\omega t} & x \geq x_j \end{cases} \tag{7.7}$$

where x_j is the axial location of the area jump. As the isentropic temperature is calculated based on the pressure oscillation amplitude, this condition produces the same impact on the induced temperature fluctuations.

7.2.3 Identification of Ignition Location

As shown in Fig. 7.2, the axial flame motion is mostly concentrated close to the walls. Therefore, the results presented correspond to the outermost mixture plug shown in Fig. 7.7 where the oscillation of $p'(z,t)$ is greatest. Scaling the acoustic field in Fig. 5.8 with the experimentally measured pressure amplitudes indicates that pressure oscillations in this region correspond to approximately 10 kPa, which is set as the value for A in Eq. (7.3). According to Eq. (7.5), this results in a corresponding isentropic temperature fluctuation of ~ 25 K in the region shortly after the area jump.

Figure 7.8 shows the axial temperature profile in the reheat combustor with the transverse acoustic oscillations imposed for a sample injection time, t_i. The impact of the isentropic temperature fluctuations can be clearly seen from the T_{plug} profile downstream of the area jump. The increase in the amplitude of the temperature fluctuations following the sharp temperature rise can be attributed to the increase of the T_r term in Eq. (7.5).

The ignition position, x_{ig} is defined as the position where the gradient of the temperature profile is at its maximum [117]. To avoid errors due to the modulation of the temperature profile gradient by the isentropic fluctuations, the temperature due to chemical reaction, T_r (see Eq. (7.6)), is used to determine the ignition position. Therefore, x_{ig} is the position where $dT_r(t) \,/\, dx$ is at its maximum, as marked in Fig. 7.8.

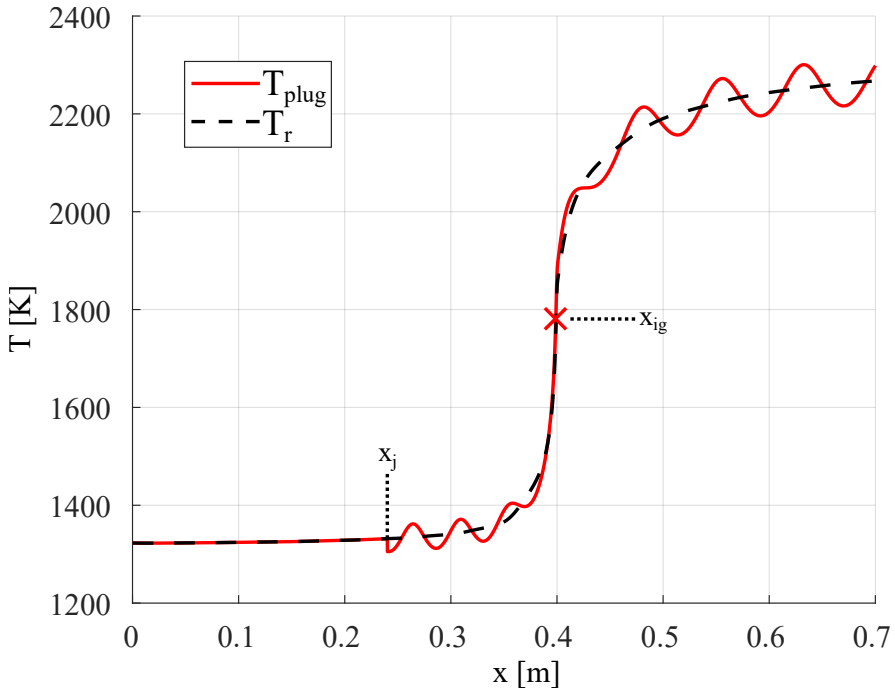

Figure 7.8: Axial temperature profile of the outermost mixture plug calculated by the PFR model with the imposed acoustic oscillations for a sample injection time, t_i. The area jump and ignition positions are indicated by x_j and x_{ig}, respectively. Both the instantaneous temperature in the mixture plug, T_{plug}, and the temperature due to the chemical reactions, T_r, are shown.

7.2.4 Autoignition Flame Response to Transverse Acoustic Oscillations

Figure 7.9 shows the variation of the ignition length over a full oscillation cycle from the experiments and the flame response model. The error bars shown at each experimental data point indicate the uncertainty of measuring the ignition position, x_{ig}, based on the pixel resolution of the optical setup ($1.5\,\mathrm{px/mm^2}$). To account for the error margin of the control hardware of the test rig in the model (most notably in terms of air and fuel mass flow rates), the model results were calculated for the ideal case (solid black line) as well as for the the upper and lower limits

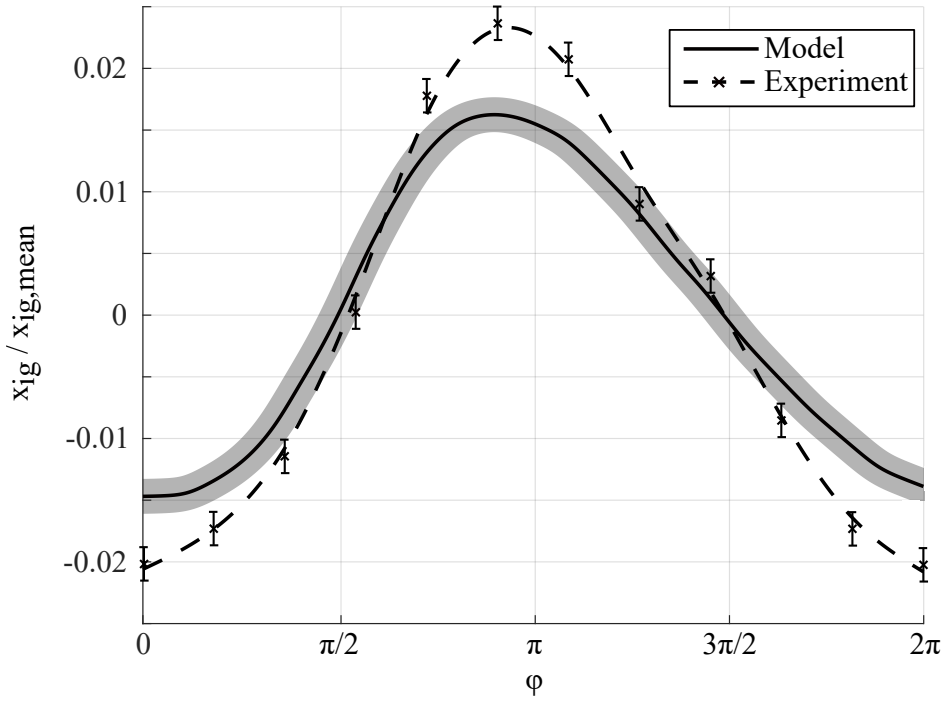

Figure 7.9: Comparison of ignition length variation over a full oscillation cycle between the flame response model and experimental measurements. The dashed line is fitted in a least squares sense to the experimental data points. The experimental error bars show the uncertainty of measuring ignition location due to limited pixel resolution. The shaded region around the model results shows the difference in ignition length variation calculated from the upper and lower bounds of experimental input uncertainties.

of this control uncertainty. This is represented in Fig. 7.9 by the shaded region surrounding the model results.

The experimental results correspond to those of the high-reactivity test case described in Chapter 5. For both cases, the ignition length is defined as the distance from fuel injection in the mixing section to the ignition location. The mean ignition length, $x_{ig,mean}$, is calculated as the average ignition position over the oscillation cycle.

Comparison of the results from the reduced order model and experiments reveals that both cases exhibit a sinusoidal behaviour. The difference between the amplitude of the ignition delay variation from experiments and the flame response model is approximately 30%, indicating that modulation of the autoignition delay time by transverse acoustic oscillations does indeed contribute significantly to the experimentally-observed flame shape modulation. The model and experimental uncertainties illustrated in Fig. 7.9 are not enough to account for this difference in results, however; this is an expected outcome. As described in Section 7.1, the experimentally observed flame motion is not solely a result of autoignition delay modulation but is also due to flame displacement and deformation by the acoustic velocity field. The $\sim 30\%$ difference between the experimental and model results can therefore be assumed to mostly be due to the contribution by flame displacement and deformation. It should also be noted that the modelled ignition delay response shown in Fig. 7.9 is that of the mixture plug closest to the wall of the modelled domain (see Fig. 7.7). As stated previously, this position was chosen as it corresponds to the location of the maximum flame motion observed in the experiments. Due to the sinusoidal mode shape of the transverse mode, the magnitude of the ignition length variation will decrease towards zero at the pressure node along the centreline, after which the magnitude will increase again but with inverted sign. The mixture plug at the opposite wall from that shown in Fig. 7.9 will therefore exhibit the same behaviour but with a phase shift of π radians.

It can also be observed from Fig. 7.9 that the ignition length moves further downstream relative to its mean position than it does upstream. This is due to reducing pressure and temperature sensitivity of the autoignition delay time with increasing pressure and temperature. This effect is illustrated in Fig. 7.10 where the pressure and temperature sensitivity of the ignition delay time are illustrated by the solid and dashed curves, respectively. The ignition delay time decreases monotonically in both cases, with a reduction in the steepness of the gradient as the pressure and temperature increase. The ignition position therefore moves further downstream during phases with negative acoustic pressure am-

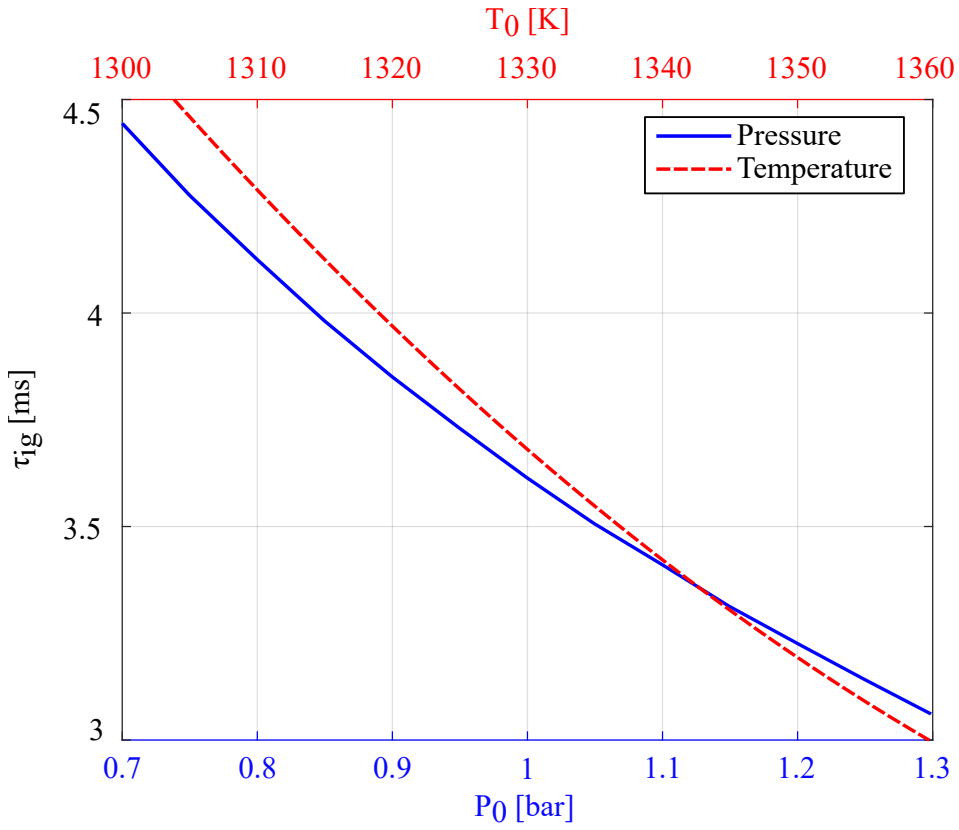

Figure 7.10: Pressure and temperature sensitivity of the autoignition delay time calculated by the flame response model with no acoustic perturbations.

plitude than it moves upstream during positive acoustic pressure phases. This monotonic decrease of autoignition delay time with both pressure and temperature means that both oscillations constructively superpose and increase the magnitude of the ignition delay modulation.

Figure 7.9 indicates an in-phase movement of the ignition location with the pressure oscillations, i.e. there is an upstream flame movement when pressure is high ($\phi = 0, 2\pi$) and a downstream movement when pressure is low ($\phi = \pi$). This instantaneous flame response to transverse acoustic oscillations was predicted previously by Zellhuber et al [111]. However, the reaction kinetics are not only modulated by the instantaneous conditions, but by the history of pressure and temperature conditions along

the fluid particle path [125]. Therefore, the net pressure and temperature modulation experienced by a fluid particle between injection and ignition is also of interest. Figure 7.11 shows the relationship between the ignition length variation and the fluid particle net pressure oscillation for an oscillation cycle. The net acoustic oscillation was calculated simply as a cumulative sum of p' up to the ignition location. This shows an in-phase relationship between ignition length variation and the net acoustic pressure (note that the curves are mirrored due to the sign convention). As the effects of pressure and temperature on ignition delay constructively superpose, the net temperature oscillation follows the same trend as the pressure in Fig. 7.11. The net influence of the pressure and temperature history is particularly important for high-frequency transverse instabilities where fluid particles can experience multiple oscillation cy-

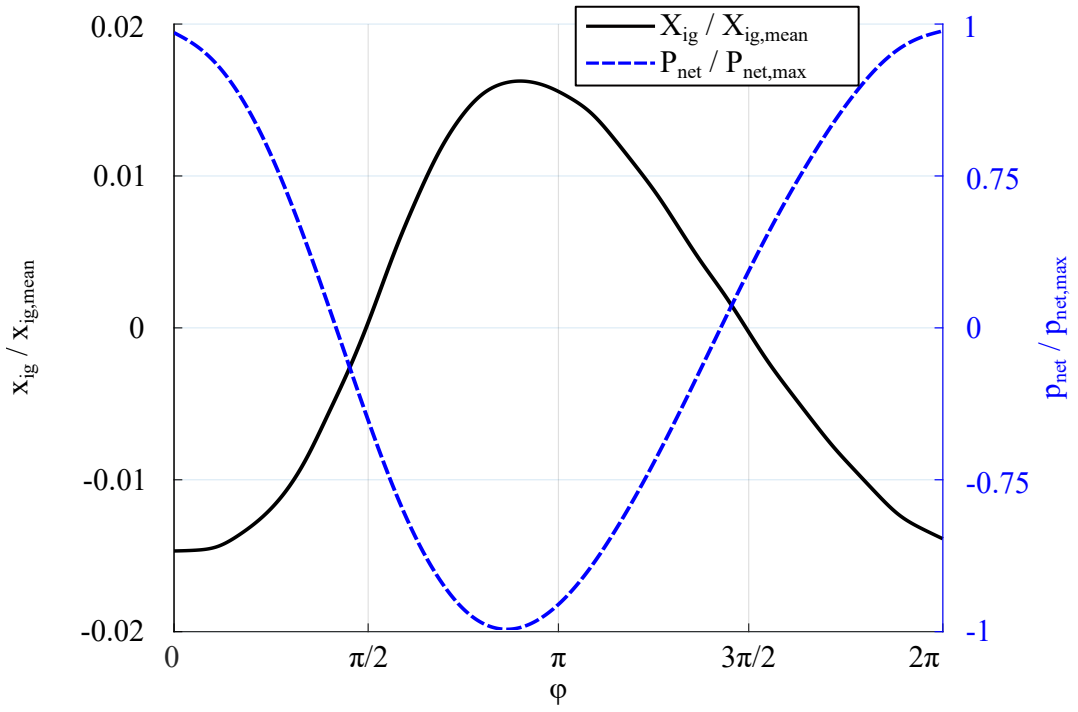

Figure 7.11: Comparison of the ignition length variation and the net pressure oscillation experienced by a fluid particle over an oscillation cycle.

cles between injection and ignition (see Fig. 7.8), the number of which depends on the position of the flame relative to the area jump and the oscillation frequency. As the flame motion represents a fluctuation of heat release about its mean value, understanding the phase relationship between the ignition delay variation and the acoustic condition is essential for determining whether this phenomenon contributes to thermoacoustic driving. During the upstream motion, the heat release rate increases due to the increased relative velocity between the flame front and the mean flow, while the opposite is true during the downstream motion. As shown in Fig. 7.11, the upstream motion (and therefore increased heat release) coincide with the high pressure conditions while the downstream motion coincides with low pressure conditions. This in-phase relationship between pressure and heat release oscillations satisfies the Rayleigh criterion [95] and supports the hypothesis that autoignition delay modulation by high-frequency acoustic pulsations contributes significantly to driving of thermoacoustic instabilities in reheat flames.

7.3 Summary

In this chapter, thermoacoustic driving associated with modulation of the autoignition delay time by acoustic pulsations is investigated. First, the flame response at the T1z mode frequency due to the overlap of the autoignition-stabilised flame zone and regions exhibiting high-amplitude acoustic pressure pulsations is considered. Examination of the dynamic flame response at the T1z mode frequency via phase-locked CL imaging reveals the following:

- A coherent modulation of the flame shape is observed at the T1z mode frequency. This manifests as an alternating axial motion of the flame near the acoustic pressure antinode at the combustion chamber walls. The flame moves upstream when when acoustic pressure is positive and downstream when acoustic pressure is negative.

- This axial flame motion is also associated with a significant heat release oscillation in these regions with high pressure oscillation amplitudes. This in-phase nature of the pressure and heat release oscillations indicates that this is the source of driving for the limit-cycle oscillations experienced by the T1z mode.

- No behaviour associated with acoustically induced vortex shedding is observed for this mode. This is due to the small area expansion in the direction of the T1z mode oscillations. The small area jump does not allow strong recirculation regions to form and the proximity of the area jump edges to the velocity nodes at the walls precludes the formation of strong acoustically-induced vortices.

- A small transverse displacement of the flame can be observed from the phase-locked CL images, indicating that flame displacement (and therefore deformation) contribute to driving of this mode. However, due to the small magnitude of the displacement it is unlikely that the strong driving which produces the limit-cycle oscillations is solely due to these mechanisms. The strong sensitivity of the instability to fuel reactivity indicates that there is a significant driving component associated with modulation of the autoignition-stabilised portion of the flame.

- The observed flame shape and heat release oscillation is therefore expected to be mainly due to the acoustic pressure pulsations modulating the autoignition delay time, which is the reason for the axial flame motion induced by the transversally oscillating acoustic field.

To further investigate this modulation of the autoignition delay time by the acoustic pressure pulsations, a reduced order model coupled with chemical kinetics calculations is developed. This allows calculation of the variation of the autoignition delay time in response to a defined acoustic oscillation, in this case at the amplitude and frequency of the experimentally observed T1z mode. The proposed coupling mechanism between the autoignition flame and the acoustic field is distinct from

those typically relevant in the low frequency regime which are generally due to fluctuations of the upstream flow properties. In this case, the dominant coupling mechanism is a direct modulation of the local reaction kinetics by the acoustic oscillations. The results of the model compared with the experiments reveals the following:

- The majority of the flame motion observed in the experiments can be attributed to the autoignition delay modulation by the acoustic pressure pulsations. This indicates that the autoignition delay modulation mechanism dominates the driving of the high-amplitude limit cycle oscillations while the displacement and deformation mechanisms only make relatively small contributions.
- While there is an instantaneous response of the flame position to acoustic oscillations, the ignition delay also responds in an in-phase manner to the history of acoustic fluctuations experienced by the fluid as it travels through the domain. This net influence is particularly important to consider for high-frequency instabilities as a fluid particle can experience multiple oscillation cycles between injection and ignition.

8 Summary and Conclusions

This thesis investigated the underlying flame-acoustic interactions which drive high-frequency thermoacoustic oscillations in sequentially-staged gas turbine combustion systems, specifically in the reheat stage. Reheat flames feature both propagation- and autoignition stabilisation and this allows the potential for different flame-acoustic coupling mechanisms to arise compared with more conventional combustor types.

In the first part of this work, an experimental study was conducted to investigate the flame response to acoustic oscillations. Two distinct thermoacoustic modes were identified from the pressure spectra under unforced conditions. The first of these was determined to be the first transverse mode in the vertical direction of the rectangular cross-section combustion chamber. This mode occurs at 1600 Hz and was found to be intermittently unstable regardless of operating conditions. The second is also a first transverse mode but oriented horizontally in the combustion chamber, orthogonally to the first. The frequency of this mode is 3000 Hz and it exhibits high-amplitude limit-cycle behaviour but only when the reheat stage is operated at high power settings with a more reactive fuel blend. Both of these modes have been determined to be localised within the reheat combustion chamber and do not extend significantly upstream into the mixing section. As a result, upstream flow conditions are not modulated by the transverse acoustic modes and thus the driving must be a result of local interactions between the flame and acoustics within the combustion chamber.

Investigation of the dynamic flame response revealed that each of the two modes is associated with different coherent flame behaviours. For the 1600 Hz mode, alternating hot/cold patches were observed to be convectively transported through the propagation-stabilised shear layer

regions, modulating the local heat release rate in these areas. This phenomenon was found to be due to acoustically-induced vortex shedding from the edges of the area jump at the frequency of the thermoacoustic instability. In this case there were no coherent fluctuations present in the autoignition stabilised core region of the flame. The pattern of hot/cold patches were not observed for the the 3000 Hz mode, which instead exhibited a periodic axial motion of the flame close to the walls. The reason for the difference in flame response between these two first transverse modes was determined to be due to their orthogonal orientations in the chamber and how the resulting mode shapes allow different interactions between the propagation- and autoignition-stabilised flame regions and the acoustic pressure (and velocity) nodes/antinodes. The vertical orientation of the 1600 Hz mode results in high acoustic velocities at the edges of the area jump. This produces the strong vortices which are convected through the shear layers and cause the pattern of alternating hot/cold patches. For this mode there is also a pressure node at the combustor centreline in the vicinity of the autoignition-stabilised part of the flame, limiting the potential for any significant interactions between this flame regime and the acoustics.

The horizontal orientation of the 3000 Hz mode instead limits the possibility for strong vortex shedding to occur due to the negligible extent of the area expansion in this direction. However, the distribution of pressure nodes and antinodes does result in an overlap between the autoignition flame and high amplitude acoustic oscillations. Due to the pressure sensitivity of autoignition flames, it is proposed that the autoignition delay time is modulated by the acoustic oscillations and that this is the cause of the periodic axial motion observed in the flame response. This hypothesis is supported by the dependence of the limit-cycle oscillations on the fuel reactivity, as this directly impacts the strength of the autoignition portion of the flame. Therefore, two distinct thermoacoustic driving mechanisms are present, each of which varies in importance depending on the mode shape.

- The 1600 Hz mode is primarily driven by modulation of the reac-

tive shear layer regions resulting from acoustically-induced vortex shedding.

- The 3000 Hz mode is primarily driven by local modulation of the autoignition delay time by acoustic pressure oscillations.

These mechanisms are also expected to be superposed with flame displacement and deformation due to the transverse acoustic velocity field, however the effects of these mechanisms were not unambiguously observable from the experimental results.

The objective of the rest of the thesis is therefore to estimate the significance of these flame-acoustic coupling mechanisms for the overall thermoacoustic driving and to determine which are most likely to be important for industrially-relevant combustion systems.

The first step in investigating the mechanism associated with modulation of the reactive shear layers by acoustically-induced vortex shedding was to determine the reason why this mode is only intermittently unstable regardless of operating conditions. The intermittently periodic pressure oscillations were discretised into four conditions: stochastic fluctuations, growth of pressure amplitudes, periodic oscillations and decay of pressure amplitudes. Investigation of the condition dependent flame dynamics revealed that a shift in heat release distribution between the propagation-stabilised shear layers and the autoignition-stabilised core region is the reason for the intermittency. This redistribution of heat release is likely due to the stochastic nature of autoignition kernel formation. Thermoacoustic oscillations arise due to increased heat release away from the pressure node at the combustor centreline and towards the antinodes at the walls, resulting in stronger flame-acoustic feedback and greater driving potential.

Next the phenomenon of acoustically-induced vortex shedding as a thermoacoustic driving mechanism is investigated. This has been observed in previous studies of swirl flames; however, it did not result in thermoacoustic driving in that case due to strong flame quenching in the

shear layers. It is also the subject of ongoing investigation for jet flames. By calculating the net heat release oscillation in each modulated shear layer and comparing this with the phase of the pressure oscillations, an in-phase interaction of the flame and the acoustic field is observed. Furthermore, almost the entire heat release oscillation originates from the shear layer regions, with a negligible amount contributed from the rest of the flame. This mechanism is therefore a very significant driver of the 1600 Hz mode. However, it is clear from the 3000 Hz flame dynamics that this phenomenon is not present, mainly due to the combustor geometry. Furthermore, vortex shedding is also a source of acoustic dissipation, suggesting that as pressure oscillations (and therefore vortex shedding) increase in strength, the associated dissipation will also increase, fundamentally limiting the driving potential of this mode by balancing it with damping. This may also be a factor in the intermittent nature of the 1600 Hz observed in the experiments. The industrial significance of this driving mechanism is also limited by the pressure conditions in real engines. At the elevated pressures present in industrial gas turbine combustors, the autoignition portion of the reheat flame would be proportionately stronger compared with the propagation part due to the high pressure sensitivity of the autoignition delay time. It is therefore suggested that although this mechanism should not be neglected, it is not the key driver of high-frequency thermoacoustic instabilities in reheat flames.

From here, the focus shifts to the mechanism associated with modulation of the autoignition delay time by acoustic pressure perturbations. The flame dynamics of the 3000 Hz mode revealed an axial motion of the autoignition portion of the flame in the regions where the acoustic oscillations are greatest. This flame motion results in a significant fluctuation of the heat release rate which occurs in-phase with the acoustic oscillations. Due to the in-phase nature of the oscillations, and the fact that the heat release fluctuations are a considerable portion of the overall heat release, this behaviour represents an important source of driving potential.

It was observed that there is an upstream motion of the flame when acoustic pressure oscillations are positive and a downstream motion when acoustic pressure is negative. This instantaneous response is expected due to the pressure sensitivity of the autoignition delay time. The local reaction kinetics of he autoignition portion of the flame are therefore being directly modulated by the acoustic oscillations. This mechanism is distinct from the autoignition flame-acoustic coupling mechanisms which have been observed in the low-frequency regime, which are generally a result of coherent fluctuations of the upstream flow properties. This importance of this mechanism for the overall thermoacoustic driving is made clearer by the lack of significant flame displacement/deformation effects observable in the flame dynamics. This suggests that the limit-cycle oscillations are driven primarily by the autoignition delay modulation mechanism, particularly since the 3000 Hz mode only becomes unstable under conditions which favour a stronger autoignition region.

To further investigate the significance of the autoignition delay modulation mechanism, a reduced order model for the response of purely autoignition-stabilised flames to acoustic disturbances was developed and the results are compared with the experimental observations. The model revealed that the majority of the experimentally observed flame motion can be attributed to modulation of the autoignition delay time, while the remaining portion of the motion is assumed to be due to flame displacement/deformation. This explains why the latter mechanisms were not clearly visible in the experimental results, as the response was dominated by the first mechanism. The model also revealed that a significant portion of the autoignition delay modulation is due to the isentropic temperature fluctuations induced by the acoustic pressure pulsations, which is to be expected due to the higher temperature sensitivity of the delay time compared with the pressure sensitivity. In addition to the instantaneous response, the model also indicated that the flame responds in an in-phase manner to the history of acoustic fluctuations experienced by the fluid between fuel injection and ignition. This is particularly interesting for high-frequency modes as a parcel of the

fluid experiences several oscillation cycles before igniting.

Overall the results of the investigation suggests that the autoignition delay modulation mechanism is the key driving mechanism of high-frequency thermoacoustic instabilities in reheat flames. The occurrence of high-amplitude limit-cycle oscillations is dependent on the mode shape, as a strong overlap between the autoignition flame and acoustic pressure antinodes is required, and operating conditions, due to the requirement of a strong autoignition zone. It is therefore essential to predict situations where this driving mechanism could become an issue to avoid thermoacoustic stability issues.

9 Previous Publications

Parts of this Ph.D. thesis have been published by the author in conference proceedings and journal papers. All of these publications are registered according to the valid doctoral regulations. Therefore, they are not necessarily quoted explicitly in the text. Whether they were referenced, depended on maintaining comprehensibility and providing all necessary context. A list of these publications is listed below:

- McClure, J., Bothien, M., Sattelmayer, T., 2023. "Autoignition Delay Modulation by High-Frequency Thermoacoustic Oscillations in Reheat Flames". *Proceedings of the Combustion Institute* **39**(4), pp. 4691-4700
- McClure, J., Bothien, M., Sattelmayer, T., 2023. "High-Frequency Mode Shape Dependent Flame-Acoustic Interactions in Reheat Flames". *Journal of Engineering for Gas Turbines and Power,* **145**(1), p. 011014
- McClure, J., Berger, F., Bertsch, M., Schuermans, B., Sattelmayer, T., 2022. "Observation of Reactive Shear Layer Modulation Associated with High-Frequency Transverse Thermoacoustic Oscillations in a Gas Turbine Reheat Combustor Experiment". *International Journal of Spray and Combustion Dynamics,* **14**(1-2), pp. 131-142
- McClure, J., Berger, F., Bertsch, M., Schuermans, B., Sattelmayer, T., 2021. "Self Excited High-Frequency Transverse Limit-Cycle Oscillations and Associated Flame Dynamics in a Gas Turbine Reheat Combustor Experiment". Proceedings of the ASME Turbo Expo, no. GT2021-59540

Bibliography

[1] International Energy Agency IEA, 2022. World Energy Outlook 2022. Tech. rep., Paris, France.

[2] Rabl, A., and Spadaro, J. V., 2000. "Public Health Impact of Air Pollution and Implications for the Energy System". *Annual Review of Energy and the Environment,* **25**(1), pp. 601–627.

[3] Intergovernmental Panel on Climate Change IPCC, 2022. "Impacts of 1.5 C Global Warming on Natural and Human Systems". In *Global Warming of 1.5 C*. pp. 175–312.

[4] International Emissions Trading Association IETA, 2021. COP26 Summary Report. Tech. rep., Glasgow, UK.

[5] Abanades, A., 2018. "Natural Gas Decarbonization as a Tool for Greenhouse Gases Emission Control". *Frontiers in Energy Research,* ***6***, pp. 1–7.

[6] Gülen, S. C., and Curtis, M., 2022. "Gas Turbine's Role in Energy Transition". In Proceedings of the ASME Turbo Expo, no. GT2022-81802.

[7] International Renewable Energy Agency IRENA, 2018. Power System Flexibility for the Energy Transition. Tech. rep., Abu Dhabi, UAE.

[8] Wang, P., Gao, Z., and Bertling, L., 2012. "Operational Adequacy Studies of Power Systems with Wind Farms and Energy Storages". *IEEE Transactions on Power Systems,* **27**(4), pp. 2377–2384.

[9] Goldthau, A., 2014. "Rethinking the Governance of Energy Infrastructure: Scale, Decentralization and Polycentrism". *Energy Research & Social Science,* ***1***, pp. 134–140.

[10] Lieuwen, T., Chang, M., and Amato, A., 2013. "Stationary Gas Turbine Combustion: Technology Needs and Policy Considerations". *Combustion and Flame,* ***160***(8), pp. 1311–1314.

[11] Gonzalez-Salazar, M. A., Kirsten, T., and Prchlik, L., 2018. "Review of the Operational Flexibility and Emissions of Gas- and Coal-Fired Power Plants in a Future with Growing Renewables". *Renewable and Sustainable Energy Reviews,* ***82***, pp. 1497–1513.

[12] de Groot, M., Crijns-Graus, W., and Harmsen, R., 2017. "The Effects of Variable Renewable Electricity on Energy Efficiency and Full Load Hours of Fossil-Fired Power Plants in the European Union". *Energy,* ***138***, pp. 575–589.

[13] Abudu, K., Igie, U., Roumeliotis, I., and Hamilton, R., 2021. "Impact of Gas Turbine Flexibility Improvements on Combined Cycle Gas Turbine Performance". *Applied Thermal Engineering,* ***189***, p. 116703.

[14] Lee, H., Hernandez, S., McDonell, V., Steinthorsson, E., Mansour, A., and Hollon, B., 2009. "Development of Flashback Resistant Low-Emission Micro-Mixing Fuel Injector for 100% Hydrogen and Syngas Fuels". In Proceedings of the ASME Turbo Expo, no. GT2009-59502.

[15] Mathieu, O., Petersen, E. L., Heufer, A., Donohoe, N., Metcalfe, W., Curran, H. J., Güthe, F., and Bourque, G., 2014. "Numerical Study on the Effect of Real Syngas Compositions on Ignition Delay Times and Laminar Flame Speeds at Gas Turbine Conditions". *Journal of Engineering for Gas Turbines and Power,* ***136***(1), p. 011502.

[16] Zheng, L., Cronly, J., Ubogu, E., Ahmed, I., Zhang, Y., and Khandelwal, B., 2019. "Experimental Investigation on Alternative Fuel

Combustion Performance using a Gas Turbine Combustor". *Applied Energy,* ***238***, pp. 1530–1542.

[17] Mu, Y., Li, Z., Luo, K., Fan, J., Xing, J., Zhang, B., and Shi, S., 2022. "Analyzing the Combustion Oscillation of a Gas Turbine for Syngas based on the Characteristic Time-Scale Theory". *Thermal Science and Engineering Progress,* ***30***, p. 101224.

[18] Aguilar, J. G., Æsøy, E., and Dawson, J. R., 2022. "The Influence of Hydrogen on the Stability of a Perfectly Premixed Combustor". *Combustion and Flame,* ***245***, p. 112323.

[19] Skabelund, B. B., Stechel, E. B., and Milcarek, R. J., 2023. "Thermodynamic Analysis of a Gas Turbine Utilizing Ternary CH4/H2/NH3 Fuel Blends". *Energy,* ***282***, p. 128818.

[20] Cai, Z., Huang, M., Wei, G., Liu, Z., Fang, H., Song, Y., Zhang, M., Wang, W., Ming, Z., Wang, J., Chang, W., Fan, X., Hussain, A., and Hao, Q., 2023. "Numerical Study of the Effect of Pressure on the Combustion Characteristics of Ammonia/Coal-Derived Syngas Mixture under Gas Turbine Operating Conditions". *Fuel,* ***347***, pp. 223–233.

[21] Solana-Pérez, R., Miniero, L., Shcherbanev, S., Bothien, M., and Noiray, N., 2020. "Morphology and Dynamics of a Premixed Hydrogen-Methane-Air Jet Flame in Hot Vitiated Turbulent Crossflow". In Proceedings of the ASME Turbo Expo, no. GT2020-16282.

[22] Bothien, M. R., Ciani, A., Wood, J. P., and Fruechtel, G., 2019. "Toward Decarbonized Power Generation With Gas Turbines by Using Sequential Combustion for Burning Hydrogen". *Journal of Engineering for Gas Turbines and Power,* ***141***(12), p. 121013.

[23] Marek, C. J., Smith, T. D., and Kundu, K., 2005. "Low Emission Hydrogen Combustors for Gas Turbines Using Lean Direct Injection". In 41st AIAA/ASME/SAE/ASEE Joint Propulsion Conference & Exhibit, no. AIAA-2005-3776.

[24] Haines, M., Polman, E., and Delaat, J., 2005. "Reduction of CO2 Emissions by Addition of Hydrogen to Natural Gas". *Greenhouse Gas Control Technologies,* ***7***(1), pp. 337–345.

[25] Poyyapakkam, M., Wood, J., Mayers, S., Ciani, A., Güthe, F., and Syed, K., 2012. "Hydrogen Combustion Within a Gas Turbine Reheat Combustor". In Proceedings of the ASME Turbo Expo, no. GT2012-69165.

[26] Welch, M., 2019. "Decarbonizing Power Generation Through the Use of Hydrogen As a Gas Turbine Fuel". In ASME Power Conference, no. POWER2019-1821.

[27] Beita, J., Talibi, M., Sadasivuni, S., and Balachandran, R., 2021. "Thermoacoustic Instability Considerations for High Hydrogen Combustion in Lean Premixed Gas Turbine Combustors: A Review". *Hydrogen,* ***2***(1), pp. 33–57.

[28] Solana-Pérez, R., Shcherbanev, S. A., Dharmaputra, B., Ciani, A., and Noiray, N., 2023. "Combustion Regime Transition of H2 Flames during Steady and Transient Operation of a Sequential Combustor". *Proceedings of the Combustion Institute,* ***39***(4), pp. 4335–4344.

[29] Solana-Pérez, R., Shcherbanev, S. A., Ciani, A., and Noiray, N., 2023. "Effect of Mixing on the Anchoring and Combustion Regimes of Pure Hydrogen Flames in Sequential Combustors". *Journal of Engineering for Gas Turbines and Power,* ***145***(3).

[30] Niaz, S., Manzoor, T., and Pandith, A. H., 2015. "Hydrogen Storage: Materials, Methods and Perspectives". *Renewable and Sustainable Energy Reviews,* ***50***, pp. 457–469.

[31] Bauer, S., Hampel, B., and Sattelmayer, T., 2017. "Operability Limits of Tubular Injectors With Vortex Generators for a Hydrogen-Fueled Recuperated 100 kW Class Gas Turbine". *Journal of Engineering for Gas Turbines and Power,* ***139***(8), p. 082607.

[32] Funke, H. H. W., Keinz, J., Kusterer, K., Haj Ayed, A., Kazari, M., Kitajima, J., Horikawa, A., and Okada, K., 2017. "Experimental and Numerical Study on Optimizing the DLN Micromix Hydrogen Combustion Principle for Industrial Gas Turbine Applications". *Journal of Thermal Science and Engineering Applications,* ***9***, p. 2017.

[33] Miyamoto, K., Inoue, K., Kawakami, T., Nakamura, S., Tanimura, S., and Masada, J., 2018. "Development of Hydrogen and Natural Gas Co-firing Gas Turbine". In The Future of Gas Turbine Technology 9th International Gas Turbine Conference, no. 73-IGTC18.

[34] Fleck, J., Griebel, P., Steinberg, A. M., Stöhr, M., Aigner, M., and Ciani, A., 2012. "Autoignition Limits of Hydrogen at Relevant Reheat Combustor Operating Conditions". *Journal of Engineering for Gas Turbines and Power,* ***134***(4), p. 041502.

[35] Lefebvre, A. H., and Ballal, D. R., 2010. *Gas Turbine Combustion: Alternative Fuels and Emissions*, 3rd ed. CRC Press, Boca Raton, Florida.

[36] Candel, S., Durox, D., Schuller, T., Bourgouin, J.-F., and Moeck, J. P., 2014. "Dynamics of Swirling Flames". *Annual Review of Fluid Mechanics,* ***46***(1), pp. 147–173.

[37] Eroglu, A., Flohr, P., Brunner, P., and Hellat, J., 2009. "Combustor Design for Low Emissions and Long Lifetime Requirements". In Proceedings of the ASME Turbo Expo, no. GT2009-59540.

[38] Joos, F., Brunner, P., Schulte-Werning, B., Syed, K., and Eroglu, A., 1996. "Development of the Sequential Combustion System for the ABB GT24/GT26 Gas Turbine Family". In International Gas Turbine & Aeroengine Congress & Exhibition, no. 96-GT-315.

[39] Lammel, O., Schütz, H., Schmitz, G., Lückerath, R., Stöhr, M., Noll, B., Aigner, M., Hase, M., and Krebs, W., 2010. "FLOX Combustion at High Power Density and High Flame Temperatures". *Journal of Engineering for Gas Turbines and Power,* ***132***(12), p. 121503.

[40] Funke, H. H. W., Dickhoff, J., Keinz, J., Haj Ayed, A., Parente, A., and Hendrick, P., 2014. "Experimental and Numerical Study of the Micromix Combustion Principle Applied for Hydrogen and Hydrogen- Rich Syngas as Fuel with Increased Energy Density for Industrial Gas Turbine Applications". *Energy Procedia,* ***61***, pp. 1736–1739.

[41] Rosenkranz, J. A., and Sattelmayer, T., 2022. "Analytical Modeling of the Injector Response To High Frequency Modes in a Tubular Multi-Jet-Combustor". In Proceedings of the ASME Turbo Expo, no. GT2022-81957.

[42] Uslu, H. H., Vinci, A., Saviozzi, M., Mosaico, G., Assadi, M., Silvestro, F., and Nikpey Somehsaraei, H., 2022. "Techno-Economic Dispatch Analysis of a Case Study Consisting of Micro Gas Turbines Using Real-Time Data". In Proceedings of the ASME Turbo Expo, no. GT2022-83437.

[43] Düsing, K. M., Ciani, A., Benz, U., Eroglu, A., and Knapp, K., 2013. "Development of GT24 and GT26 (Upgrades 2011) Reheat Combustors, Achieving Reduced Emissions and Increased Fuel Flexibility". In Proceedings of the ASME Turbo Expo, no. GT2013-95437.

[44] Guyot, D., Tea, G., and Appel, C., 2016. "Low NOx Lean Premix Reheat Combustion in Alstom GT24 Gas Turbines". *Journal of Engineering for Gas Turbines and Power,* ***138***(5), p. 051503.

[45] Pennell, D. A., Bothien, M. R., Ciani, A., Granet, V., Singla, G., Thorpe, S., Wickstroem, A., Oumejjoud, K., and Yaquinto, M., 2017. "An Introduction to the Ansaldo GT36 Constant Pressure Sequential Combustor". In Proceedings of the ASME Turbo Expo, no. GT2017-64790.

[46] Güthe, F., Hellat, J., and Flohr, P., 2009. "The Reheat Concept: The Proven Pathway to Ultralow Emissions and High Efficiency and Flexibility". *Journal of Engineering for Gas Turbines and Power,* ***131***(2), p. 021503.

[47] Ciani, A., Bothien, M., Bunkute, B., Wood, J., and Früchtel, G., 2019. "Superior Fuel and Operational Flexibility of Sequential Combustion in Ansaldo Energia Gas Turbines". *Journal of the Global Power and Propulsion Society,* ***3***, pp. 630–638.

[48] Lieuwen, T. C., 2012. *Unsteady Combustor Physics*. Cambridge University Press, Cambridge, UK.

[49] Candel, S., 2002. "Combustion Dynamics and Control: Progress and Challenges". *Proceedings of the Combustion Institute,* ***29***(1), pp. 1–28.

[50] Culick, F. E. C., 2006. *Unsteady Motions in Combustion Chambers for Propulsion Systems*. AGARDograph, NATO RTO-AG-AVT-039.

[51] Goy, C. J., James, S. R., and Rea, S., 2005. "Monitoring Combustion Instabilities: E.ON UK's Experience". In *Combustion Instabilities in Gas Turbine Engines - Operational Experience, Fundamental Mechanisms, and Modeling*, T. C. Lieuwen and V. Yang, eds. AIAA, ch. 8, pp. 163–175.

[52] Poinsot, T., 2017. "Prediction and Control of Combustion Instabilities in Real Engines". *Proceedings of the Combustion Institute,* ***36***(1), pp. 1–28.

[53] Lieuwen, T., Torres, H., Johnson, C., and Zinn, B. T., 2001. "A Mechanism of Combustion Instability in Lean Premixed Gas Turbine Combustors". *Journal of Engineering for Gas Turbines and Power,* ***123***(1), pp. 182–189.

[54] Ćosić, B., Moeck, J. P., and Paschereit, C. O., 2014. "Nonlinear Instability Analysis for Partially Premixed Swirl Flames". *Combustion Science and Technology,* ***186***, pp. 713–736.

[55] Noiray, N., 2017. "Linear Growth Rate Estimation From Dynamics and Statistics of Acoustic Signal Envelope in Turbulent Combustors". *Journal of Engineering for Gas Turbines and Power,* ***139***(4), p. 041503.

[56] Han, X., Li, J., and Morgans, A. S., 2015. "Prediction of Combustion Instability Limit Cycle Oscillations by Combining Flame Describing Function Simulations with a Thermoacoustic Network Model". *Combustion and Flame,* ***162***(10), pp. 3632–3647.

[57] Xia, Y., Morgans, A., Jones, W., Rogerson, J., Bulat, G., and Han, X., 2017. "Predicting Thermoacoustic Instability in an Industrial Gas Turbine Combustor: Combining a Low Order Network Model with Flame LES". In Proceedings of the ASME Turbo Expo, no. GT2017-63247.

[58] Schulze, M., Hummel, T., Klarmann, N., Berger, F. M., Schuermans, B., and Sattelmayer, T., 2017. "Linearized Euler Equations for the Prediction of Linear High-Frequency Stability in Gas Turbine Combustors". *Journal of Engineering for Gas Turbines and Power,* ***139***(3), p. 031510.

[59] Hofmeister, T., 2021. "Influence of Acoustically-Induced Vorticity Perturbations on High-Frequency Thermoacoustic Instabilities in Gas Turbine Combustors". PhD thesis, Technical University of Munich, Munich, Germany.

[60] Zellhuber, M. P. G., 2013. "High Frequency Response of Auto-Ignition and Heat Release to Acoustic Perturbations". PhD thesis, Technical University of Munich, Munich, Germany.

[61] Hummel, T., 2018. "Modeling and Analysis of High-Frequency Thermoacoustic Oscillations in Gas Turbine Combustion Chambers". PhD thesis, Technical University of Munich, Munich, Germany.

[62] Schulz, O., and Noiray, N., 2019. "Combustion Regimes in Sequential Combustors: Flame Propagation and Autoignition at Elevated Temperature and Pressure". *Combustion and Flame,* ***205***, pp. 253–268.

[63] Krisman, A., Hawkes, E. R., and Chen, J. H., 2018. "The Structure and Propagation of Laminar Flames under Autoignitive Conditions". *Combustion and Flame,* ***188***, pp. 399–411.

[64] Spadaccini, L., and Colket, M., 1994. "Ignition Delay Characteristics of Methane Fuels". *Progress in Energy and Combustion Science,* ***20***(5), pp. 431–460.

[65] Goy, C. J., Moran, A. J., and Thomas, G. O., 2001. "Autoignition Characteristics of Gaseous Fuels at Representative Gas Turbine Conditions". In Proceedings of the ASME Turbo Expo, no. 2001-GT-0051.

[66] Gant, F., 2021. "Thermoacoustics of Advanced Reheat Combustion Systems". PhD thesis, ETH Zurich, Zurich, Switzerland.

[67] Healy, D., Curran, H., Dooley, S., Simmie, J., Kalitan, D., Petersen, E., and Bourque, G., 2008. "Methane/Propane Mixture Oxidation at High Pressures and at High, Intermediate and Low Temperatures". *Combustion and Flame,* ***155***(3), pp. 451–461.

[68] Pers, H., Aniello, A., Morisseau, F., and Schuller, T., 2023. "Autoignition-Induced Flashback in Hydrogen-Enriched Laminar Premixed Burners". *International Journal of Hydrogen Energy,* ***48***(27), pp. 10235–10249.

[69] Xia, H., Han, W., Wei, X., Zhang, M., Wang, J., Huang, Z., and Hasse, C., 2023. "Numerical Investigation of Boundary Layer Flashback of CH4/H2/Air Swirl Flames under Different Thermal Boundary Conditions in a Bluff-Body Swirl Burner". *Proceedings of the Combustion Institute,* ***39***(4), pp. 4541–4551.

[70] Saravanamuttoo, H. I. H., Rogers, G. F. C., Cohen, H., and Straznicky, P. V., 2009. *Gas Turbine Theory*, 7th ed. Pearson Prentice Hall, Harlow, UK.

[71] Correa, S. M., 1993. "A Review of NOx Formation Under Gas-Turbine Combustion Conditions". *Combustion Science and Technology,* ***87***(1-6), pp. 329–362.

[72] Düsing, K. M., Ciani, A., and Eroglu, A., 2011. "Effect of Mixing Quality on NOx Emissions in Reheat Combustion of GT24 & GT26 Engines". In Proceedings of the ASME Turbo Expo, no. GT2011-45676.

[73] Gysling, D. L., Copeland, G. S., Mccormick, D. C., and Proscia, W. M., 1998. "Combustion System Damping Augmentation with Helmholtz Resonators". In International Gas Turbine & Aeroengine Congress & Exhibition, no. 98-GT-268.

[74] Bellucci, V., Flohr, P., Paschereit, C. O., and Magni, F., 2004. "On the Use of Helmholtz Resonators for Damping Acoustic Pulsations in Industrial Gas Turbines". *Journal of Engineering for Gas Turbines and Power,* ***126***(2), pp. 271–275.

[75] Bellucci, V., Schuermans, B., Nowak, D., Flohr, P., and Paschereit, C. O., 2005. "Thermoacoustic Modeling of a Gas Turbine Combustor Equipped With Acoustic Dampers". *Journal of Turbomachinery,* ***127***(2), pp. 372–379.

[76] Noiray, N., and Schuermans, B., 2012. "Theoretical and Experimental Investigations on Damper Performance for Suppression of Thermoacoustic Oscillations". *Journal of Sound and Vibration,* ***331***(12), pp. 2753–2763.

[77] Bothien, M. R., Noiray, N., and Schuermans, B., 2014. "A Novel Damping Device for Broadband Attenuation of Low-Frequency Combustion Pulsations in Gas Turbines". *Journal of Engineering for Gas Turbines and Power,* ***136***(4), p. 041504.

[78] Schuermans, B., Bothien, M., Maurer, M., and Bunkute, B., 2015. "Combined Acoustic Damping-Cooling System for Operational Flexibility of GT26/GT24 Reheat Combustors". In Proceedings of the ASME Turbo Expo, no. GT2015-42287.

[79] Cai, C., and Mak, C. M., 2018. "Noise Attenuation Capacity of a Helmholtz Resonator". *Advances in Engineering Software,* ***116***, pp. 60–66.

[80] Singla, G., Noiray, N., and Schuermans, B., 2012. "Combustion Dynamics Validation of an Annular Reheat Combustor". In Proceedings of the ASME Turbo Expo, no. GT2012-68684.

[81] Lieuwen, T., and Zinn, B. T., 1998. "The Role of Equivalence Ratio Oscillations in Driving Combustion Instabilities in Low NOx Gas Turbines". *International Symposium on Combustion,* ***27***(2), pp. 1809–1816.

[82] Stöhr, M., Yin, Z., and Meier, W., 2017. "Interaction Between Velocity Fluctuations and Equivalence Ratio Fluctuations During Thermoacoustic Oscillations in a Partially Premixed Swirl Combustor". *Proceedings of the Combustion Institute,* ***36***, pp. 3907–3915.

[83] Vogel, M., Bachfischer, M., Kaufmann, J., and Sattelmayer, T., 2021. "Experimental Investigation of Equivalence Ratio Fluctuations in a Lean Premixed Kerosene Combustor". *Experiments in Fluids,* ***62***(5), p. 93.

[84] Schwing, J., Sattelmayer, T., and Noiray, N., 2011. "Interaction of Vortex Shedding and Transverse High-Frequency Pressure Oscillations in a Tubular Combustion Chamber". In Proceedings of the ASME Turbo Expo, no. GT2011-45246.

[85] Hofmeister, T., Hummel, T., Schuermans, B., and Sattelmayer, T., 2020. "Modeling and Quantification of Acoustic Damping Induced by Vortex Shedding in Noncompact Thermoacoustic Systems". *Journal of Engineering for Gas Turbines and Power,* ***142***(3), p. 031016.

[86] Rosenkranz, J.-A., and Sattelmayer, T., 2023. "Experimental Investigation of High Frequency Flame Response on Injector Coupling in a Perfectly Premixed Multi-Jet Combustor". In Proceedings of the ASME Turbo Expo, no. GT2023-101417.

[87] Palies, P., Durox, D., Schuller, T., and Candel, S., 2010. "The Combined Dynamics of Swirler and Turbulent Premixed Swirling Flames". *Combustion and Flame,* ***157***(9), pp. 1698–1717.

[88] Tay-Wo-Chong, L., Komarek, T., Kaess, R., FoÂ¨ller, S., and Polifke, W., 2010. "Identification of Flame Transfer Functions From LES of a Premixed Swirl Burner". In Proceedings of the ASME Turbo Expo, no. GT2010-22769.

[89] Blumenthal, R. S., Subramanian, P., Sujith, R., and Polifke, W., 2013. "Novel Perspectives on the Dynamics of Premixed Flames". *Combustion and Flame,* ***160***(7), pp. 1215–1224.

[90] Berger, F. M., Hummel, T., Hertweck, M., Kaufmann, J., Schuermans, B., and Sattelmayer, T., 2017. "High-Frequency Thermoacoustic Modulation Mechanisms in Swirl-Stabilized Gas Turbine Combustors - Part I: Experimental Investigation of Local Flame Response". *Journal of Engineering for Gas Turbines and Power,* ***139***(7), p. 071501.

[91] Hummel, T., Berger, F., Hertweck, M., Schuermans, B., and Sattelmayer, T., 2017. "High-Frequency Thermoacoustic Modulation Mechanisms in Swirl-Stabilized Gas Turbine Combustors - Part II: Modeling and Analysis". *Journal of Engineering for Gas Turbines and Power,* ***139***(7), p. 071502.

[92] Mangold, T. O., Orchini, A., Paschereit, C. O., Moeck, J. P., and Bohon, M. D., 2022. "Flame Response of a Lean Premixed Swirl Flame To High Frequency Azimuthal Forcing". In Proceedings of the ASME Turbo Expo, no. GT2022-84211.

[93] Noiray, N., Durox, D., Schuller, T., and Candel, S., 2008. "A Unified Framework for Nonlinear Combustion Instability Analysis based on the Flame Describing Function". *Journal of Fluid Mechanics,* ***615***, pp. 139–167.

[94] Li, J., Xia, Y., Morgans, A. S., and Han, X., 2017. "Numerical Prediction of Combustion Instability Limit Cycle Oscillations for a Combustor with a Long Flame". *Combustion and Flame,* ***185***, pp. 28–43.

[95] Rayleigh, J. W. S., 1878. *The Theory of Sound*, 2nd ed. Macmillan, London, U.K.

[96] Schwing, J., and Sattelmayer, T., 2013. "High-Frequency Instabilities in Cylindrical Flame Tubes: Feedback Mechanism and Damping". In Proceedings of the ASME Turbo Expo, no. GT2013-94064.

[97] Stuttaford, P., Rizkalla, H., Oumejjoud, K., Demougeot, N., Bosnoian, J., Hernandez, F., Yaquinto, M., Mohammed, A. P., Terrell, D., and Weller, R., 2016. "FlameSheet Combustor Engine and Rig Validation for Operational and Fuel Flexibility With Low Emissions". In Proceedings of the ASME Turbo Expo, no. GT2016-56696.

[98] Armitage, C. A., Balachandran, R., Mastorakos, E., and Cant, R. S., 2006. "Investigation of the Nonlinear Response of Turbulent Premixed Flames to Imposed Inlet Velocity Oscillations". *Combustion and Flame,* ***146***(3), pp. 419–436.

[99] Balachandran, R., Dowling, A. P., and Mastorakos, E., 2008. "Non-Linear Response of Turbulent Premixed Flames to Imposed Inlet Velocity Oscillations of Two Frequencies". *Flow, Turbulence and Combustion,* ***80***, pp. 455–487.

[100] Hummel, T., Hammer, K., Romero, P., Schuermans, B., and Sattelmayer, T., 2017. "Low-Order Modeling of Nonlinear High-Frequency Transversal Thermoacoustic Oscillations in Gas Turbine Combustors". *Journal of Engineering for Gas Turbines and Power,* ***139***(7), p. 071503.

[101] Lieuwen, T. C., 2002. "Experimental Investigation of Limit-Cycle Oscillations in an Unstable Gas Turbine Combustor". *Journal of Propulsion and Power,* ***18***(1), pp. 61–67.

[102] Noiray, N., and Schuermans, B., 2013. "Deterministic Quantities Characterizing Noise Driven Hopf Bifurcations in Gas Turbine Combustors". *International Journal of Non-Linear Mechanics,* ***50***, pp. 152–163.

[103] Krebs, W., Krediet, H., Portillo, E., Hermeth, S., Poinsot, T., Schimek, S., and Paschereit, O., 2013. "Comparison of Nonlin-

ear to Linear Thermoacoustic Stability Analysis of a Gas Turbine Combustion System". *Journal of Engineering for Gas Turbines and Power,* ***135***(8), p. 081503.

[104] Krediet, H. J., Beck, C. H., Krebs, W., and Kok, J. B., 2013. "Saturation Mechanism of the Heat Release Response of a Premixed Swirl Flame using LES". *Proceedings of the Combustion Institute,* ***34***(1), pp. 1223–1230.

[105] Berger, F. M., Hummel, T., Schuermans, B., and Sattelmayer, T., 2018. "Pulsation-Amplitude-Dependent Flame Dynamics of High-Frequency Thermoacoustic Oscillations in Lean-Premixed Gas Turbine Combustors". *Journal of Engineering for Gas Turbines and Power,* ***140***(4), p. 041507.

[106] Hofmeister, T., and Sattelmayer, T., 2021. "Amplitude-Dependent Damping and Driving Rates of High-Frequency Thermoacoustic Oscillations in a Lab-Scale Lean-Premixed Gas Turbine Combustor". *Journal of Engineering for Gas Turbines and Power,* ***143***(12), p. 121018.

[107] O'Connor, J., Acharya, V., and Lieuwen, T., 2015. "Transverse Combustion Instabilities: Acoustic, Fluid Mechanic, and Flame Processes". *Progress in Energy and Combustion Science,* ***49***, pp. 1–39.

[108] Shreekrishna, and Lieuwen, T., 2009. "High Frequency Premixed Flame Response to Acoustic Perturbations". In 15th AIAA/CEAS Aeroacoustics Conference (30th AIAA Aeroacoustics Conference), no. AIAA-2009-3261.

[109] Schimek, S., Ćosić, B., Moeck, J. P., Terhaar, S., and Paschereit, C. O., 2015. "Amplitude-Dependent Flow Field and Flame Response to Axial and Tangential Velocity Fluctuations". *Journal of Engineering for Gas Turbines and Power,* ***137***(8), p. 081501.

[110] Berger, F., 2020. "High Frequency Transverse Thermoacoustic Instabilities in Swirl and Reheat Combustors". PhD thesis, Technical University of Munich, Munich, Germany.

[111] Zellhuber, M., Schuermans, B., and Polifke, W., 2014. "Impact of Acoustic Pressure on Autoignition and Heat Release". *Combustion Theory and Modelling,* ***18***(1), pp. 1–31.

[112] Romero, P., 2022. "Numerical Modeling of High-Frequency Transverse Thermoacoustic Instabilities in Reheat Combustors". PhD thesis, Technical University of Munich, Munich, Germany.

[113] Yang, Y., Schulz, O., Noiray, N., Düsing, K. M., Scarpato, A., and Bothien, M., 2015. "Numerical Analysis of the Dynamic Flame Response in Alstom Reheat Combustion Systems". In Proceedings of the ASME Turbo Expo, no. GT2015-42622.

[114] Schulz, O., and Noiray, N., 2018. "Autoignition Flame Dynamics in Sequential Combustors". *Combustion and Flame,* ***192***, pp. 86–100.

[115] Schulz, O., Doll, U., Ebi, D., Droujko, J., Bourquard, C., and Noiray, N., 2019. "Thermoacoustic Instability in a Sequential Combustor: Large Eddy Simulation and Experiments". *Proceedings of the Combustion Institute,* ***37***(4), pp. 5325–5332.

[116] Gant, F., Bunkute, B., and Bothien, M. R., 2021. "Reheat Flames Response to Entropy Waves". *Proceedings of the Combustion Institute,* ***38***(4), pp. 6271–6278.

[117] Gopalakrishnan, H. S., Gruber, A., and Moeck, J., 2021. "Response of Autoignition-Stabilized Flames to One-Dimensional Disturbances: Intrinsic Response". *Journal of Engineering for Gas Turbines and Power,* ***143***(12), aug, p. 121011.

[118] Schwing, J., Grimm, F., and Sattelmayer, T., 2012. "A Model for the Thermo-Acoustic Feedback of Transverse Acoustic Modes and Periodic Oscillations in Flame Position in Cylindrical Flame Tubes". In Proceedings of the ASME Turbo Expo, no. GT2012-68775.

[119] Zellhuber, M., Schwing, J., Schuermans, B., Sattelmayer, T., and Polifke, W., 2014. "Experimental and Numerical Investigation of Thermoacoustic Sources Related to High-Frequency Instabilities".

International Journal of Spray and Combustion Dynamics, ***6***(1), pp. 1–34.

[120] Romero, P., Berger, F. M., Hummel, T., Schuermans, B., and Sattelmayer, T., 2018. "Numerical Design of a Novel Reheat Combustor Experiment for the Analysis of High-Frequency Flame Dynamics". In Proceedings of the ASME Turbo Expo, no. GT2018-77034.

[121] Klarmann, N., Sattelmayer, T., Zoller, B. T., Geng, W., and Magni, F., 2016. "Impact of Flame Stretch and Heat Loss on Heat Release Distributions in Gas Turbine Combustors: Model Comparison and Validation". In Proceedings of the ASME Turbo Expo, no. GT2016-57625.

[122] Buschhagen, T., Gejji, R., Philo, J., Tran, L., Enrique Portillo Bilbao, J., and Slabaugh, C. D., 2018. "Experimental Investigation of Self-Excited Combustion Instabilities in a Lean, Premixed, Gas Turbine Combustor at High Pressure". *Journal of Engineering for Gas Turbines and Power,* ***140***(11), p. 111503.

[123] Buschhagen, T., Gejji, R., Philo, J., Tran, L., Bilbao, J. E. P., and Slabaugh, C. D., 2019. "Self-Excited Transverse Combustion Instabilities in a High Pressure Lean Premixed Jet Flame". *Proceedings of the Combustion Institute,* ***37***(4), pp. 5181–5188.

[124] Philo, J. J., Gejji, R. M., and Slabaugh, C. D., 2020. "Injector-Coupled Transverse Instabilities in a Multi-Element Premixed Combustor". *International Journal of Spray and Combustion Dynamics,* ***12***, pp. 1–17.

[125] Ni, A., Joos, F., and Polifke, W., 2000. "Ignition Delay Time Modulation as a Contribution to Thermo-Acoustic Instability in Sequential Combustion". In Proceedings of the ASME Turbo Expo, no. 2000-GT-0103.

[126] Zellhuber, M. P. G., Bellucci, V., Schuermans, B., and Polifke, W., 2011. "Modelling the Impact of Acoustic Pressure Waves on Auto-

Ignition Flame Dynamics". In Proceedings of the 5th European Combustion Meeting.

[127] Zellhuber, M., Tay-Wo-Chong, L., and Polifke, W., 2011. "Non-Linear Flame Response at Small Perturbation Amplitudes – Consequences for Analysis of Thermoacoustic Instabilities". In Proceedings of the 5th European Combustion Meeting.

[128] Zellhuber, M., Meraner, C., Kulkarni, R., Polifke, W., and Schuermans, B., 2013. "Large Eddy Simulation of Flame Response to Transverse Acoustic Excitation in a Model Reheat Combustor". *Journal of Engineering for Gas Turbines and Power,* ***135***(9), p. 091508.

[129] Scarpato, A., Zander, L., Kulkarni, R., and Schuermans, B., 2016. "Identification of Multi-Parameter Flame Transfer Function for a Reheat Combustor". In Proceedings of the ASME Turbo Expo, no. GT2016-57699.

[130] Bothien, M., Lauper, D., Yang, Y., and Scarpato, A., 2019. "Reconstruction and Analysis of the Acoustic Transfer Matrix of a Reheat Flame From Large-Eddy Simulations". *Journal of Engineering for Gas Turbines and Power,* ***141***(2), p. 021018.

[131] Fleck, J. M., Griebel, P., Steinberg, A. M., Stöhr, M., Aigner, M., and Ciani, A., 2010. "Experimental Investigation of a Generic, Fuel Flexible Reheat Combustor at Gas Turbine Relevant Operating Conditions". In Proceedings of the ASME Turbo Expo, no. GT2010-22722.

[132] Fleck, J. M., Griebel, P., Steinberg, A. M., Arndt, C. M., Naumann, C., and Aigner, M., 2013. "Autoignition of Hydrogen/Nitrogen Jets in Vitiated Air Crossflows at Different Pressures". *Proceedings of the Combustion Institute,* ***34***(2), pp. 3185–3192.

[133] Gopalakrishnan, H. S., 2022. "Dynamics and Stability of Autoignition Fronts in Elementary Reheat Combustor Configurations". PhD thesis, NTNU, Trondheim, Norway.

[134] Gant, F., Scarpato, A., and Bothien, M. R., 2019. "Occurrence of Multiple Flame Fronts in Reheat Combustors". *Combustion and Flame,* ***205***, pp. 220–230.

[135] Morgans, A. S., and Duran, I., 2016. "Entropy Noise: A Review of Theory, Progress and Challenges". *International Journal of Spray and Combustion Dynamics,* ***8***(4), pp. 285–298.

[136] Hosseinalipour, S., Fattahi, A., Khalili, H., Tootoonchian, F., and Karimi, N., 2020. "Experimental Investigation of Entropy Waves Evolution for Understanding of Indirect Combustion Noise in Gas Turbine Combustors". *Energy,* ***195***, p. 116978.

[137] Bonciolini, G., and Noiray, N., 2019. "Synchronization of Thermoacoustic Modes in Sequential Combustors". *Journal of Engineering for Gas Turbines and Power,* ***141***(3), p. 031010.

[138] Weilenmann, M., Xiong, Y., Bothien, M., and Noiray, N., 2019. "Background-Oriented Schlieren of Fuel Jet Flapping under Thermoacoustic Oscillations in a Sequential Combustor". *Journal of Engineering for Gas Turbines and Power,* ***141***(1), p. 011030.

[139] Berger, F. M., Hummel, T., Romero, P., Schuermans, B., and Sattelmayer, T., 2018. "A Novel Reheat Combustor Experiment for the Analysis of High-Frequency Flame Dynamics - Concept and Experimental Validation". In Proceedings of the ASME Turbo Expo, GT2018-77101.

[140] Güthe, F., Guyot, D., Singla, G., Noiray, N., and Schuermans, B., 2012. "Chemiluminescence as Diagnostic Tool in the Development of Gas Turbines". *Applied Physics B: Lasers and Optics,* ***107***(3), pp. 619–636.

[141] Lauer, M., and Sattelmayer, T., 2010. "On the Adequacy of Chemiluminescence as a Measure for Heat Release in Turbulent Flames With Mixture Gradients". *Journal of Engineering for Gas Turbines and Power,* ***132***(6), p. 061502.

[142] Aditya, K., Gruber, A., Xu, C., Lu, T., Krisman, A., Bothien, M. R., and Chen, J. H., 2019. "Direct Numerical Simulation of Flame Stabilization Assisted by Autoignition in a Reheat Gas Turbine Combustor". *Proceedings of the Combustion Institute,* ***37***(2), pp. 2635–2642.

[143] Feldman, M., 2011. "Hilbert Transform in Vibration Analysis". *Mechanical Systems and Signal Processing,* ***25***(3), pp. 735–802.

[144] Güthe, F., and Schuermans, B., 2007. "Phase-Locking in Post-Processing for Pulsating Flames". *Measurement Science and Technology,* ***18***(9), pp. 3036–3042.

[145] Hertweck, M., Berger, F. M., Hummel, T., and Sattelmayer, T., 2016. "Impact of the Heat Release Distribution on High-Frequency Transverse Thermoacoustic Driving in Premixed Swirl Flames". *International Journal of Spray and Combustion Dynamics,* ***9***(3), pp. 143–154.

[146] Ciani, A., Eroglu, A., Güthe, F., and Paikert, B., 2010. "Full-Scale Atmospheric Tests of Sequential Combustion". In Proceedings of the ASME Turbo Expo, no. GT2010-22891.

[147] Nair, V., Thampi, G., and Sujith, R. I., 2014. "Intermittency Route to Thermoacoustic Instability in Turbulent Combustors". *Journal of Fluid Mechanics,* ***756***, pp. 470–487.

[148] Unni, V. R., and Sujith, R. I., 2017. "Flame Dynamics During Intermittency in a Turbulent Combustor". *Proceedings of the Combustion Institute,* ***36***(3), pp. 3791–3798.

[149] Kheirkhah, S., Cirtwill, J. D., Saini, P., Venkatesan, K., and Steinberg, A. M., 2017. "Dynamics and Mechanisms of Pressure, Heat Release Rate, and Fuel Spray Coupling During Intermittent Thermoacoustic Oscillations in a Model Aeronautical Combustor at Elevated Pressure". *Combustion and Flame,* ***185***, pp. 319–334.

[150] George, N. B., Unni, V. R., Raghunathan, M., and Sujith, R. I., 2018. "Pattern Formation During Transition from Combustion Noise to

Thermoacoustic Instability via Intermittency". *Journal of Fluid Mechanics,* ***849***, pp. 615–644.

[151] Ebi, D., Denisov, A., Bonciolini, G., Boujo, E., and Noiray, N., 2018. "Flame Dynamics Intermittency in the Bistable Region Near a Subcritical Hopf Bifurcation". *Journal of Engineering for Gas Turbines and Power,* ***140***(6), p. 061504.

[152] Kabiraj, L., and Sujith, R. I., 2012. "Nonlinear Self-Excited Thermoacoustic Oscillations: Intermittency and Flame Blowout". *Journal of Fluid Mechanics,* ***713***, pp. 376–397.

[153] Gant, F., Gruber, A., and Bothien, M. R., 2020. "Development and Validation Study of a 1D Analytical Model for the Response of Reheat Flames to Entropy Waves". *Combustion and Flame,* **222**, pp. 305–316.

[154] Goodwin, D. G., Speth, R. L., Moffat, H. K., and Weber, B. W., 2021. Cantera: An Object-Oriented Software Toolkit for Chemical Kinetics, Thermodynamics, and Transport Processes.

[155] Smith, G. P., Golden, D. M., Frenklach, M., Moriarty, N. W., Eiteneer, B., Goldenberg, M., Bowman, C. T., Hanson, R. K., Song, S., Gardiner, W. C., Lissianski, V. V., and Qin, Z., 2022. GRI-Mech 3.0.

[156] Sattelmayer, T., 2003. "Influence of the Combustor Aerodynamics on Combustion Instabilities From Equivalence Ratio Fluctuations". *Journal of Engineering for Gas Turbines and Power,* ***125***(1), pp. 11–19.